Analysis of elastoplastic response of maritime structures in breaking waves using a double pendulum with a friction hinge

R.R. van Zanten

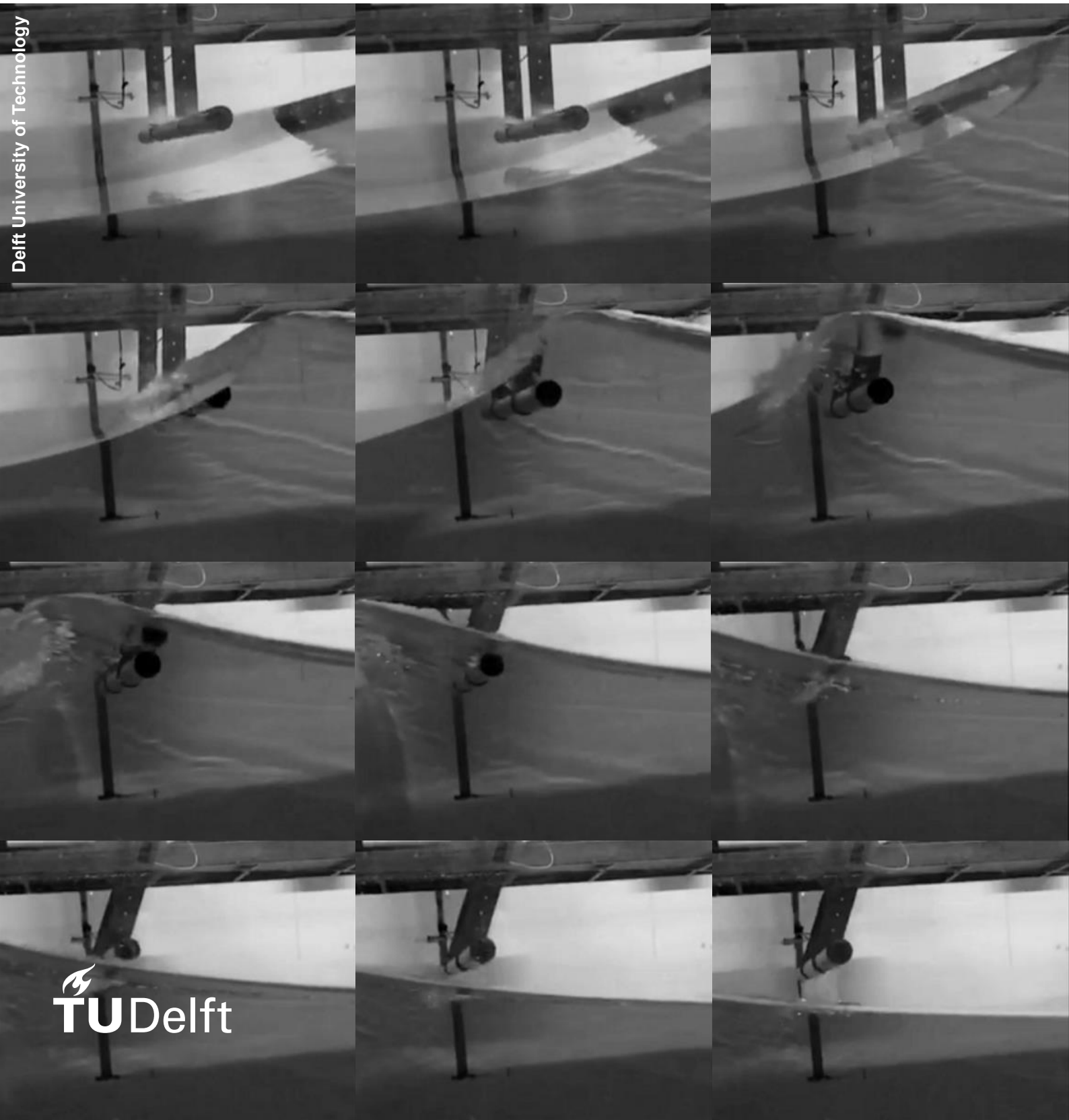

Delft University of Technology

TU Delft

Analysis of elastoplastic response of maritime structures in breaking waves using a double pendulum with a friction hinge

by

R.R. van Zanten

to obtain the degree of
Master of Science in Marine Technology
at the Delft University of Technology,
to be defended publicly on Friday December 18, 2020, at 11:00.

Student number:	4361067	
Project duration:	March 2, 2020 – December 18, 2020	
Assessment Committee:	Dr.ir. P.R. Wellens	Delft University of Technology, Chair
	Ir. R.W. Bos	Delft University of Technology, Supervisor
	Dr.ir. J.H. den Besten	Delft University of Technology
	Dr. F. Alijani	Delft University of Technology

An electronic version of this literature study is available at https://repository.tudelft.nl/.

TU Delft

Summary

Waves impacting on maritime structures can cause damage which endangers the environment around these structures. In 2005, hurricanes Katrina and Rita raged over the Gulf of Mexico, causing structural damage to over 100 drilling platforms with their extreme wave and weather conditions, resulting in 30.2 million litres of oil spillage. Fluid-structure interaction (FSI) plays an important role in this harmful event based on structural failure.

In existing research, extensive analysis of hydro-elastic interaction between regular or breaking waves and walls or cylinders is carried out. When the wave loads become too high and hydro-plasticity occurs, the plastic response is strongly coupled with the hydrodynamic pressure. This phenomenon could leave the structure with little residual strength, resulting in structural failure. No research has been found on a simple understanding of the influence of plasticity on FSI in waves. Research in this area has to be conducted to create a safer working environment, to reduce overconsumption of sources and to lead to fewer environmental accidents. To investigate the influence of plasticity on FSI, the use of a double pendulum with few degrees of freedom and known properties is proposed, so that the emphasis of the research can be on FSI. The following question is answered with an experiment and reduced-order model: *What is the influence of plasticity on the behaviour of a pendulum in breaking waves?*

This question is answered by investigating a double pendulum that is exposed to impact loads in the form of breaking waves. The top hinge of the pendulum is a regular hinge, while the second hinge, added on a lower point on the pendulum, is fixated with a frictional torque. A frictional torque (0 - 11 Nm) is used as a mechanical representation of the *Yield Point Theory*, which is a plasticity theory that assumes a certain stress needs to be overcome to initiate the motion of material dislocations. After that point, a lower stress is required for dislocation movement. Three different pendulums are subjected to three focused waves with different focus locations in front of the pendulum.

The first aspect of the behaviour that is analysed is the motion of the pendulum, which, in our approach, models the deformation of a structure. Compared to the situation in which sufficient friction is applied to create a single hinge pendulum, situations with less friction have a smaller response of the angle of the top part of the pendulum. The lower the value of the applied friction, the larger the relative angle between the top and bottom pendulum is. These results can be translated into the analysis of different energy components that make it possible to distinguish between elastic and plastic behaviour. Compared to the single hinge pendulum, the elastic energy of the pendulum decreases with decreasing values of the frictional torque. However, at values of the frictional torque below 3 Nm, the inertia of the pendulum influences its motion and the values for the elastic energy increase again. The dissipated energy in the friction hinge, modelling plastic energy, decreases with increasing frictional torque when the torque is larger than 2 Nm. The most surprising influence of FSI on the behaviour of the pendulum can be seen in the energy transferred from the wave to the structure, called ‘total absorbed’ energy. The total absorbed energy decreases with increasing frictional torque. This means that when a structure allows for more plastic deformation, the energy that will absorbed in total is larger.

The reduced-order model can predict the behaviour of the elastic and plastic energy transfer. It can not predict the behaviour of the total absorbed energy accurately. The model can predict the influence of the length of the pendulum on the behaviour of the energy components. For the different waves it can not always correctly predict the differences in transferred energy. This observation induces the most important recommendation of this research, which is based on the way the waves are modelled. In the current model only small deformations of the free surface are assumed, which is not sufficient to represent the waves in the experiment. Using irrotational incompressible inviscid flow, wave breaking can be simulated, likely resulting in a better prediction of the differences in pendulum behaviour between the three focus locations. This is expected to result in a better agreement between the model and experiment.

Preface

This thesis is written to obtain the Master of Science degree in Marine Technology at the Delft University of Technology. The conducted research is about the influence of plasticity, which is simulated with a frictional torque, on the behaviour of a double pendulum subjected to breaking waves. This document is for everybody who is interested in simple modelling of fluid-structure interaction in waves.

I would like to thank my supervisor Reinier Bos for his guidance during my project. Thank you for all the moments you were available to answer my questions, ask my own questions to me in a different way or even program a simple problem together. You were always critical, but also let me know if you thought that something was good. Also, I would like to thank Peter Wellens for his feedback from a different view during important moments, his aid with generating the waves in my experiments and his stimulation to aim for a better grade. Last but not least, I would like to thank my two external committee members Henk den Besten and Farbod Alijani for assessing the quality of my work.

Besides my graduation committee, I would like to express my gratitude towards everyone that works next to the towing tank at 3Me and who helped me to make my experiments successful. With this, I mean evaluating or constructing my setup, assessing the behaviour of the pendulum, or just taking my mind of the experiments during the breaks. I would like to especially thank Peter Poot for his critical view on my setup and overview of the situation, Jasper den Ouden for his high precision and all the effort during the preparation phase of my experiments and Pascal Taudin Chabot for fabricating specific components for my setup, helping me to rearrange my setup or having a chat when the days of executing experiments became quite long.

Furthermore, I would like to thank my friends for placing my subject and thoughts into perspective, for being interested in my thesis and for (digital) coffee or lunch breaks even during these difficult times of COVID-19. Also, thanks to my roommates for the tea breaks, relaxing evenings and for cheering me up in the moments I needed it, during this period of working from home. Thanks to my mum and dad for always supporting me and believing in me during the entire 6.5 years of my study. And of course, Koen, thank you for your endless support, for always staying calm and for proofreading parts of my thesis.

Renée van Zanten
Delft, December 2020

Contents

List of Figures

List of Tables

Nomenclature

Roman Symbols

Subscript i can be 1 or 2, referring to the top and bottom part of the pendulum, respectively. Subscript j can be 1, 2 or 3, referring to the three WHMs.

A	Wave amplitude	m
a	Horizontal acceleration of fluid particle	ms^{-2}
A_c	Frontal area of the cylinder	m^3
c	Phase velocity of the wave	ms^{-1}
C_d	Drag coefficient	-
c_g	Group velocity of the wave	ms^{-1}
c_i	Damping coefficient of the pendulum	Nms
C_l	Frictional constraint used in Lagrange's equation	rad
C_m	Added mass coefficient	-
D	Cylinder diameter	m
d	Water depth	m
D_l	Rayleigh dissipation function used in Lagrange's equation	Nms^{-1}
g	Gravitational acceleration	ms^{-2}
E_{abs}	Total absorbed energy by the pendulum	J
E_{diss}	Dissipated energy in the friction hinge of the pendulum	J
E_{el}	Elastic energy of the pendulum	J
E_{kin}	Kinetic energy of the pendulum	J
E_{pot}	Potential energy of the pendulum	J
E_{stor}	Stored energy of the pendulum	J
F_f	Friction force	N
F_{impact}	Wave impact force	N
F_m	Force resulting from the Morison equation	N
F_n	Normal force	N
F_{wave}	Horizontal wave force	N
H	Wave height	m
h_i	CoG height of pendulum	m
I_i	Mass moment of inertia	kgm^2
k	Stiffness, restoring force coefficient (In relation to pendulum)	Nm
	Wavenumber (In relation to waves)	m^{-1}
L_i	Length of pendulum	m
L_l	Lagrangian, $T_l - V_l$, kinetic - potential energy used in Lagrange's equation	J
M_{aim}	Aimvalue for frictional torque in the experiment	Nm
M_f	Frictional torque	Nm
m_i	Mass of pendulum	kg
p_{atm}	Atmospheric pressure	Pa
Q_i	Generalised force used in Lagrange's equation (In relation to EoM)	Nm
	1st and 3rd quartile (In relation to results)	-
q_i, $\dot{q}_i$	Generalised coordinates used in Lagrange's equation	rad
R	Cylinder radius	m
T	Oscillation period (In relation to pendulum)	s
	Wave period (In relation to waves)	s
t, dt	Time, time step	s
T_l	Kinetic energy used in Lagrange's equation	J

u	Horizontal velocity of fluid particle	ms^{-1}
v, $\dot{v}$	Wave speed and acceleration relative to the pendulum	ms^{-1}, ms^{-2}
V_c	Volume of the cylinder	m^3
V_l	Potential energy used in Lagrange's equation	J
W	Width of the cylinder	m
W_f	Frictional work	J
x_{focus}	Focus location of the wave in the tank	m
x_i	Local horizontal coordinate of pendulum CoG	m
x_j	Location in the tank of the WHM	m
x_{nut}	Local coordinate used for adjusting friction mechanism	mm
y, $\dot{y}$	Coordinates used for time integration	rad, $rads^{-1}$, $rads^{-2}$
y_i	Local vertical coordinate of the pendulum CoG	m

Greek symbols

Subscript i can be 1 or 2, referring to the top and bottom part of the pendulum, respectively.

β	Wetness parameter	-
ϵ	Strain	-
ϵ_w	Phase of regular wave	rad
η	Wave elevation	m
η_b	Maximum elevation of the free water surface for breaking wave	m
θ_i, $\dot{\theta}_i$, $\ddot{\theta}_i$	Angle, angular velocity and angular acceleration of pendulum	rad, $rads^{-1}$, $rads^{-2}$
λ	Curling factor (In combination with η_b)	-
	Wavelength	m
λ_{check}	Theoretical frictional torque used to check slip/stick condition	Nm
μ	Friction coefficient	-
ρ	Water density	kgm^{-3}
σ	Stress	Pa
σ_l	Frictional torque used in Lagrange's equation	Nm
ω	Wave frequency	$rads^{-1}$

Abbreviations

CFD	Computational Fluid Dynamics
CoG	Centre of Gravity
EoM	Equation(s) of motion
FE	Finite Elements
FSI	Fluid-Structure Interaction
SPH	Smoothed Particle Hydrodynamics
SWL	Still Water Level
WHM	Wave Height Measurer

1

Introduction

Waves impacting on maritime structures can cause damage which endangers the environment around these structures. In the past, several catastrophes are documented to be a result of structural failure due to extreme wave conditions. In 2005, hurricanes Katrina and Rita raged over the Gulf of Mexico, which was the working area of 4000 drilling platforms. Their extreme waves and weather conditions caused structural damage to more than 100 of these platforms (Chang et al., 2017). The clean-up activities of the debris and 30.2 million litres of oil continued for over a year (Davidson, 2019). Unfortunately, as reported in 2019 by (Davidson, 2019), no one is held responsible for this large oil spill and the impact on the ecosystems due to structural failure.

Fluid-structure interaction (FSI) plays an important role in this harmful event based on structural failure. Improving the understanding of the influence of plasticity on FSI, which is a key concept in this research, has an impact on different societal problems. First of all, catastrophic events like those during Katrina and Rita can be prevented by creating a better estimation of the capacity of the structure. This leads to less debris in the seawater and fewer repair visits needed, which means less disturbance of the sea life. Next to this, less failure leads to less spill of harmful materials in the seawater. When taking the improved estimation into account in the design process, the current over-designing can be reduced, resulting in less consumption of materials. This reduction leads to less expensive constructions and a smaller impact on the resources of the earth. Another practical benefit of the improved comprehension is that a more extensive and time-consuming analysis could be compared to the results found in this research.

An even more important potential result of the improved understanding is the prevention of loss of human lives in disastrous events. It is crucial to guarantee the safety of people (on ships and offshore structures). A better understanding of extreme loads on these structures and their plastic response can play an important role in this safety. Other disciplines in which human lives are affected, such as biomedical engineering, could also benefit from this research (van Loon and van de Vosse, 2010).

In existing research, extensive analysis of hydro-elastic interaction between regular or breaking waves and walls, and vertical or horizontal cylinders is carried out, shown in section 1.1. The goal of this research will be established using the clear gap in this existing research, which are shown in sections 1.3 and 1.2. In section 1.4 the outline of the rest of the report can be found.

1.1. State of the art

The research of Sarpkaya (1979) examines the impact of a sinusoidally oscillating free surface on horizontal cylinders. It states that the force exerted on the cylinder can not be seen separately from the dynamic response. Namely, this dynamic response can amplify the slamming-force coefficient significantly. Based on this statement, this literature review focuses on FSI in both a hydro-elastic as well as a hydro-plastic manner in section 1.1.1 and 1.1.2, respectively. These two sections focus on impact situations, so FSI in fully submerged cases will not be considered in this research. This is because the loads of these impact situations are often not well understood due to large and highly uncertain impact components (Haley et al., 2014; Dalton and Nash, 1976). Breaking waves are more

complex and variable than regular waves, leading to a principal focus on breaking waves in these sections.

1.1.1. Hydro-elastic analyses

Different forms of breaking waves impacting on a structure have been observed and named, namely the slosh impact, flip-through impact, air pocket impact and aerated impact, which are summarised by Hofland et al. (2010). The air pocket impact wave is often called a plunging wave as well. These four wave impact types are shown in figure 1.1. Another wave impact form described by Hattori et al. (1994) is the vertical wavefront impact.

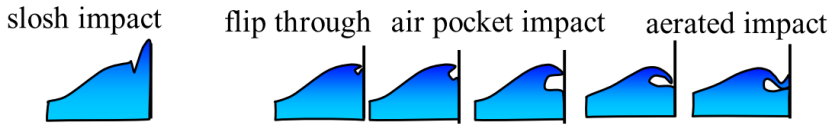

Figure 1.1: Different wave impact types as summarised by Hofland et al. (2010). The air pocket impact is often called a plunging wave.

Some observations are not specific for one breaking wave type but apply to more wave types. An early result on flip-through, vertical wavefront and plunging wave collision shows that the pressure increases when a small amount of air is included. When the wave is more of a plunging type, more air is trapped, and the pressure oscillations that occur are damped (Hattori et al., 1994). The more trapped air, the larger the rise time and duration of the impact force (Bullock et al., 2007).

Some results are only presented for a plunging wave, but again the importance of trapped air is shown. The impacts on a vertical wall can be decomposed into a part due to the dynamics of the trapped air and a part due to the hydrodynamics (Chan and Melville, 1988). Not only the size but also the distribution of the load is significantly influenced by the presence of trapped air (Tsaousis and Chatjigeorgiou, 2020). A numerical simulation based on potential flow shows good predictions (after scaling) for this situation (Zhang et al., 1996). Experimental results show that the influence of air bubbles for the plunging wave impact is also significant on a vertical cylinder. The influence of these bubbles increases when the breaking wave is more developed before the impact, resulting in a larger impact pressure (Ha et al., 2020).

The magnitude of the impact does vary with the cylinder elevation and the horizontal position with respect to the wave. A more severe impact is observed when the radius of the cylinder is similar to the radius of curvature of the water surface (Prasad et al., 1994). Next to this, the impact force is highest when the cylinder is located just below the crest level of the wave and the lowest when the wave breaks behind the cylinder (Kamath et al., 2016). This paper also presents an inverse relation between the rise time with respect to the impact duration and the distance between the cylinder and the breaking location.

A semi-analytical solution for a steep wave impact on a vertical cylinder is given by Tsaousis et al. (2020), addressing the water-entry phase of a wave impact. It shows that by using linear potential theory, a 3D Wagner approximation can be established that shows results in between the 2D von Karman and 2D Wagner results. These results are both related to the velocity squared, but the force using von Karman is half the value of Wagner due to the inclusion of the jet region in the latter (den Besten, 2019). Peregrine (2003) also shows that irrotational inviscid incompressible flow is a good description of many water-wave impacts. When this steep wave is close to breaking, it becomes unclear in which direction the impact force acts (Haley et al., 2014).

Waves will break when they become too steep and other formulations apply for the wave load. The impact force on a pile exerted by a breaking wave consists of two parts: a large “quasi-impact force” with a short duration and a slowly varying force (Wiegel, 1982). The impact load can be modelled using a curling factor λ to indicate the height of the impact area as a function of the wave height. This indicates that the dynamic part can be related to the mass of an amount of water impacting on the cylinder. The curling factor is used in other studies as well (Goda et al., 1966; Wienke and Oumeraci, 2005; Wienke et al., 2005). The slowly varying part can be estimated by the so-called Morison equation. This semi-empirical formula gives the force of an unbroken surface wave exerted on the submerged part of a vertical cylindrical object that reaches from the bottom to above the wave crest. This solution, addressing the submerged phase of a wave impact, consists of a drag force, which is approximately

the same as for steady flow, and a virtual mass contribution caused by the mass of the displaced water (Morison et al., 1950). This result is used in other research that shows that this formulation is also applicable to other geometries such as a horizontal cylinder (Bos and Wellens, 2020; Haley et al., 2014). The fact that this expression, originally meant for vertical piles, is also applicable to other geometries, can be explained by looking at the formulation of the Morison equation. This formulation is, among others, a function of the diameter and cross-sectional area, integrated over the height. This explanation has lead to the inclusion of principles on walls, and vertical and horizontal cylinders in this literature review.

An adjustment to the formulation by Morison et al. (1950) is made by Davies and Martin (1990). This research shows mathematical formulations for the vertical and horizontal forces on a large-diameter horizontal cylinder, which are deduced from experimental results. A large backward horizontal force is analysed, which is ascribed to high added mass coefficients. Another research shows that the regular waves, also used in the papers above, do not create a large and impulsive slamming response (Dalton and Nash, 1976).

The loads discussed above can cause large deflections of structures. The maximum deflection on a vertical cylinder is induced by a moderate plunging wave. The deflection in this situation is 1.5 times larger than for non-breaking waves, while the impact force is almost 5 times larger (Manjula et al., 2012). The amplitude of an oscillating pendulum can be seen as a model for the deflection of a structure. OpenFOAM software gives good agreement with experiments when applied on a free oscillating pendulum in still water (Kotsur et al., 2014).

1.1.2. Hydro-plastic analyses

If loads become too high, the material enters the plastic regime. This phenomenon could leave the structure with little residual strength, resulting in structural failure. The behaviour in the plastic regime is different than in the elastic regime, causing the structure to influence the wave loading differently. This type of FSI is called hydro-plastic analysis and is less investigated than hydro-elastic analysis. The first analytical method of hydro-plastic slamming is given for a flat or nearly flat water impact on beams and stiffened panels. This analytical model is of good accuracy when validated with experiments and numerical simulations (Yu et al., 2019a,b). An example of extensive CFD calculation is the FE/SPH modelling of an extreme wave on a structure. This model uses non-linear fluid and structural behaviour and simulates structural collapse due to water loading, which is validated by large scale experiments (Campbell and Vignjevic, 2012).

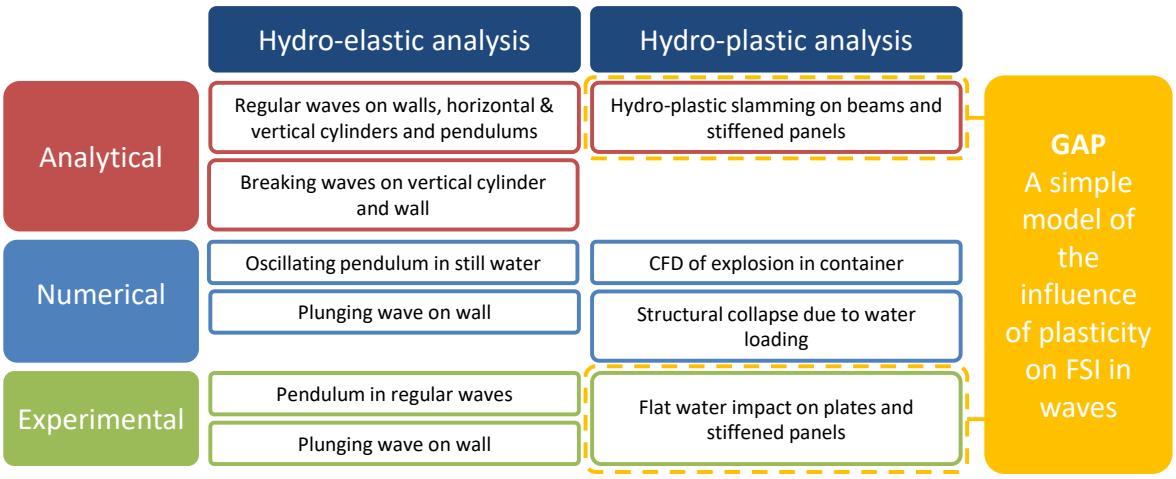

Figure 1.2: A summary of the analysed previous research is shown. Previous research can be divided into hydro-elastic and hydro-plastic analysis. Hydro-elastic analysis is frequently described in literature in an analytical, numerical or experimental way. However, hydro-plastic analysis is more scarce. It can be seen clearly that generating a simple approximation for the influence of plasticity on FSI in waves would partially close the gap observed.

1.2. Gap analysis: a simple model of the influence of plasticity on FSI in waves

By summarising the analysis from the previous section, a gap analysis of current research is performed in this section. As shown, a lot of different research has been executed on FSI. Most of the research captures the elastic behaviour of the structure that is subjected to waves. Yu et al. (2019a) state that in wave impact situations the coupling of the elastic responses of the structure and the hydrodynamic pressure is important. When loads become too high and plastic response occurs, hydro-plasticity occurs, meaning that this plastic response is strongly coupled with the hydrodynamic pressure. Between the existing literature and a simple approach for a coupling of the plastic response of a structure and the wave influence a gap is clearly present, which is shown in figure 1.2. The meaning of 'simple' is a focused or dedicated model of which the properties are known and that can be used to investigate only the influence of FSI. Research in this area has to be conducted to create a safer environment, reduce overconsumption of resources and lead to fewer environmental accidents. Generating a simple approximation for the influence of plasticity on FSI in waves would be a first step towards a better understanding of the interaction between hydrodynamic loading and constructions that deform plastically.

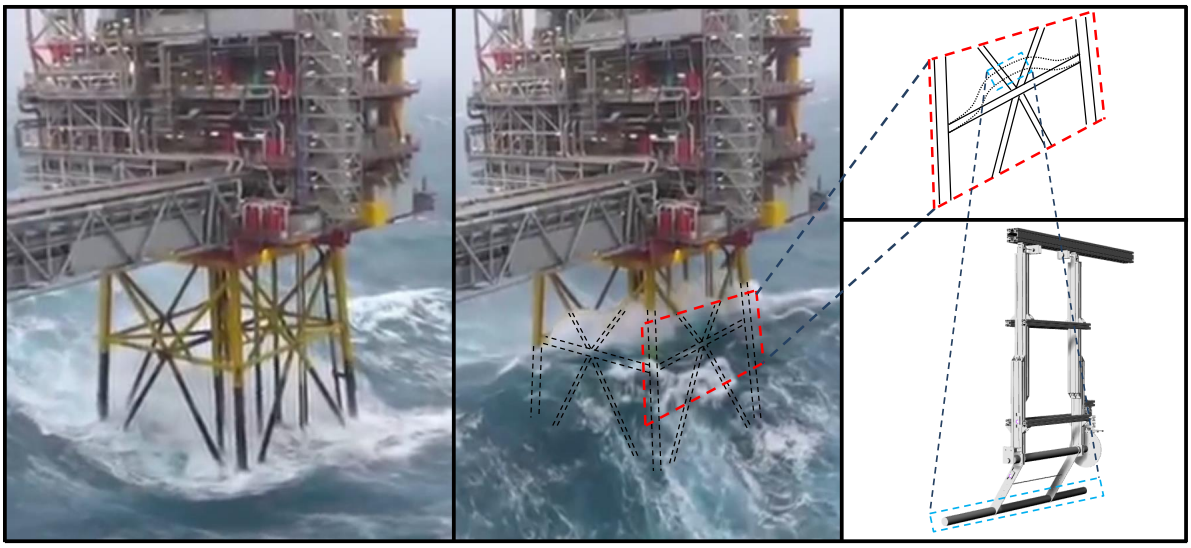

Figure 1.3: This figure shows a horizontal brace of an oil rig that is hit by a large wave. The assumed deformation of this brace is shown on the top right of the figure. The middle of this deformed brace can be modelled as the cylindrical end of a pendulum as shown in the bottom right of the figure. The motion of this pendulum is a measure for the deformation of a beam-like structure. *Source images: (Top Fives, 2018)*

1.3. Research goal

To close the gap indicated in the previous section, a simple approximation for the influence of plasticity on FSI in waves should be found. Based on the example given earlier, an oil rig in extreme weather conditions is used as an example situation to find this simple approximation. An oil rig that is hit by a large wave is shown in figure 1.3. When a horizontal brace of this oil rig is selected, one can image that it will deform in the way shown in the top right of the figure. The middle of this brace stays approximately straight, which can be selected as the part that will be observed. This specific part of the brace can be modelled as the cylindrical end of a pendulum as shown in the bottom right of the figure. The motion of this pendulum is a measure for the deformation of a beam-like structure. Therefore, the influence of plasticity on FSI in waves can be analysed using a simple pendulum that allows plastic deformation as well. This pendulum will be exposed to impact loads in the form of breaking waves. In this research, the pendulum is chosen because of its ability to show clear and easy to interpret results due to its few degrees of freedom.

The desire to close the gap can be translated into a goal with accompanying research questions which are shown in section 1.3.1. Then, the hypotheses for this research are shown in section 1.3.2. The scope of the total research is given afterwards in section 1.3.3.

1.3.1. Research questions

This research aims to find a model for the influence of plasticity on FSI. This goal will be reached by investigating a simple pendulum that allows plastic deformation that will be exposed to impact loads in the form of breaking waves. The desired output of these investigations is to capture the energy transfer and absorbed energy in the plastic deformation in different situations. To obtain this information in a structured manner, the main research question is formulated and clarified using sub-questions.

What is the influence of plasticity on the behaviour of a pendulum in breaking waves?

1. What are the typical conditions when breaking waves are formed? How can these waves be modelled?
2. How can a simple pendulum be adjusted to allow plastic deformation? How can this be implemented in a reduced-order or experimental approach?
3. When measuring the energy transfer from the waves to the pendulum, which energy components can indicate the influence of plasticity in the result?

1.3.2. Hypotheses of this project

In order to predict the result of the research, two hypotheses are constructed to answer the main question.

1. The influence of the plastic deformation of the pendulum causes energy absorption. It is expected that situations with a higher resistance to plastic deformation absorb less plastic energy when loaded with the same wave. Next to this, pendulums with a higher stiffness are expected to absorb more energy while plastic deformation occurs.
2. Variability in the transferred energy could indicate the importance and influence of the plasticity on the behaviour. However, the variability could also be a result of the different amounts of trapped air in the breaking wave.

1.3.3. Scope of this project

Due to the combination of time limitations and numerous interesting focus points, the project's scope is defined in this section to create more guidance for the project. It is assumed that this scope can give an outcome of this research that can also be applied on full-size ship and offshore structures. The assumptions, limitations and focus points presented, will be categorised in two parts: those applicable on the fluid and those applicable to the structure.

Fluid

- It is assumed that the vertical elements of the pendulum will not receive a contribution from the hydrodynamic force. The cylindrical part of the pendulum will be almost the full width of the fluid domain. Therefore, the problem can be evaluated as a 2D problem.
- Only breaking waves will be analysed, no monochromatic waves. This is because the large impact of breaking waves is more likely to cause plastic deformation. Large impacts are related to severe and extreme conditions which influence the Ultimate Limit State. Based on previous experiments with the pendulum, the wave height will be approximately 15 cm. The wave used to create a breaking wave will be focused at three different locations in front of the pendulum.
- The influence of trapped air is important on the rise time or peak of impact pressure as discussed in section 1.1. Therefore, it is aspired to implement this influence.

Structure

- It is assumed that the vertical elements of the pendulum will not receive a contribution from the hydrodynamic force. The cylindrical part of the pendulum will be almost the full width of the fluid domain. Therefore, the problem can be evaluated as a 2D problem.
- The structure consists of one pendulum that allows both elastic as well as plastic deformation. The start of the design of the pendulum is based on previous experiments by Bos and Wellens (2020).
- Only the plastic regime before the ultimate strength is reached is analysed. This restriction means no necking will occur. The stress-strain curve can depend on for example the temperature, pretreatments of the material, the material properties and the strain rate. Only the influence of the material properties will be implemented.

1.4. Outline of the report

The next chapter, chapter 2, describes a reduced-order model which is used to design the experimental setup described in chapter 3. Some improvements to the model are also presented in chapter 2 after comparing the results of the experiment and the model. The evaluation of the experimental results and the results of the improved model are presented in chapter 4. The final chapter of this research, chapter 5, consists of the conclusions and recommendations for this report.

2

Reduced-order model of pendulum in breaking waves

A reduced-order model is a good medium to discover the principles of a certain situation without long calculation time or complex equations. In chapter 1, the central problem of this research is introduced and it is indicated that analysing a simple model that allows plastic deformation loaded by waves can aid in the assessment of maritime structures in waves. The model of a pendulum that will be used is based on research by Bos and Wellens (2020). In their research, a pendulum is located above the free surface and subjected to monochromatic waves. The phases that are captured in the experiment are water entry, submerged behaviour and water exit. The amplitude of the pendulum is presented for different wavelengths, which show the different influences of fluid-structure interaction (FSI). A reduced-order model combined with a wetness factor and coefficients determined by Sarpkaya (1986) shows good performance when compared to experiments.

A short description of fluid and structural behaviour is given in section 2.1 which is essential knowledge for understanding this project. Then, a justification is given of the fundamental principles applied in the model in section 2.2. Based on these principles, two different models are constructed and discussed. The first model is used for the design of the experiment and first comparison with the results, which is described in section 2.3. A second, improved, model is used for final comparison with experimental results. The adjustments made to the first model are shown and explained in section 2.4.

2.1. A concise description of the behaviour of structures and waves

It is necessary to know and understand the physics behind structural and fluid behaviour before a reduced-order model is composed. In this section, both are described briefly before continuing to implement this knowledge into the model. The basic principles of this structural behaviour are described in section 2.1.1. Then, the basic principles of the waves are shown in section 2.1.2.

2.1.1. Structural behaviour: elastic and plastic regime

Two important terms when introducing structural behaviour are stress and strain. The stress is a measure for the internal forces in a material, and the strain is the deformation of the material with respect to its original shape. Now the stress-strain diagram of a ductile material can be analysed, shown in the left diagram of figure 2.1. When a load is applied, the stress and strain increase according to a linear relationship that is prescribed by the Young's Modulus of the material. This part of the curve is called the elastic regime. When a load is applied that causes stress higher than the yield strength, the material enters the plastic regime. In this regime, the relationship between stress and strain is non-linear. After reaching the ultimate strength, necking of the structure occurs, and the stress in the material decreases until failure of the structure.

In the right diagram of figure 2.1, the behaviour of the stress-strain curve is shown in the situation that the material is unloaded and loaded again. When the structure is unloaded in the elastic regime, it will follow the linear relationship returning to its original shape. However, if unloading occurs while the material is in the plastic regime, the stress-strain curve will go down from that exact point in a linear

relationship. This response leads to a permanent deformation when the load on the structure is equal to zero. When the structure is loaded again, it will follow this new linear line until it reaches the point of unloading. Then, the stress will follow the original stress-strain curve. In the second load cycle, the stress at which a non-linear behaviour is initiated is higher than the yield strength. This increased maximum value for linear behaviour is due to a process called strain hardening and is also indicated in the left diagram of figure 2.1.

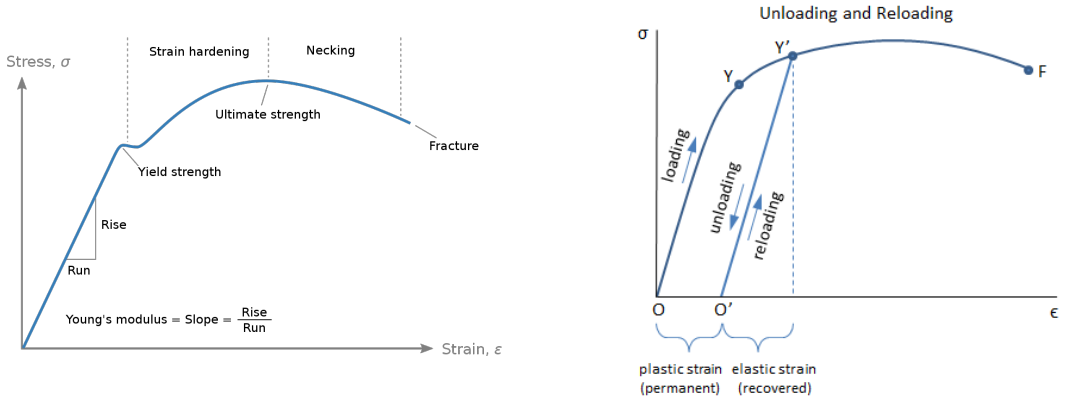

Figure 2.1: The stress-strain diagram of a ductile material is shown in the left of the figure. The behaviour of the stress-strain curve when the material is unloaded and loaded again is shown on the right. This image shows the process of strain hardening. *Source of images: (Wikipedia, 2020) and (MechaniCalc, 2020)*

2.1.2. Behaviour of waves: linear and non-linear waves

The most simple form of a wave is a regular wave. Assuming this wave satisfies potential theory and only small amplitudes occur, the wave elevation on any moment or location can be given by equation 2.1. This is visualised in figure 2.2.

$$\eta(t) = A\cos(kx - \omega t + \epsilon_w) \tag{2.1}$$

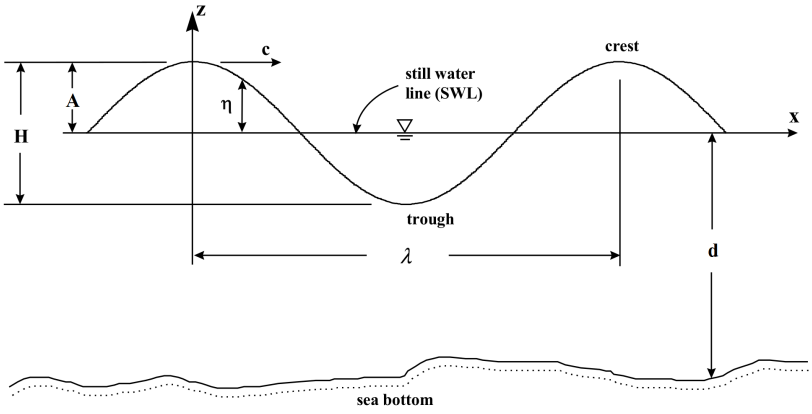

Figure 2.2: A schematic drawing of a regular wave in which the important parameters are η (wave elevation), A (wave amplitude) and λ (wavelength). Furthermore, the depth of the water is indicated with d. *Source of original image: (Montanari, 2017)*

In this equation and figure, A is wave amplitude, k is the wavenumber equal to $2\pi/\lambda$ in which λ is the wavelength, x is the location, ω is the frequency, t the time and ϵ_w the phase of this wave component.

When assuming a linear behaviour of the wave, the wavenumber (and therefore the wavelength) and the frequency are related according to the dispersion relation given in equation 2.2.

$$\omega^2 = kg\tanh(kd) \tag{2.2}$$

In these linear waves, two different velocities can be indicated. The first velocity is the propagation speed of a top of the wave, which is called the phase velocity, given in equation 2.3. The equation shows that long waves travel faster than short waves.

$$c = \frac{\lambda}{T} = \frac{\omega}{k} = \frac{g}{\omega}\tanh(kd) \tag{2.3}$$

The second velocity is the propagation speed of the wavefront or the total wave group, which is called the group velocity. This formulation for this velocity is shown in equation 2.4. The value of n is always smaller than 1 and, therefore, individual waves travel through the wave group. They appear at the end of a wave group, travel forward and disappear at the front of the wave group (Holthuijsen, 2007).

$$c_g = nc = \frac{1}{2}\left(1 + \frac{2kd}{\sinh(2kd)}\right)\frac{g}{\omega}\tanh(kd) \tag{2.4}$$

An advantage due to the assumed linearity is that different regular wave components can be summed, resulting in the equation shown in equation 2.5.

$$\eta(t) = \sum_{i=1}^{n} A_i \cos(k_i x - \omega_i t + \epsilon_{w,i}) \tag{2.5}$$

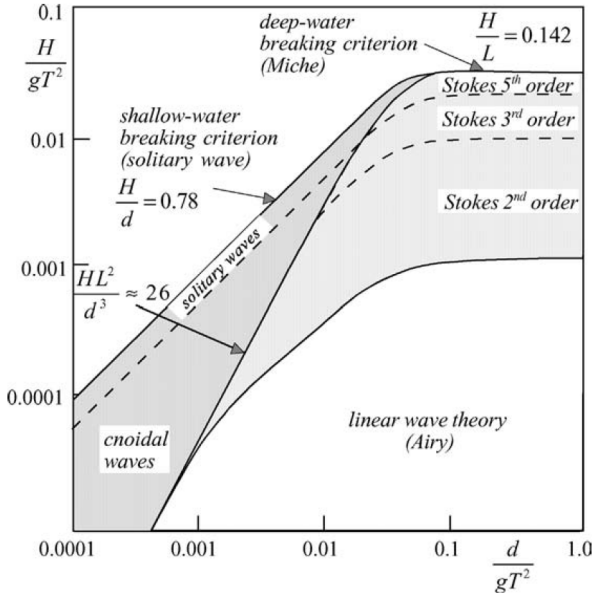

Figure 2.3: The applicability of different wave theories in different wave conditions. Originally published by Méhauté (1976), but this version is retrieved from Holthuijsen (2007).

However, not all waves are linear due to, for example, shallow water effects or steepness of the wave (H/λ). The applicability of different wave theories is dependent on wave height, wave period and depth of the water and is shown in figure 2.3 (Méhauté, 1976). In this figure, L is equal to the wavelength, so it will be indicated here by λ. The Airy wave theory consists of the waves shown in figure 2.2. If the water is shallow and $H\lambda^2/d^3 > 26$ cnoidal waves are formed. For increasing steepness in deep water Stokes waves of 2nd, 3rd or 5th order are formed. Both the cnoidal as well as the Stokes waves consist of waves with sharper crests and flatter troughs.

When steepness even further increases, solitary waves in shallow water will break if $H/d > 0.78$. In deep water, all waves will break when $H/\lambda > 0.142$. Generating a controlled breaking wave directly with a wavemaker is difficult or even impossible. Therefore, groups of monochromatic waves, which can be generated accurately, should be combined to create a steep wave. This steep wave, also called a focused wave, can be generated using dispersive focusing. This procedure is used in numerous studies showing, for example, the evolution of free and bound waves or freak waves in numerical and

experimental ways (Vyzikas et al., 2018; Wu and Yao, 2004). If the steepness of this focused wave exceeds the maximum a breaking wave is generated. Some different forms of breaking waves are discussed in section 1.1.

2.2. Explanation of the fundamental ideas of the model

A pendulum that allows elastic as well as plastic deformation will be subjected to a breaking wave. The breaking wave will be constructed as described in section 2.1.2, by addition of wave components. These wave components will be focused at one location due to dispersive focusing. The fundamentals of a simple model of a pendulum that allows for plastic deformation should be explained in more detail. The method of modelling plastic deformation is shown in section 2.2.1. Then, a justification of the use of a pendulum is done in section 2.2.2.

2.2.1. Incorporation of plasticity

When loads on a structure become too high, the structure deforms in an inelastic or plastic way. Different theoretical models are created using dislocation theory. Two plasticity models presented by Lubliner (2008) are given here. The first model is the *Yield Stress Theory* which assumes that the yield stress is equal to the value of the shear stress required to supply enough energy to the dislocations to start moving. The second model is the *Yield Point Theory* which assumes that a higher stress needs to be overcome to initiate the motion of the dislocations. After that point, a lower stress is required for dislocation movement.

These two models can be approximated mechanically as well. Different models for friction between two surfaces exist. These friction models show significant similarity to the plasticity theories described by Lubliner (2008). When this friction is modelled as Coulomb friction, the friction force is constant. The formulation for this is equal to $F_f = \mu F_n$. This formulation means that the friction force is equal to a coefficient of friction times a force normal to the two frictional surfaces. If this frictional force is representing the *Yield stress theory*, μ has only one value, but when the difference between the static and dynamic friction coefficient is taken into account, the friction represents the *Yield point theory*. The fact that friction models can be used to represent elastoplastic behaviour is also shown by for example Curnier (1984) and Wriggers (2006).

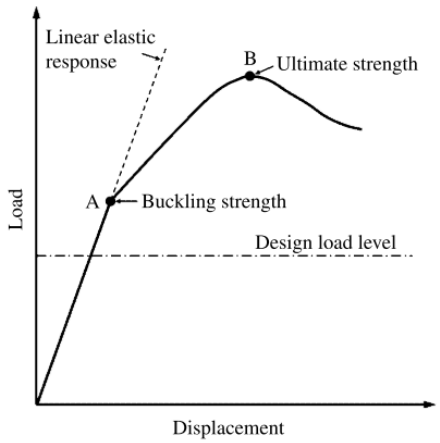

Figure 2.4: Load-displacement curve of a structure. The linear elastic and the non-linear plastic response are shown. *(Source of image (Paik, 2018))*

2.2.2. Usage of a pendulum

An essential first step towards understanding structural failure of ships and offshore structures due to hydrodynamic loading is the analysis of a simple model. An example of a simple mechanical model used for this increased comprehension is a pendulum. When the end of this pendulum is a cylinder, wave impacts on a horizontal cylinder and the accompanying FSI can be investigated. Incorporating friction in a pendulum can be done by using a double pendulum in which one hinge is a friction hinge.

When looking at a typical load-displacement curve of a structure, shown in figure 2.4, it can be seen that the graph consists of lines of different slopes, which can be called stiffness. For the pendulum, the same principles take place, but now, the elastic response is not linear. When the elastic response is taking place, the total pendulum will rotate, but when the plastic regime is reached, the stiffness should become different. Therefore, a plastic hinge is added below the elastic hinge. When the elastic limit is exceeded, the friction in the friction hinge is overcome, and it starts to move, which simulates plastic deformation. The motion leads to a reduction in the stiffness when the bottom part of the pendulum is moving, resulting in a combination of the simulated elastic and plastic deformation. When the pendulum is unloaded, the plastic deformation will remain. It should be noted that the stiffness of the pendulum has been reduced slightly with respect to the original situation.

2.3. The first model used for design of and first comparison with experiment

A reduced-order model is constructed of the double pendulum subjected to breaking waves. In the bottom hinge of the pendulum, friction can be applied to simulate plastic deformation. The first model, which is not perfect, will be used for the design of the experiment and first comparison with the experimental results. After this first comparison, improvements will be made and presented. The equations of motion of the first version of the reduced-order model are given in section 2.3.1. The load due to the waves is estimated in section 2.3.2.

2.3.1. Equations of Motion

A schematic overview of the double pendulum and its coordinates is given in figure 2.5. The top hinge (1) is a normal hinge, and the bottom hinge (2) is the hinge with a frictional contact. The black dots at (x_1, y_1) and (x_2, y_2) are the locations of the centre of gravity of both parts of the pendulum. The model is formulated in terms of two coordinates, namely θ_1 and θ_2. These coordinates are the angles of the top and bottom part of the pendulum with respect to the vertical, respectively. All locations can be expressed as a function of these two coordinates, the height of the centre of gravity of both pendulum parts and the length of the top part of the pendulum. The force due to the waves is assumed to be a horizontal component only.

The equations of motion are obtained by using Lagrange's equation, as shown in equation 2.6. All the separate parts of this formulation are explained below the equation.

$$\frac{d}{dt}\left(\frac{\partial L_l}{\partial \dot{q}_i}\right) - \frac{\partial L_l}{\partial q_i} + \frac{\partial D_l}{\partial \dot{q}_i} = Q_i - \frac{\partial C_l}{\partial q_i}\sigma_l \qquad \forall i = [1,2] \tag{2.6}$$

In which:

L_l = Kinetic energy - potential energy $= T - V$

T_l = Kinetic energy $= \frac{1}{2}m_1(\dot{x}_1^2 + \dot{y}_1^2) + \frac{1}{2}I_1\dot{\theta}_1^2 + \frac{1}{2}m_2(\dot{x}_2^2 + \dot{y}_2^2) + \frac{1}{2}I_2\dot{\theta}_2^2$

V_l = Potential energy $= m_1 g h_1 + m_2 g h_2$

D_l = Rayleigh dissipation function $= \frac{1}{2}c_1\dot{\theta}_1^2 + \frac{1}{2}c_2\dot{\theta}_2^2$ (Agarana et al., 2017)

Q_1 = Generalised force 1 $= F_{wave} L_1 \cos(\theta_1)$

Q_2 = Generalised force 2 $= F_{wave} L_2 \cos(\theta_2)$

C_l = Frictional constraint $= \theta_2 - \theta_1$ (Vallery and Schwab, 2018)

σ_l = Frictional torque $= M_f \operatorname{sign}(\dot{\theta}_2 - \dot{\theta}_1)$ (Vallery and Schwab, 2018)

Above equations can be solved using the following definitions of the locations of the centre of gravity

of each part of the pendulum.

$$
\begin{aligned}
x_1 &= \ h_1 \cos(\theta_1) \\
y_1 &= -h_1 \sin(\theta_1) \\
x_2 &= \ L_1 \cos(\theta_1) + h_2 \cos(\theta_2) \\
y_2 &= -L_1 \sin(\theta_1) - h_2 \sin(\theta_2)
\end{aligned}
$$

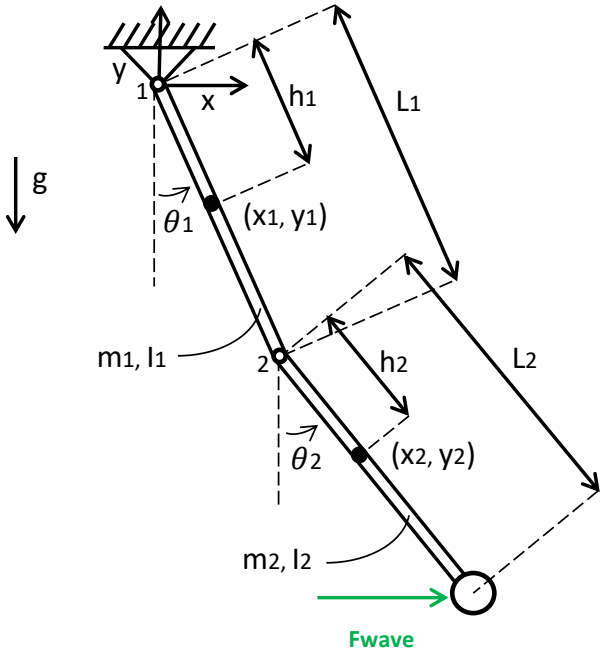

Figure 2.5: A schematic overview of the double pendulum. The black dots indicate the locations of the centre of gravity of both elements of the pendulum at (x_1, y_1) and (x_2, y_2). The model is formulated in terms of two coordinates, namely θ_1 and θ_2. These coordinates are the angles with the vertical of the top and bottom part of the pendulum, respectively.

By further analysing the problem, two cases can be identified: slip or stick of the plastic hinge. Slip means that the bottom pendulum is moving with respect to the top pendulum, and stick means that the relative angle between both parts stays constant. When slip occurs equations 2.7 and 2.8 are valid, resulting from equation 2.6. In these formulations $\lambda = M_f \operatorname{sign}(\dot{\theta}_2 - \dot{\theta}_1)$, in which M_f is the maximum torque that can be utilised in the plastic hinge.

$$
\begin{aligned}
(m_1 h_1^2 + I_1 + m_2 L_1^2)\ddot{\theta}_1 + m_2 L_1 h_2 \cos(\theta_1 - \theta_2)\ddot{\theta}_2 + c_1\dot{\theta}_1 + m_2 L_1 h_2 \sin(\theta_1 - \theta_2)\dot{\theta}_2^2 \\
+(m_1 h_1 + m_2 L_1) g \sin(\theta_1) \\
= F_{wave} L_1 \cos(\theta_1) + \lambda
\end{aligned}
\tag{2.7}
$$

$$
\begin{aligned}
m_2 L_1 h_2 \cos(\theta_1 - \theta_2)\ddot{\theta}_1 + (m_2 h_2^2 + I_2)\ddot{\theta}_2 + c_2\dot{\theta}_2 - m_2 L_1 h_2 \sin(\theta_1 - \theta_2)\dot{\theta}_1^2 + m_2 g h_2 \sin(\theta_2) \\
= F_{wave} L_2 \cos(\theta_2) - \lambda
\end{aligned}
\tag{2.8}
$$

When stick occurs, $\dot{\theta}_1 = \dot{\theta}_2$ and $\ddot{\theta}_1 = \ddot{\theta}_2$, equations 2.7 and 2.8 reduce to one equation shown in equation 2.9. In this equation, no term contains the frictional torque.

$$
\begin{aligned}
(2 m_2 L_1 h_2 \cos(\theta_1 - \theta_2) + m_2(h_2^2 + L_1^2) + m_1 h_1^2 + I_1 + I_2)\ddot{\theta}_1 + (c_1 + c_2)\dot{\theta}_1 \\
+(m_2 L_1 + m_1 h_1) g \sin(\theta_1) + m_2 h_2 g \sin(\theta_2) \\
= F_{wave} L_1 \cos(\theta_1) + F_{wave} L_2 \cos(\theta_2)
\end{aligned}
\tag{2.9}
$$

One of stick or slip can be assumed. First, stick is assumed, and equation 2.9 is integrated over time. Then all the positions, velocities and accelerations are known and can be used to check if the assumption of stick is indeed correct. This can be done by rewriting equation 2.7 or 2.8 and moving λ to one side and renaming it to λ_{check}. When $|\lambda_{check}| < M_f$ the assumption of stick is indeed correct. Otherwise, if $|\lambda_{check}| \geq M_f$, the plastic hinge is slipping and equations 2.7 and 2.8 are integrated over time.

Time integration scheme: Semi-Implicit Euler Method
A relative simple time integration scheme is chosen that has the same amount of steps as a first-order scheme, but a higher accuracy. The chosen scheme is called Semi-Implicit Euler Method and has an overall error of $\mathcal{O}(\Delta t^2)$ (Langtangen and Linge, 2016). The details of the integration scheme are shown, using the situation of the double pendulum as an example. First, the vectors y and $\dot{y}$ are defined in equation 2.10.

$$y = (\theta_1, \theta_2, \dot{\theta}_1, \dot{\theta}_2) \text{ and } \dot{y} = (\dot{\theta}_1, \dot{\theta}_2, \ddot{\theta}_1, \ddot{\theta}_2) \tag{2.10}$$

The integration scheme for the situation in which slip occurs is shown in equation 2.11. For the stick condition, it is shown in equation 2.12. The subscripts are indices of the vectors, while the superscripts are the indicators of the old or new values. The functions ($f_{slip}()$ and $f_{stick}()$) are the function for the second derivative of $\ddot{\theta}_1$ and $\ddot{\theta}_2$ for the slip and stick situation, respectively. These functions are derived from equations 2.7 and 2.8 or 2.9.

$$\begin{aligned} y_1^n &= y_1^o + dt \cdot y_3^o \\ y_2^n &= y_2^o + dt \cdot y_4^o \\ y_3^n &= y_3^o + dt \cdot f_{slip}(y_1^n, y_2^n, y_3^o, y_4^o, \dot{y}_3^o, \dot{y}_4^o) \\ y_4^n &= y_4^o + dt \cdot f_{slip}(y_1^n, y_2^n, y_3^o, y_4^o, \dot{y}_3^o, \dot{y}_4^o) \end{aligned} \tag{2.11}$$

$$\begin{aligned} y_1^n &= y_1^o + dt \cdot y_3^o \\ y_2^n &= y_2^o + dt \cdot y_4^o \\ y_3^n &= y_3^o + dt \cdot f_{stick}(y_1^n, y_2^n, y_3^o, y_4^o, \dot{y}_3^o, \dot{y}_4^o) \\ y_4^n &= y_3^n \end{aligned} \tag{2.12}$$

Required time step: 0.0005 seconds
The only unknown part of the integration is the required time step to obtain sufficiently accurate results. A situation in which the time step is equal to 10^{-5} s, L_1 = 0.65 m, L_1 = 0.40 m and M_f = 1 Nm is taken as the reference situation. Then, results are obtained using different time steps, and their root mean squared error with respect to the reference situation is calculated. These results are shown in figure 2.6. The error occurring at dt = 0.0005 s is considered to be sufficiently small. Therefore, this time step is used in the calculations.

2.3.2. Load due to the waves

No analytical result for a breaking wave force on a horizontal cylinder is present in the current literature. In a similar way as the applicability of the Morison equation, initially meant for vertical cylinders, on other geometries, the breaking wave force on a pile will be applied on a horizontal cylinder (Morison et al., 1950; Bos and Wellens, 2020; Haley et al., 2014). According to Wiegel (1982), this breaking force consists of a slowly varying part and an impact part. The slowly varying part can be approximated using the Morison equation shown in equation 2.13 (Morison et al., 1950). In this formulation C_d = 2.0 and C_m = 1.0. The values for C_m and C_d are chosen in agreement with Bos and Wellens (2020) who modelled the same cylinder.

$$F_m = \rho(C_m V_c \dot{v} + \frac{1}{2} C_d A_c |v| v) \tag{2.13}$$

The velocities and accelerations needed in equation 2.13 are a result of the wave created by ten wave components. The total wave elevation at the focus and, for now, assumed impact location is assumed to be equal to $\eta = \sum_{i=1}^{10} A_i cos(k_i x - \omega_i t + \epsilon_{w,i})$. As shown in section 2.1.2, this equation is only valid

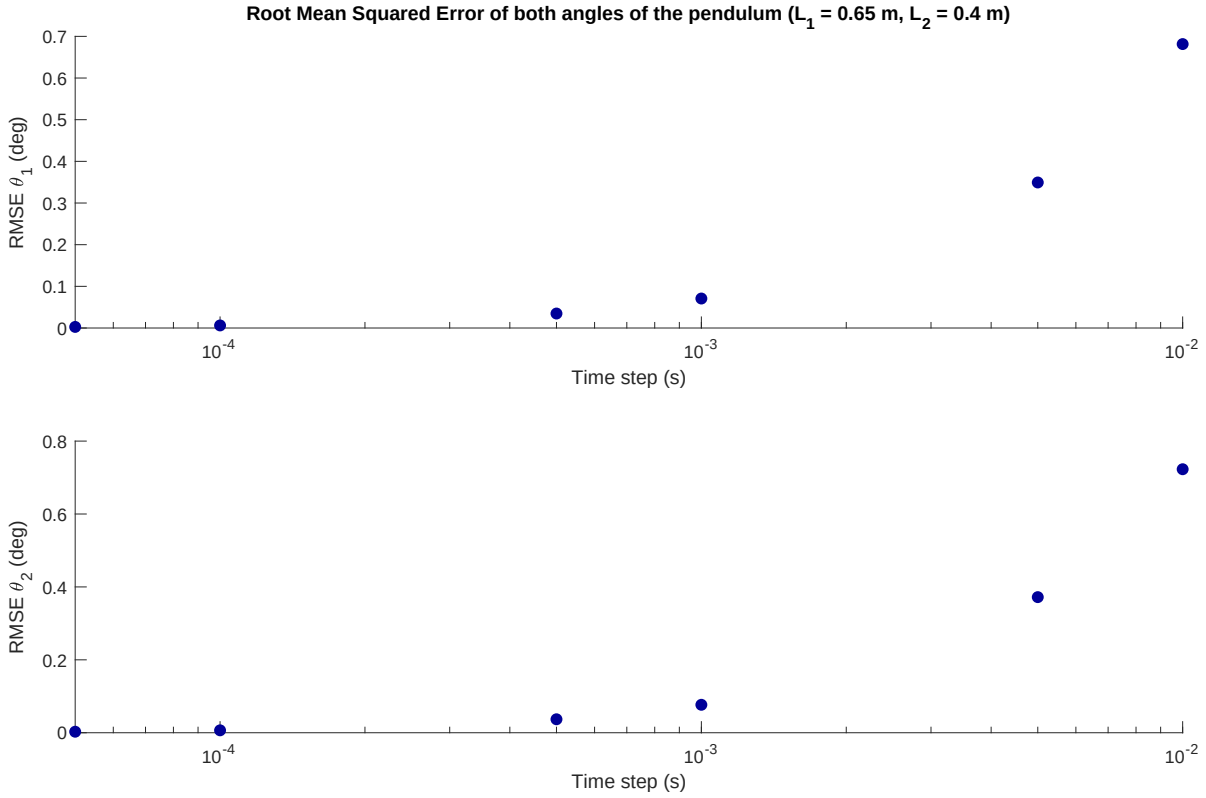

Figure 2.6: The root mean squared error (RMSE) of different time steps compared to the reference situation. In this reference situation dt = 10^{-5} s, L_1 = 0.65 m, L_1 = 0.40 m and M_f = 1 Nm. The masses are based on the properties of the original pendulum described by Bos and Wellens (2020). The error occurring at dt = 0.0005 s is considered to be sufficiently small. Therefore, this time step is selected.

for linear waves, and it does not take into account the different group velocities of the components. However, it is found sufficient as a first estimation for the wave elevation at the focus point. By applying this same assumption about linearity, the results for the combined velocity and acceleration are shown in equations 2.14 and 2.15. A constant extrapolation of the velocity and acceleration at still water level (SWL) is adopted for locations above the SWL. This assumption is based on the accurate performance presented by Bos and Wellens (2020).

$$u = \sum_{i=1}^{10} A_i \omega_i \frac{cosh(k_i d)}{sinh(k_i d)} cos(k_i x - \omega_i t + \epsilon_{w,i}) \tag{2.14}$$

$$a = \sum_{i=1}^{10} A_i \omega_i^2 \frac{cosh(k_i d)}{sinh(k_i d)} sin(k_i x - \omega_i t + \epsilon_{w,i}) \tag{2.15}$$

The Morison formulation is only valid for full submergence. Therefore, the wetness parameter presented by Bos and Wellens (2020) is used to smoothly transition between dry and wet phases of the cylinder. The factor is shown in equation 2.16.

$$\beta = \max\left(\min\left(\frac{\eta - (y - D/2)}{D}, 1\right), 0\right) \tag{2.16}$$

A more elaborate expression of the impact load is taken from Wienke et al. (2005). This research presents the impact load as a function of the curling factor λ and the elevation of the wave. The height of the area of the impact is defined by $\lambda\eta_b$. Since in this situation the area of impact is horizontal, $\lambda\eta_b$ will be replaced by βW in all formulations. The modified impact load formulation is shown in equations 2.17 and 2.18.

$$F_{impact} = \beta W \rho R v^2 \left(2\pi - 2\sqrt{\frac{v}{R}t}\,\operatorname{arctanh}\sqrt{1-\frac{v}{4R}t} \right) \quad \text{for} \quad 0 \le t \le \frac{1}{8}\frac{R}{v} \tag{2.17}$$

$$F_{impact} = \beta W \rho R v^2 \left(\pi\sqrt{\frac{1}{6}\frac{1}{\frac{v}{R}t'}} - \sqrt[4]{\frac{8}{3}\frac{v}{R}t'}\,\operatorname{arctanh}\sqrt{1-\frac{v}{R}t'\sqrt{6\frac{v}{R}t'}} \right) \quad \text{for} \quad \frac{3}{32}\frac{R}{v} \le t' \le \frac{12}{32}\frac{R}{v} \quad \text{with} \quad t' = t - \frac{1}{32}\frac{R}{v} \tag{2.18}$$

The total load on the horizontal cylinder is then equal to $F_{wave} = \beta F_m + F_{impact}$.

2.4. An improved model used for final comparison with experiment

The model used for the design of the experiment was not performing sufficient when compared to the experimental data. Therefore, some adjustments to the model are presented in this section. First, the adjustments made to the equations of motion or structural aspects of the pendulum are given in section 2.4.1. The adjustments made to the load due to the waves are given in section 2.4.2.

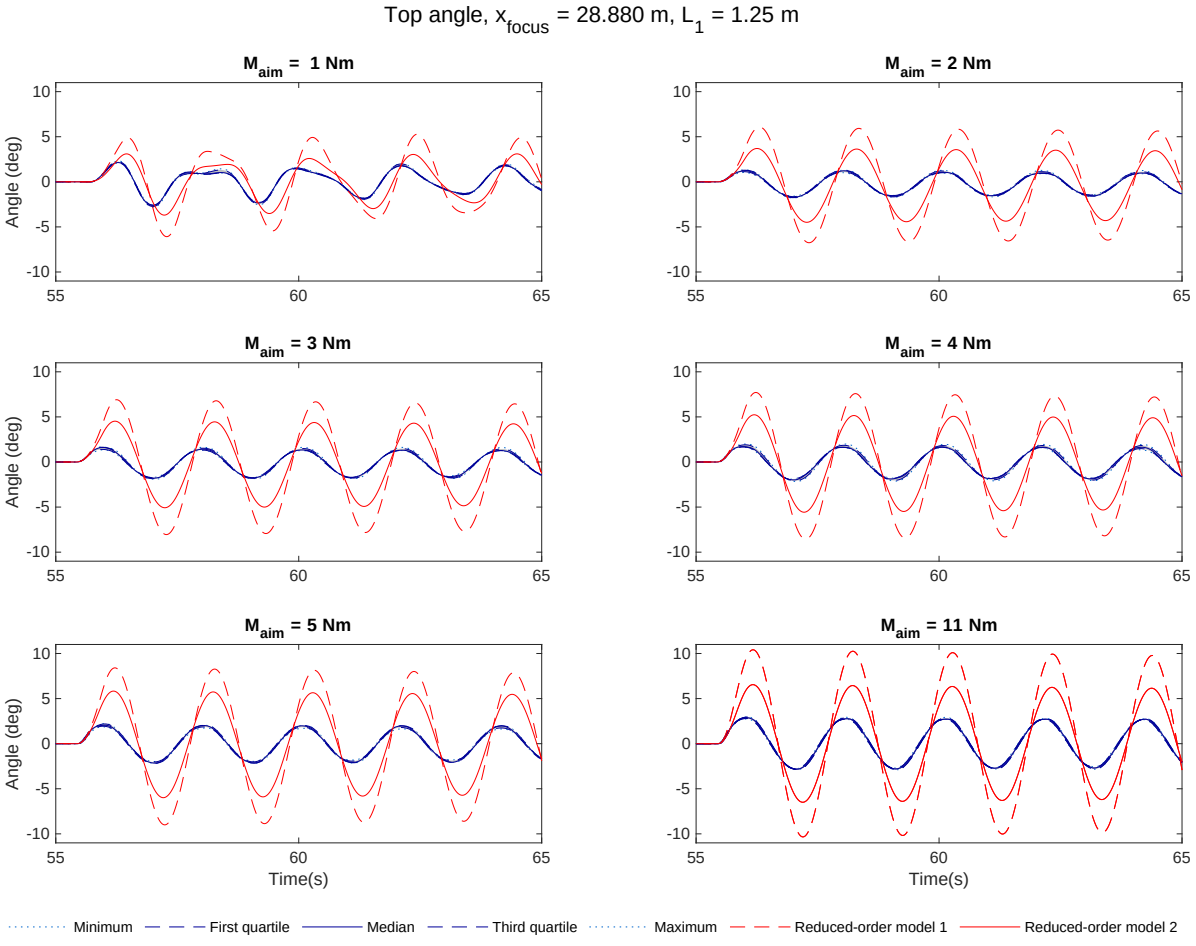

Figure 2.7: Angle of the top part of the longest pendulum subjected to waves focused at x_{focus} = 28.880 m. The time signal is given for six different aim values for the frictional torque varying from 0 Nm to 11 Nm. The top angle shown here simulates the elastic response of a structure. The first reduced-order model overestimates the experimental values severely. The second model estimates a lower top angle, but still overestimates the experimental values.

2.4.1. Equations of Motion

One change is made to the equations of motion, namely the incorporation of the difference between static and dynamic friction. Based on results from the previous model, the average ratio between the dynamic and static friction is found to be 0.81. The difference can be found in the change of the value of λ in equations 2.7 and 2.8, and the accompanying condition for the occurrence of slip or stick. The value of λ becomes equal to $M_{f,dynamic}\,\mathrm{sign}(\dot{\theta}_2 - \dot{\theta}_1)$ in equations 2.7 and 2.8 when slip occurs. Slip will occur when $|\lambda_{check}| \geq M_{f,dynamic}$ or when $|\lambda_{check}| \geq M_{f,static}$ if the stick equations were applied in the previous time step.

Another adjustment related to the equations of motion is done. In early results of the model, fast back-and-forth changes between slip and stick were observed. Therefore, an extra condition is added that guarantees no occurrence of stick for just a singular time step.

2.4.2. Load due to the waves

The results of the first model showed overestimated pendulum behaviour probably caused by a wave force that was too high and long. The angle of the top pendulum of this model is shown in figure 2.7 and the relative angle between the top and bottom pendulum and the torque are shown in figure 2.8. The values for M_{aim} will be explained in section 3.3.3. In both figures, this first model is indicated with 'Reduced-order model 1' and the measured results are indicated in blue. Both the top angle as well as the relative angle are overestimated severely by the model. The signal of the calculated torque is approximately twice as wide as the measured torque. Due to these large deviations, it is decided to adjust the wave conditions.

In a first adjustment, ten wave groups with different amplitude, period and therefore group velocity are modelled using linear equations. Each regular wave group is 3.5 waves long and is either increased to the amplitude or decreased to zero over one period. At the focus point, all the wave components are exactly at the 1.75th wave and are, therefore, in phase. Every wave group travels with their own group velocity, and in each group, the wave propagates according to $A_i \cos(k_i x - \omega_i t)$ with x relative to the focus point. No phase shift is present in this formulation due to the assumption that the waves are focused and in phase at t = 0 s. Unfortunately, this relatively simple model seemed to be too coarse and was still overestimating the behaviour of the pendulum. The results of this model are also shown in figures 2.7 and 2.8, indicated with 'Reduced-order model 2'. It can be seen that the top angle is still overestimated significantly, while the relative angle is approximated much better than in the first model. However, in this model, the relative angle increases slower than can be seen in the measured signals. The signal of the calculated torque is still approximately twice as wide as the measured torque. It is assumed that the waves are still not realistic enough. In reality, the energy of each wave group will be spread out more than in this wave model. This is due to the unintentional inclusion of different wave components in the ramp-up and down of the regular waves.

Therefore, a more extensive calculation is performed. An in-house code called *Wavbas* is used, solving the potential equation on a staggered grid. Small deflections of the free surface and incompressibility are assumed, and the convective acceleration, viscous and body force terms are removed from the momentum equations. This results in a Poisson equation to be solved. The fact that small deformations of the free surface are assumed, makes it impossible to directly simulate a breaking wave. This approach is chosen, to reduce calculation time and complexity of the model. The used boundary conditions are listed below:

- The horizontal velocity at the top of the waveboard is derived from the input file sent to the flap-type wavemaker in the experiments. This velocity reduces linearly from maximum at the top of the waveboard to zero at the bottom of the tank. The pressure at the waveboard is the same as at the first grid point in the tank.
- The horizontal velocity at the end of the tank is equal to zero. Again, the pressure at the end of the tank is the same as at the first grid point in the tank.
- The vertical velocity at the bottom of the tank is equal to zero. And again, the pressure at the bottom of the tank is the same as at the first grid point in the tank.
- The pressure at the free surface is determined using the dynamic free surface boundary condition, describing that $p = p_{atm}$ at the instantaneous vertical position of the free surface.

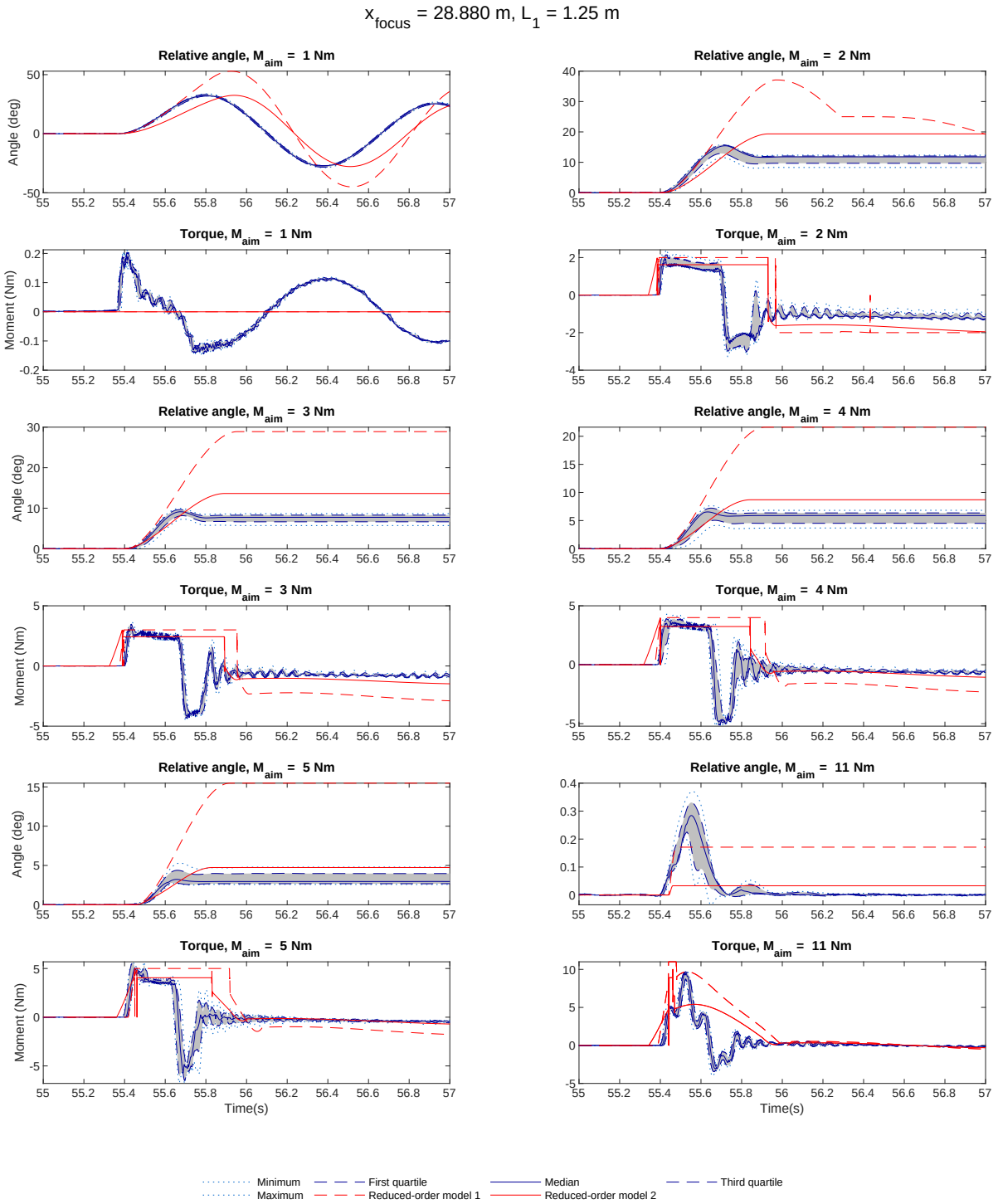

Figure 2.8: The relative angle between the top and bottom part and the measured and modelled frictional torque of the longest pendulum subjected to waves focused at x_{focus} = 28.880 m are shown. The time signals are given for six different aim values for the maximum frictional torque varying from 0 Nm to 11 Nm. The relative angle between the top and bottom pendulum shown here simulates the plastic response of a structure. The first reduced-order model overestimates the experimental values of the relative angle severely. The second model approximates the relative angle much better than in the first model. However, in this model, the relative angle increases slower than can be seen in the measured signals. The signal of the calculated torque is still approximately twice as wide as the measured torque.

Wavbas gives the input for the wave force in the form of the free surface, velocity and, via the derivative of the velocity, the acceleration as well. The results of the code are synchronised with the experimental values measured at wave gauge (WHM) 1 since the waves are not broken at that location. In order to

obtain optimal synchronisation all WHMs in the model are moved 0.85 m towards the wavemaker. At present, it is not understood why the shift is required.

After implementing these wave conditions into the reduced-order model, it is decided to change the formulation for the impact force slightly. The formulations for the Morison equation and the wetness parameter stay the same, which are given in equations 2.13 and 2.16. The formulation of the impact part of the force is changed. When implementing the formulation of Wienke et al. (2005), the wave force and acceleration of the pendulum start to oscillate at the moment of impact. This phenomenon is shown in figure 2.9 and the origin could not be explained. Another formulation for an impact force is taken from Goda et al. (1966):

$$F_{impact} = \begin{cases} \beta W \rho R v^2 \pi \left(1 - \frac{vt'}{R}\right) & \text{when positive} \\ 0 & \text{when negative} \end{cases} \quad \text{for} \quad 0 \leq t' \leq \frac{R}{v} \tag{2.19}$$

This impact formulation is applied at the moment that the wetness parameter is equal to 1 and the cylinder of the pendulum is fully submerged. t' starts counting from the moment that β = 1, W is equal to the width of the cylinder and R to the radius of the cylinder. The total horizontal load on the horizontal cylinder stays equal to $F_{wave} = \beta F_m + F_{impact}$.

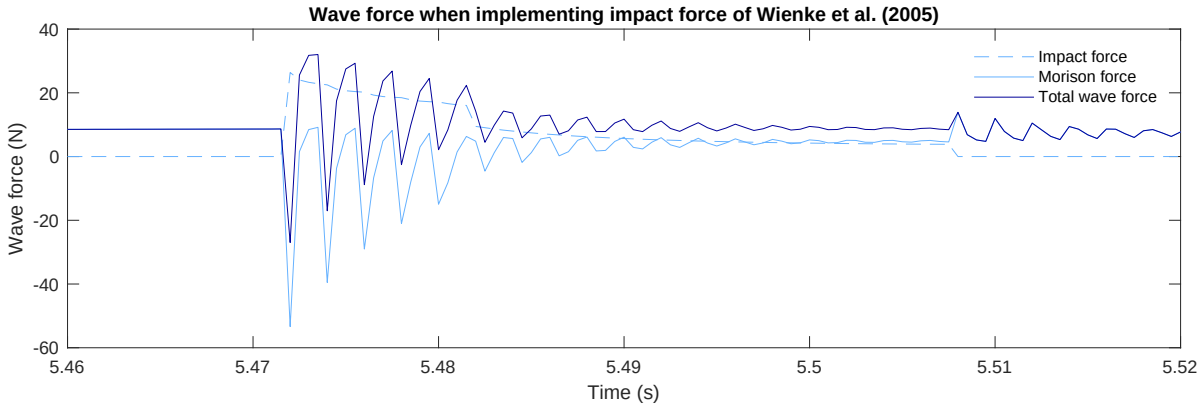

Figure 2.9: The force from the Morison equation, the impact force from Wienke et al. (2005) and their summation, which is the total wave force, are shown. The time shown on the x axis is only for scale. At the moment of impact the force increases instantly and afterwards an oscillating behaviour is observed. This phenomenon is found in the acceleration of the pendulum as well.

3

Experimental setup

Now that the existing and required research is established in chapter 1, and a reduced-order model of the double pendulum in breaking waves is presented in chapter 2, the experimental setup is explained in this chapter. The overall layout of the complete experiment is described first in section 3.1. As will be described in this section, the overall experiment consists roughly of two parts, namely the waves and the pendulum. These two parts are described separately in sections 3.2 and 3.3. Then, the inaccuracies known before the start of the experiments are shown in section 3.4.

3.1. The total layout of the experiment

The experiment consists roughly of two parts, namely the pendulum and its surrounding conditions. These two elements are combined in the total layout of the experiment shown in figure 3.1. In this figure, the beach is shown on the left and the waveboard of the wavemaker on the right. The middle position of the waveboard is defined as the origin of the axis system of the experiments. In this way, the waves will travel in the positive x-direction. In between the wavemaker and the beach, the pendulum is positioned at x = 29.88 m from the wavemaker. The three wave gauges (WHMs) are positioned at x_1 = 25.27 m, x_2 = 29.88 m and x_3 = 34.69 m from the wavemaker. The wave gauges in front and behind the pendulum are mainly used for checking the wave conditions with the expected values. Please note that this schematic overview is not to scale.

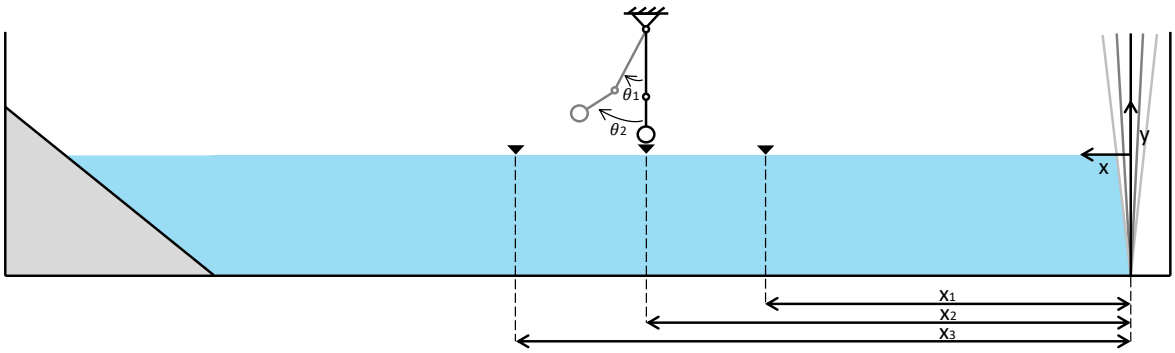

Figure 3.1: A schematic overview of the layout of the towing tank, which is not to scale. On the right side, the waveboard of the wavemaker is shown. The black line is the middle position from which the axis system is defined. This is not the same axis as earlier defined for the pendulum (shown in figure 2.5), but points in the same direction. Three wave gauges are positioned at x_1 = 25.27 m, x_2 = 29.88 m and x_3 = 34.69 m from the wavemaker. The second wave gauge is exactly positioned at the pendulum. On the left of the figure, the beach of the tank is shown.

3.2. Detailed information on the waves

The still water level (SWL) is at 994 mm from the bottom of the tank. The bottom of the tank and the walls are assumed to be perfectly flat. This assumption includes the assumption of no reflections due to the sides of the tank and no unexpected disturbances from the bottom. As stated in section 2.3.2, the wave signal consists of ten regular wave components. The amplitude, period and group velocity of these ten components are given in table 3.1.

Table 3.1: The amplitude, period and group velocity of the ten regular wave components that are used to create a focused wave.

Amplitude (m)	Period (s)	Group velocity (m/s)
0.0100	0.8003	0.6248
0.0110	0.8394	0.6554
0.0125	0.8948	0.6991
0.0145	0.9639	0.7545
0.0170	1.0441	0.8218
0.0200	1.1340	0.9032
0.0240	1.2467	1.0176
0.0290	1.3814	1.1716
0.0360	1.5667	1.3976
0.0500	1.9437	1.8187

Each regular wave group is 3.5 waves long and is either increased to the amplitude or decreased to zero over one period. At the focus point, all the wave components are exactly at the 1.75th wave and are, therefore, in phase. To know how the wave travels towards this focus point, the following two characteristics of the waves need to be incorporated: Every wave group travels with their own group velocity, and in each group, the wave propagates according to $A_i \cos(k_i x - \omega_i t)$ with x relative to the focus point.

In this experiment, three different focus points will be used, located at x_{focus} = 28.380 m, x_{focus} = 28.880 m and x_{focus} = 29.380 m from the wavemaker. Relative to the pendulum, the focus locations are at -1.5 m, -1.0 m and -0.5 m, respectively. The steepness of the focused wave is higher than the limit and, therefore, it will break.

The performance of the flap-type wavemaker of the TU Delft can be tuned with different parameters. The first parameter is the angle of the cylinders connected to the waveboard. The angle of these cylinders in this experiment is 20.01 deg, which causes a motion that is partially rotational and partially translational. In order to minimise losses in the cables from the carriage to the wavemaker, the output generated at the carriage should be maximal. Therefore, the attenuation factor at the wavemaker is set to 2.6, which results in an output of the wavemaker that is 26 % of the input.

After using this theory and the details of the wavemaker to create an input file for the wavemaker, the waves can be measured. In figure 3.2, the measured waves at WHM 1 and at the begin location of the pendulum are shown (which is equal to WHM 2). As can be seen, not all waves are entirely the same. More variations in the signal occur when the wave breaks further away from the pendulum (shown in the top right diagram). When this phenomenon would have been observed when no pendulum is present, it could have lead to the conclusion that the longer after breaking, the more spread can be observed. However, the variability can also be ascribed to fluid-structure interaction (FSI). A detailed analysis of this will be done in chapter 4. To see the pure repeatability of the waves, every morning the same wave is generated, without the pendulum interacting with it. The results of this wave are shown in the bottom two diagrams of figure 3.2. Some variability can be seen, but it is much less than observed in all the situation together. Variation also occurs due to inaccuracies of the wave gauges. This inaccuracy and other inaccuracies that are known before the actual experiment is started are discussed in section 3.4.

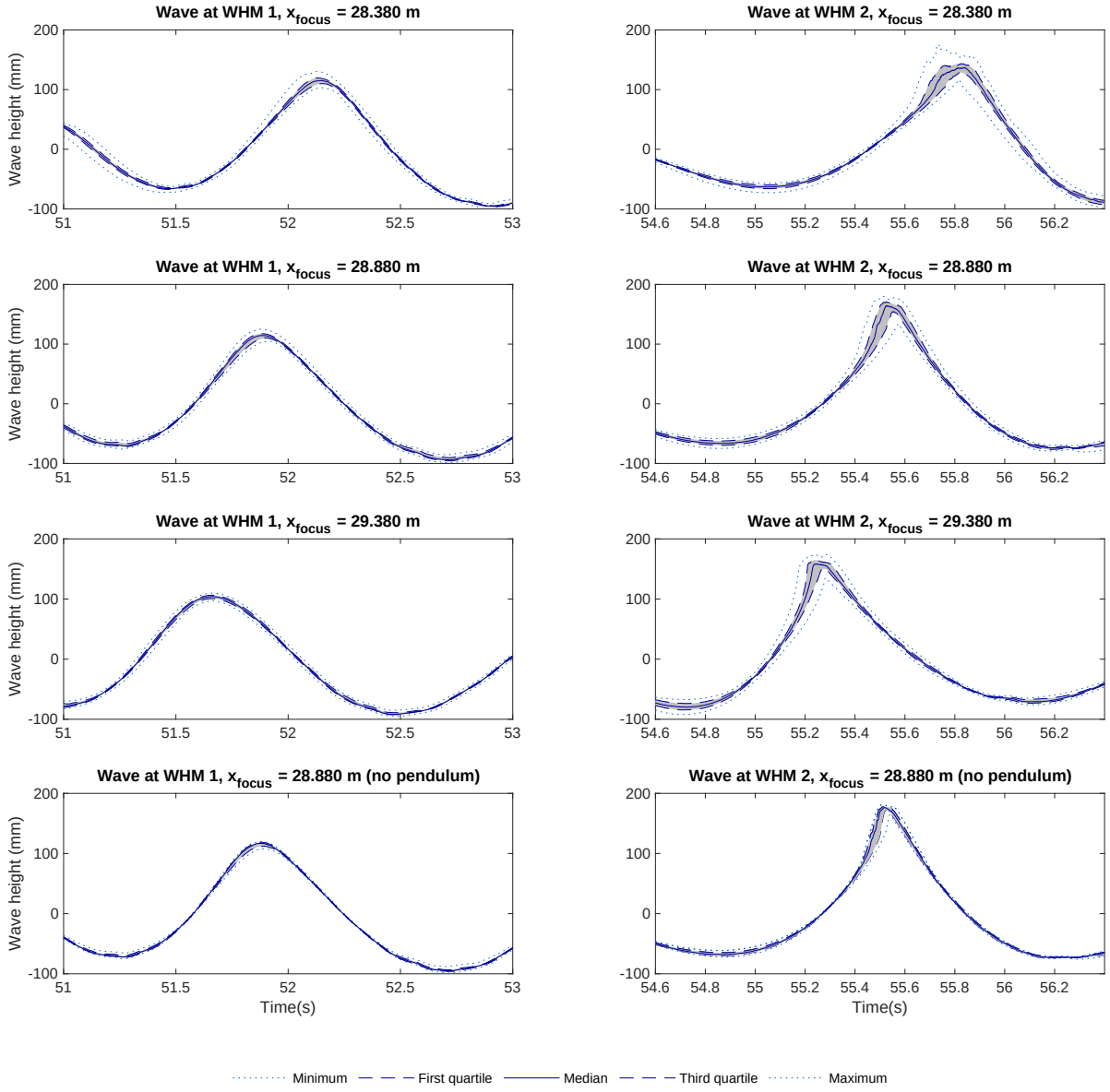

Figure 3.2: Wave measurements at WHM 1 at x = 25.27 m and WHM 2 at x = 29.88 m for the three different focus locations: x_{focus} = 28.380 m, x_{focus} = 28.880 m and x_{focus} = 29.380 m from the wavemaker. The minimum, maximum, median, lower limit of the first quartile and upper limit of the third quartile are shown, based on 109, 109 and 120 repetitions for the three focus locations. More variations in the signal at the pendulum occur when the wave breaks further away from the pendulum (shown in the top right diagram). Another reason for the spread can be FSI. In the bottom two graphs, the results of 13 repetitions for a wave focused at x_{focus} = 28.880 m without impacting on the cylinder are shown. Compared to the large variability shown in the top six diagrams, these two bottom diagrams show less spread due to fewer repetitions, but also lack of influence of the pendulum.

3.3. Detailed information on the pendulum

Now that the overall position of the pendulum is shown to be at x = 29.88 m from the wavemaker, the details of the pendulum are given. The design of the pendulum is realised using the reduced-order model described in section 2.3. It is assumed that this model is sufficiently accurate to obtain useful parameters of the pendulum. After the ideal design is explained in section 3.3.1, the real geometry of the pendulum is shown in section 3.3.2. This section contains the overall layout of the pendulum and important dimensions. Then, a more detailed overview of the friction mechanism is given in section 3.3.3.

3.3.1. Design of pendulum

The first reduced-order model of the double pendulum can be used to design the experiment. In this pendulum the top hinge is a regular hinge and in the bottom hinge friction can be applied. Note that the results presented in this section are obtained by using a simplified model. A considerable limitation of the current model is the wave model used to determine the wave force. Next to this, only one value of the frictional moment is incorporated, while in reality, this moment is dependent on different factors. For example, the static and dynamic friction coefficients are not equal.

First, the required output and possible variations of the reduced-order model will be determined. Then, the results of the variations chosen in this section will be evaluated. Furthermore, the final dimensions of the design are given.

The output of the reduced-order model that influences the design choices

In order to determine a good design for the experiment, a definition of a 'good design' should be stated. This definition will be based on the required output of the model and the experiment to be able to answer the main research question. The desired output of this research shows the absorbed energy in the plastic deformation, which is already stated in section 1.3. This absorbed energy should be maximised in order to see the largest influence of the plasticity on the behaviour of the pendulum. The absorbed energy in the plastic deformation can be given as the dissipated energy due to frictional work and can be calculated using equation 3.1.

$$W_f = \int M_f d\theta \tag{3.1}$$

For a constant moment and an angle that only increases, this equation is equal to multiplying the frictional torque and the final angle between the top and bottom pendulum.

To maximise the dissipated energy, different parameters of the pendulum can be adjusted. These adjustments should be made in such a way that after the impact, the dissipated energy is maximal, and the influence of the motion of the pendulum is minimal. The initial values of the design are based on the pendulum used in previous experiments by Bos and Wellens (2020). For every new design, one parameter of this initial design is adjusted. The parameters that are subjected to change are the length, mass and location of the centre of gravity of both the top and bottom pendulum. Changing these parameters results in a range of values of the frictional torque for which energy will be dissipated. A broad range of these values is judged as a positive element of that specific design.

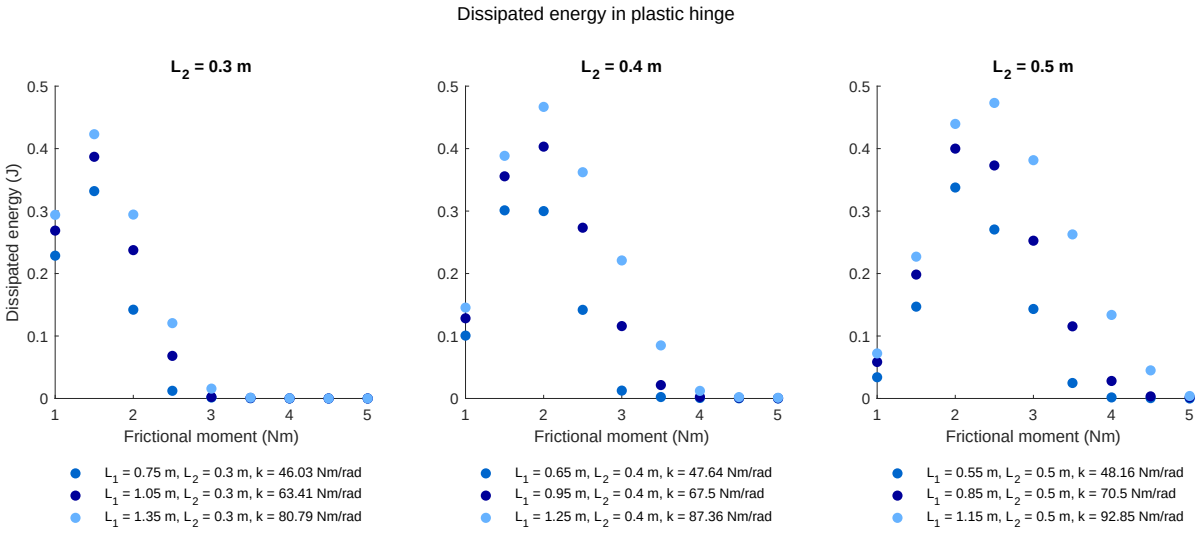

Figure 3.3: The length of the bottom pendulum is varied between 0.3 (left), 0.4 (middle) and 0.5 m (right). The dissipated energy and the range of frictional moment increase with a longer bottom part of the pendulum. For a longer bottom pendulum, more influence of the motion of the pendulum can be seen when a low frictional torque is applied.

Changes to the length, centre of gravity, and mass: L_2 = 0.4 m, $h_1 > h_2$ and $m_1 \gg m_2$
As shown in section 1.3, it is desired that the absorbed energy in the plastic deformation with respect to the stiffness of the pendulum is found. Therefore, three values for the total length of the pendulum are chosen: 1.05, 1.35 and 1.65 m. For every adjustment, the results are given for these three total lengths of the pendulum.

The first adjustment is the change of lengths of both parts of the pendulum, shown in figure 3.3. Since the total length is fixed, as stated in the previous paragraph, only the length of the bottom pendulum is adjusted. When the length of the bottom pendulum is changed between 0.3, 0.4 and 0.5 m, it can be seen that the dissipated energy and the range of frictional moment increase with a longer bottom part of the pendulum. However, for a longer bottom pendulum, more influence of the motion of the pendulum can be seen when a low frictional torque is applied. Therefore, a bottom length of 0.4 m is chosen to use as a fixed value for the other variations.

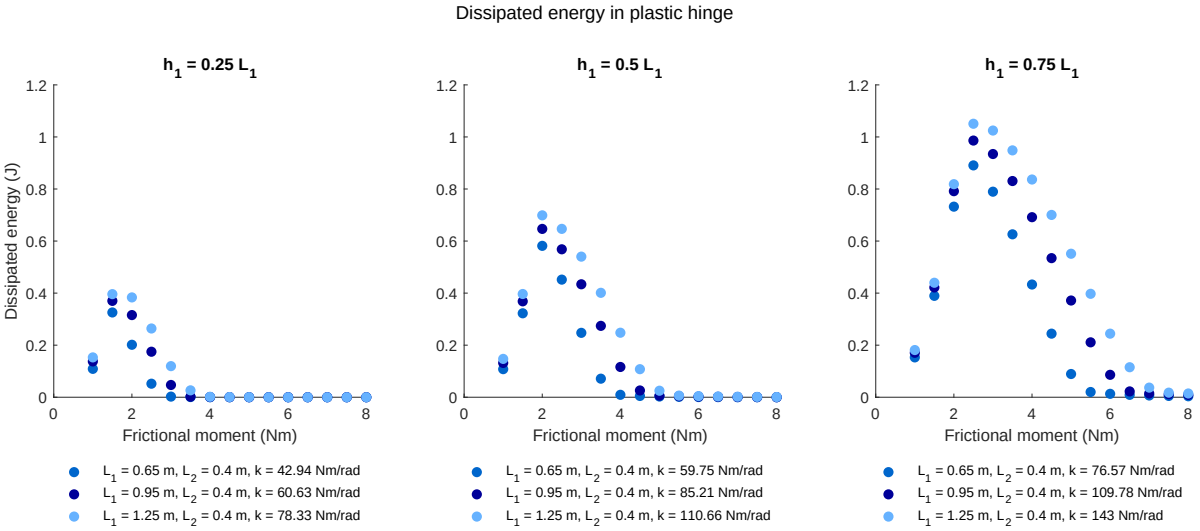

Figure 3.4: The centre of gravity of the top pendulum is varied between 0.25 L_1 (left), 0.5 L_1 (middle) and 0.75 L_1 (right). The dissipated energy and the range of frictional moment increase with a lower centre of gravity of the top part of the pendulum.

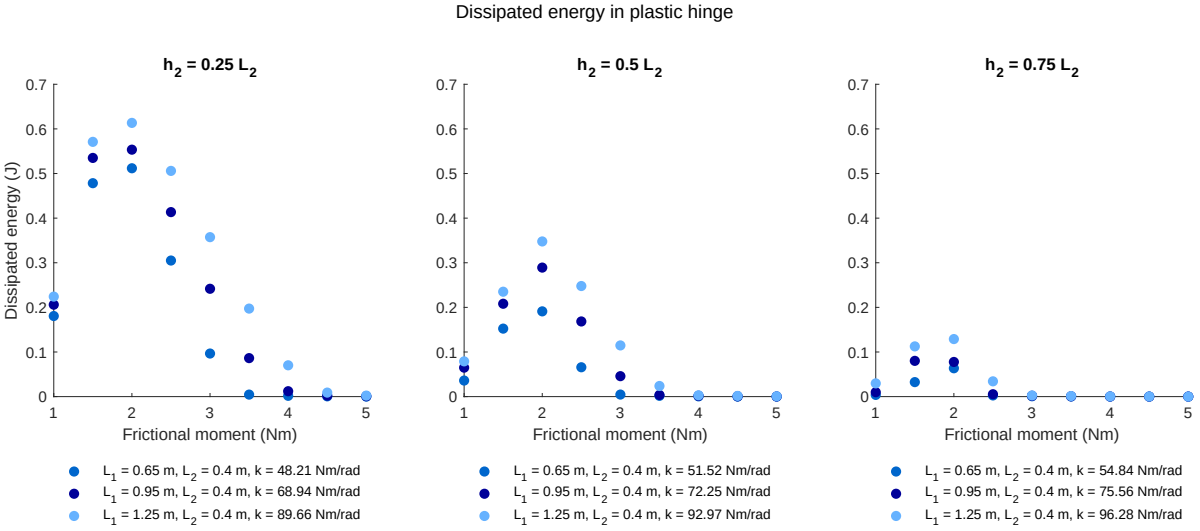

Figure 3.5: The centre of gravity of the bottom pendulum is varied between 0.25 L_2 (left), 0.5 L_2 (middle) and 0.75 L_2 (right). The dissipated energy and the range of frictional moment decrease with a lower centre of gravity of the bottom part of the pendulum.

The second adjustment is the change of centre of gravity of both parts of the pendulum, shown in figures 3.4 and 3.5. A big difference in behaviour can be seen between changing the centre of gravity of the top part and the bottom part in figure 3.4 and 3.5, respectively. From only adjusting the centre of gravity, it can be concluded that the lower the centre of gravity of the top part of the pendulum is, the higher the dissipated energy is. On the other hand, a lower centre of gravity of the bottom pendulum decreases the dissipated energy significantly. By lowering the centre of gravity of the bottom pendulum, the arm that creates a moment due to wave force reduces and the arm towards the friction hinge increases, explaining this phenomenon. Therefore, a combination of a high centre of gravity of the bottom pendulum and a low centre of gravity of the top pendulum results in the highest dissipated energy.

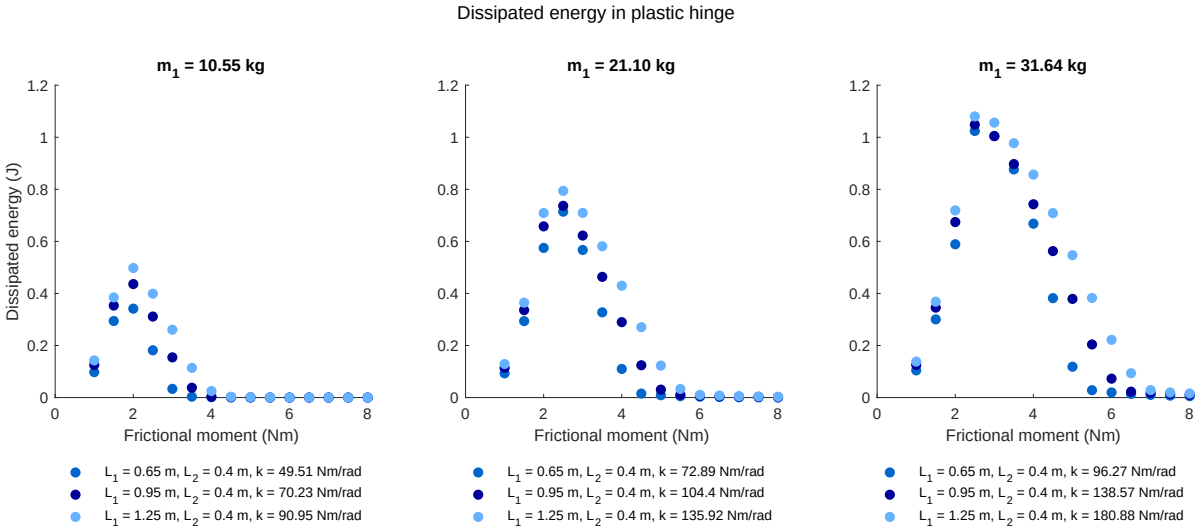

Figure 3.6: The mass of the top pendulum is varied between 10.55 (left), 21.10 (middle) and 31.64 kg (right). The dissipated energy and the range of frictional moment increase with a heavier top part of the pendulum.

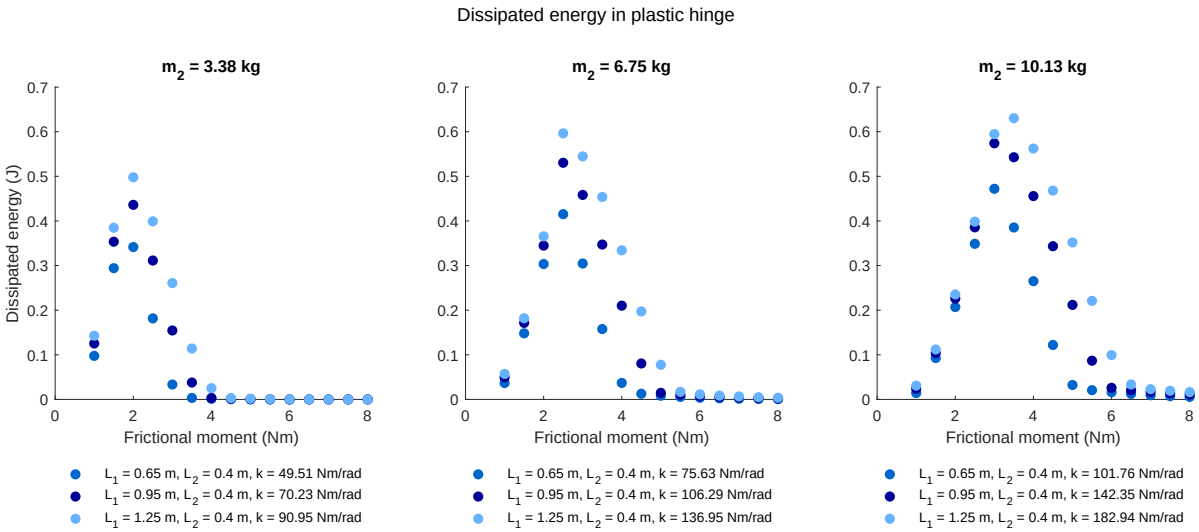

Figure 3.7: The mass of the bottom pendulum is varied between 3.38 (left), 6.75 (middle) and 10.13 kg (right). The dissipated energy and the range of frictional moment increase with a heavier bottom part of the pendulum.

The third adjustment is the change of mass of both parts of the pendulum, shown in figures 3.6 and 3.7. Increasing the mass of each of the parts of the pendulum causes an increase in the dissipated energy. The increase in dissipated energy when adjusting the mass of the top part, see figure 3.6, is higher than the increase in dissipated energy when adjusting the mass of the bottom part, see figure 3.7. This observation leads to the choice to increase only the mass of the top pendulum, to keep the

large difference in mass between the top and bottom that shows promising results in the right diagram of figure 3.6. The total mass of the pendulum should be limited. Otherwise, the risk of little total energy transfer from the wave to the pendulum occurs.

Final dimensions of the pendulum aimed for in the experiment

A choice is made for the final design dimensions that will be aimed for during the fabrication of the pendulum for the experiment, based on the analysis in the previous section. These dimensions are summarised in table 3.2 in which three different arrangements are shown. These three arrangements correspond to the three different values for the total length of the pendulum. The resulting dissipated energy is shown in figure 3.8. In this figure, it can be seen that the range of frictional torques that shows a significant amount of dissipated energy and no influence of the motion of the pendulum is between 4 and 12 Nm. It can be seen that for lower frictional torques (4 - 6 Nm), the smallest pendulum results in more dissipated energy, while for higher frictional torques, the longest pendulum results in more dissipated energy.

Table 3.2: For all three situations the desired dimensions and other numeric characteristics of the pendulum are shown. Centre of gravity is with respect to the fulcrum of each part of the pendulum. All elements indicated with a subscript 1 correspond to the top part of the pendulum and the elements with a 2 correspond to the bottom part of the pendulum.

	Long L_1 = 1.25 m	Medium L_1 = 0.95 m	Short L_1 = 0.65 m	
Length 1	1.25	0.95	0.65	m
Mass 1	31.5	31.5	31.5	kg
Centre of gravity 1	0.75 L_1 = 0.9375	0.75 L_1 = 0.7125	0.75 L_1 = 0.4875	m
Length 2	0.4	0.4	0.4	m
Mass 2	3.5	3.5	3.5	kg
Centre of gravity 2	0.25 L_2 = 0.1	0.25 L_2 = 0.1	0.25 L_2 = 0.1	m

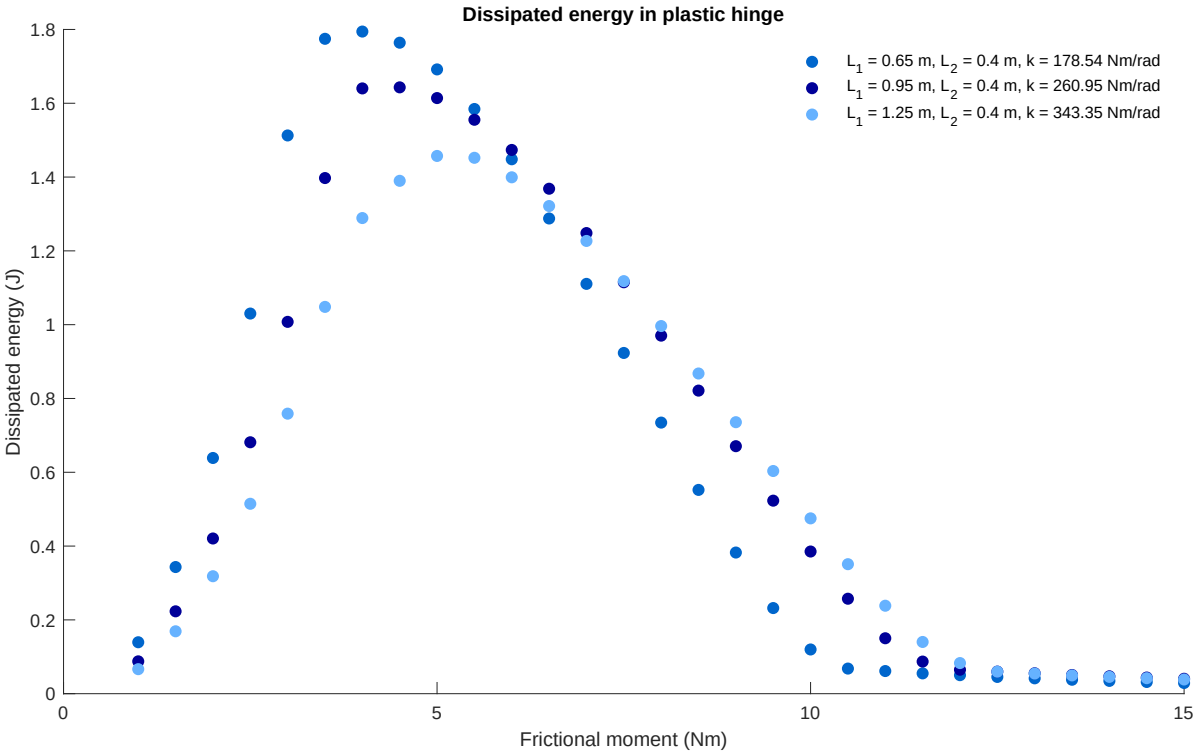

Figure 3.8: Dissipated energy for the final values that will be aimed for in the experiment. The range of frictional torques that shows a significant amount of absorbed energy and no influence of the motion of the pendulum is between 4 and 12 Nm.

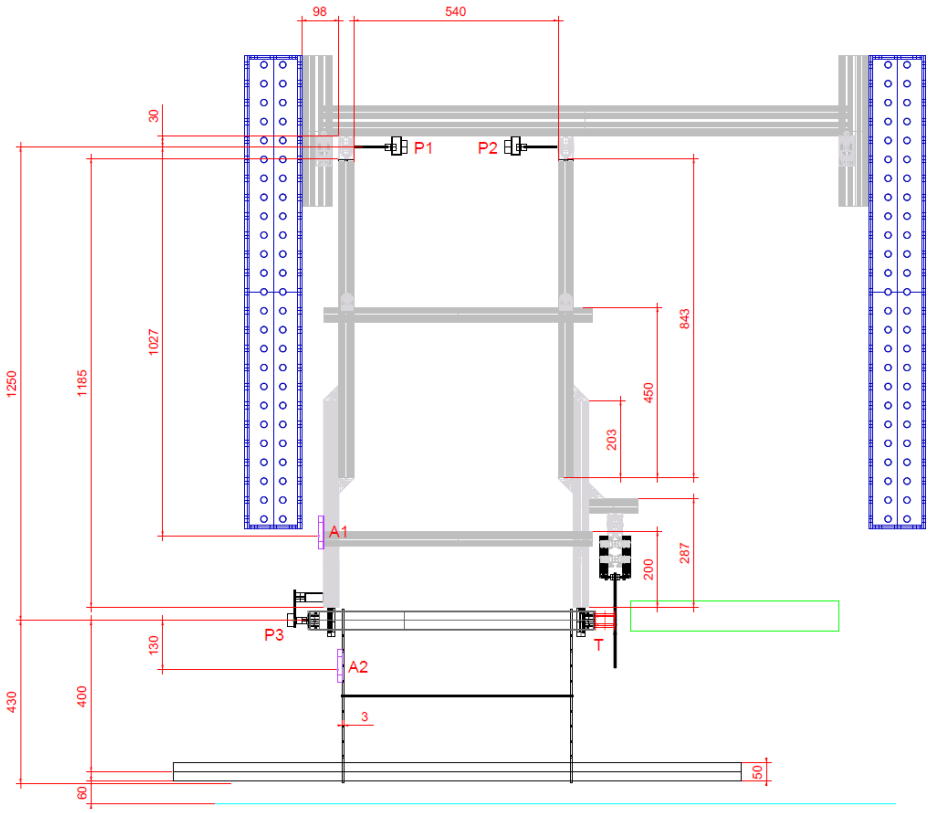

Figure 3.9: Schematic overview of the longest pendulum. In this arrangement, the length of the top part of the pendulum is 1.25 m, and the length of the bottom part is 0.4 m. The potentiometers are indicated with P1, P2 and P3, the accelerometers with A1 and A2 and the torque sensor with a red T. The distance between the blue beam and the pendulum is chosen in such a way that the cylinder of the pendulum is positioned in the middle of the towing tank. *Drawing by Jasper den Ouden.*

3.3.2. The geometry of pendulum: three different arrangements

The pendulum is constructed using the desired parameters of the pendulum given in section 3.3.1. It consists of a PVC cylinder with a diameter of 50 mm and a width of 1.5 m. This cylinder is connected to the bottom hinge with thin strips made of stainless steel. These strips are assumed to receive no contribution from the hydrodynamic force since they are thin compared to the width of the cylinder. The mechanism to apply and measure friction is connected to the bottom hinge and can measure frictional moments between 0 and 22 Nm. The amount of friction can be adjusted by compressing or releasing a compression spring in combination with brake-blocks on a brake disc. The rest of the pendulum is made of aluminium profiles. The top of the pendulum is connected to an adjustable frame. The adjustable frame facilitates keeping the cylinder at the same height while adjusting the length of the pendulum.

In this section, only the longest of the three different arrangements of the pendulum is shown in figure 3.9. This figure shows this arrangement seen in the travel direction of the waves. The potentiometers are indicated in the figure with P1, P2 and P3, the accelerometers with A1 and A2 and the torque sensor is indicated with a red T. Important dimensions are also shown in this figure. The dimensions and elements of all three arrangements can be found in appendix A. The specific values for the properties of each arrangement are given in table 3.3.

All distances are measured with a measuring tape, and the weights are determined using a scale. The centre of gravity is determined by balancing the parts of the pendulum on a thin vertical plate until stable. The restoring force coefficient is equal to the product of the mass, the centre of gravity and the gravitational acceleration, shown in equation 3.2.

$$k = mgh \tag{3.2}$$

The inertia coefficient is determined in a free vibration test. The period of oscillation is measured with

Table 3.3: For all three situations the dimensions and other numeric characteristics of the pendulum and the pendulum with respect to the water are given. The centre of gravity is with respect to the fulcrum of each part of the pendulum. The inertia coefficient is given with respect to the centre of gravity. All elements indicated with a subscript 1 correspond to the top part of the pendulum and the elements with a 2 correspond to the bottom part of the pendulum.

	Long L_1 = 1.25 m	Medium L_1 = 0.95 m	Short L_1 = 0.65 m	
Length 1	1.25	0.95	0.65	m
Mass 1	24.92	24.92	22.40	kg
Centre of gravity 1	0.755	0.592	0.348	m
Inertia coefficient 1	3.07	1.84	0.84	kgm^2rad^{-1}
Damping coefficient 1	0.376	0.339	2.590 [1]	$Nmsrad^{-1}$
Restoring force coefficient 1	184.57	144.72	76.47	$Nmrad^{-1}$
Length 2	0.4	0.4	0.4	m
Mass 2	5.26	5.26	5.26	kg
Centre of gravity 2	0.107	0.107	0.107	m
Inertia coefficient 2	0.14	0.14	0.14	kgm^2rad^{-1}
Damping coefficient 2	0.036	0.036	0.036	$Nmsrad^{-1}$
Restoring force coefficient 2	5.52	5.52	5.52	$Nmrad^{-1}$
Diameter cylinder	50	50	50	mm
Distance SWL and bottom cylinder	60	60	60	mm

[1] The original value for the damping coefficient of the shortest pendulum determined in the workshop is 0.169 $Nmsrad^{-1}$. However, when analysing the results, the damping behaviour of the model is much slower than the behaviour observed in the experiment. Transporting and reconnecting the pendulum to the hinges in the tank could have changed the damping, which would clarify the large difference in behaviour. Therefore, a new damping coefficient is determined from the results measured in the tank. This phenomenon underlines the importance of a correct assembly of the experimental setup.

a stopwatch, and the moment of inertia can be determined according to equation 3.3. In this equation $I_{fulcrum}$ is the moment of inertia around the fulcrum of the pendulum, while I_{CoG} is the moment of inertia around the centre of gravity of the pendulum. In the reduced-order model I_{CoG} is used.

$$\begin{aligned} I_{fulcrum} &= \left(\frac{T}{2\pi}\right)^2 mgh \\ I_{CoG} &= I_{fulcrum} - mh^2 \end{aligned} \tag{3.3}$$

After determining the inertia and restoring force coefficient, the measured angle in the free vibration test and its first and second derivative, a least squares fit can be applied on equation 3.4 to determine the damping coefficient of both parts of the pendulum.

$$I_{fulcrum}\ddot{\theta} + c\dot{\theta} + ksin(\theta) = 0 \tag{3.4}$$

The angles of a free oscillation of the long pendulum are shown in figure 3.10. In this free oscillation the reduced-order model is compared to the experiment, and both the model itself as well as the properties of the model can be evaluated. The behaviour of the oscillation of both parts of the pendulum is simulated accurately, which likely means that the model itself is quite accurate. The magnitude of the signal of the relative angle, however, is overestimated at some moments. This could be an indication that the separate damping coefficients of the pendulum parts are not a good representation of the total damping of the double pendulum. The differences at the start of the signal could also originate from the fact that the pendulum does not start at zero velocity in the experiment. The conclusions of this research will not be influenced by the differences between the model and the experiment shown in figure 3.10.

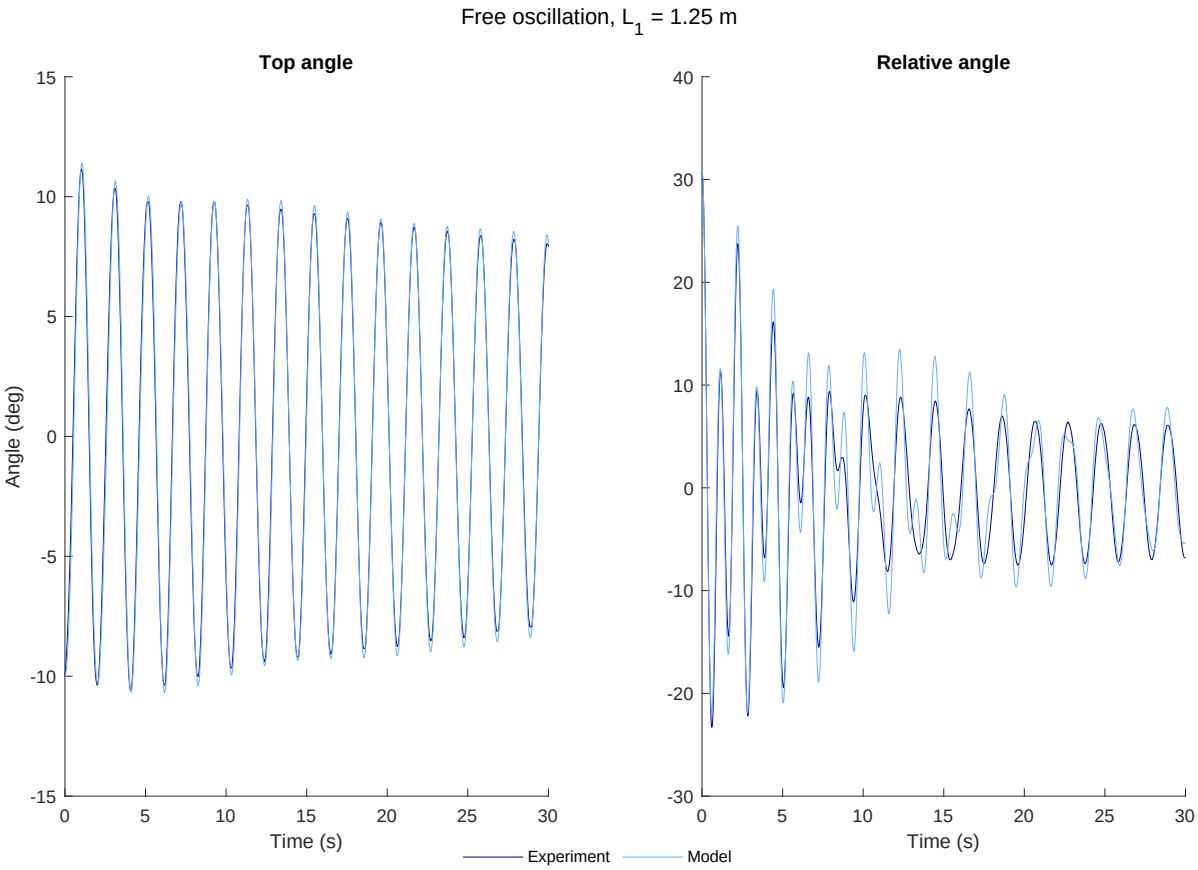

Figure 3.10: This figure shows the angles of a free oscillation of the long pendulum. In this free oscillation, the reduced-order model is compared to the experiment, and both the model itself as well as the properties of the model can be evaluated. The behaviour of the oscillation of both parts of the pendulum is simulated accurately, but the magnitude of the signal of the relative angle is overestimated at some moments.

3.3.3. Friction mechanism: repeatability and adjustability

Two aspects of the friction mechanism are critical to investigate beforehand: the resulting frictional torque of adjustments of the spring and the repeatability of these frictional torques.

First, two different positions of the spring are examined several times. In this examination, the top part of the pendulum is fixated, and a horizontal pressure on the cylinder is slowly increased by hand. This check is used to examine the repeatability of the frictional torque due to a certain position of the spring. Next to this, a reasonable first impression is obtained of the behaviour of the frictional torque. For each position of the spring, a single test is performed with a faster increase of the pressure to analyse the behaviour of the torque in that situation. The results of these tests are shown in figure 3.11. The measured results are filtered using a moving average filter. In this figure, it can be seen that for the tests in which the pressure is increased slowly, the torque increases until it suddenly drops and stays at a constant value. This phenomenon is the difference between the static and the dynamic frictional moment since the drop is at the moment the bottom pendulum starts to move. All the runs give approximately the same values and behaviour. The only run that is significantly different is the one in which the pressure is increased fast. The static friction is higher than, and the dynamic friction is not as constant as is observed in the other runs.

Now that the repeatability of the frictional torque is checked, a complete overview of the torque corresponding to a position of the spring should be established. This relation can be indicated as the adjustability of the spring. Based on figure 3.11, the average of the value for the dynamic frictional torque is used for this. The distance x_{nut}, indicated in figure 3.12, is adjusted, and the average torque is measured. These measurements are shown in figure 3.13. As expected, this figure shows a linear relation. The spring is linearly compressed, resulting in a linear increase of the normal force on the

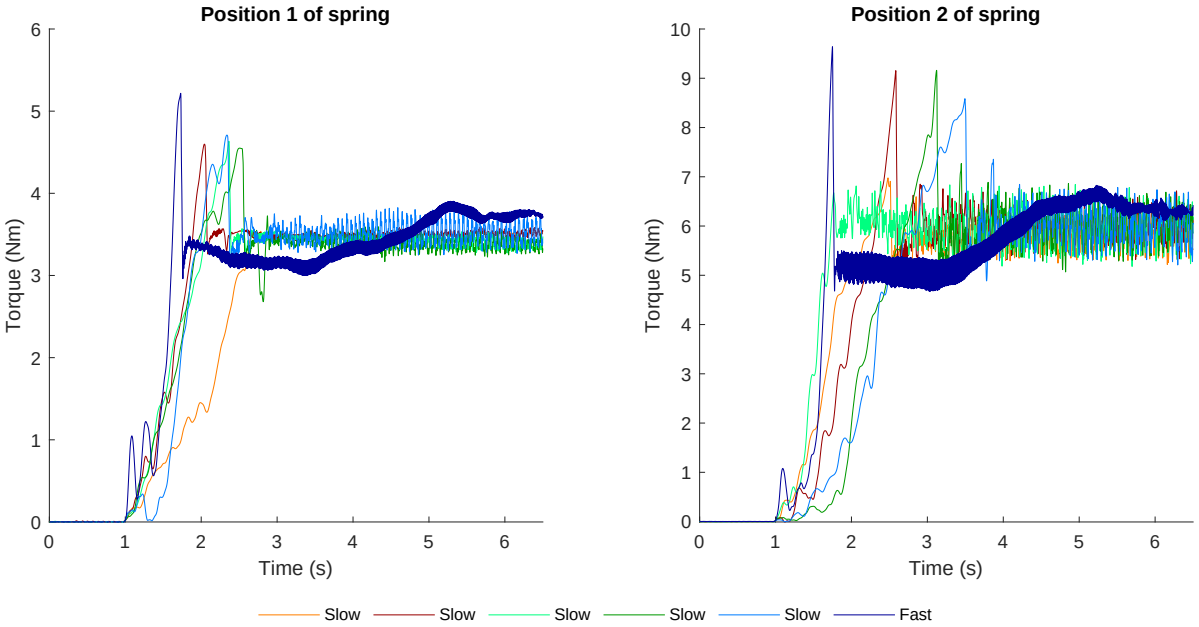

Figure 3.11: Measured torque as a result of a fixated top part of the pendulum and increasing horizontal pressure on the cylinder. Five times the pressure is slowly increased and one time faster. The measured results are filtered using a moving average filter. It can be seen that for the tests in which the pressure is increased slowly, the torque increases until it suddenly drops and stays at a constant value. This phenomenon is the difference between the static and the dynamic frictional moment since the drop is at the moment the bottom pendulum starts to move. All the runs give approximately the same values and behaviour. When the pressure is increased fast, the static friction is higher, and the dynamic friction is not as constant as is observed in the other runs.

disc. This creates a linear relation between the compression of the spring and the frictional torque. The equation for this linear relation is given in equation 3.5. For this formulation, the first and last measurements are not taken into account. They deviate from the relation probably due to deformations of the connection for the spring to the brake-blocks (for high torque) or a measurement of the normal clamping force that is not precise enough (for low torque).

$$x_{nut} = 2.1252 T_{desired} + 26.7652 \tag{3.5}$$

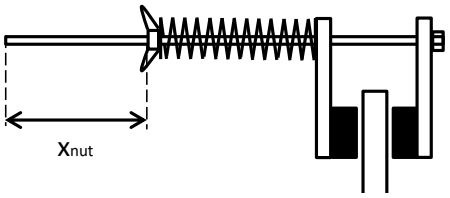

Figure 3.12: A schematic overview of the brake disc, brake-blocks, spring, nut and distance x_{nut}. This distance x_{nut} is used to tune the amount of compression of the spring.

The values used to determine the relation shown in equation 3.5 are only measured once. The measurements shown in figure 3.11, which are measured on a later time, are also shown in figure 3.13. As can be seen, the values for position 1 are not on the linear line. This can indicate that the linear relation is not the same over time, or that the linear relation is not completely correct. In either of these cases, the same value for x_{nut} is used over the experiment. Therefore, the deviation for the linear line is accepted.

The values for each desired torque are summarised in table 3.4. In order to decrease the measurement errors possible in adjusting the spring, the orientation of the nut is restricted to a horizontal one. This restriction is the reason why the third column of table 3.4 is added. This constraint creates the disadvantage of not meeting the desired torque exactly. However, it is found to be acceptable and the values in the third column of table 3.4 are used during the experiment.

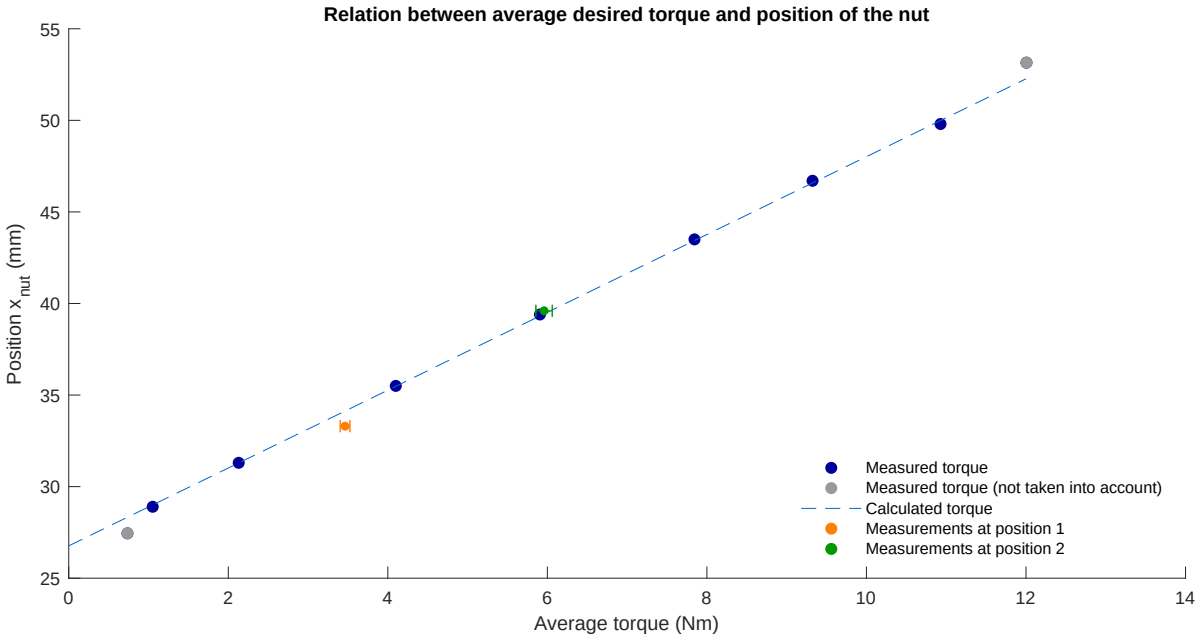

Figure 3.13: The relation between the desired torque and the required position of the spring shows a linear relation. The spring is linearly compressed, resulting in a linear increase of the normal force on the disc. This creates a linear relation between the compression of the spring and the frictional torque. The equation for this linear relation is equal to x_{nut} = 2.1252 $T_{desired}$ + 26.7652. The first and last measurements are not taken into account. Next to the measurements used to calculate the linear relation, the measurements from figure 3.11 are shown as well including the standard deviation. The measurements at position 1 are not on the linear line. This can indicate that the linear relation is not the same over time, or that the linear relation is not completely correct.

Table 3.4: A summary of the required position of the nut for the desired torque. The third column shows the required position of the nut incorporating the restriction of only using a horizontal position of the nut. This restriction is included to minimise measurement errors, and, therefore, this column shows the values used in the experiment.

Torque (Nm)	$x_{nut,aim}$ (mm)	$x_{nut,horizontal}$ (mm)
1	28.89	29.1
2	31.02	31.2
3	33.14	33.3
4	35.27	35.4
5	37.39	37.5
6	39.52	39.6
7	41.64	41.7
8	43.77	43.8
9	45.89	45.9
10	48.02	48.0
11	50.14	50.1

3.4. Sensor calibration

Before the actual measurements start, all the sensors are checked and calibrated in order to know the inaccuracies that result from each of them. The first sensors that are already mentioned are the wave gauges or wave height measurement devices. The position of each of them is shown in figure 3.1. On the pendulum, three potentiometers are installed to measure the angle of the top hinge on both sides and the bottom hinge on one side of the pendulum. The accelerometers are installed on the vertical parts of both the top and bottom pendulum, one for each part. The last sensor is the torque meter, which is located on the axis of the bottom hinge and measures the applied frictional torque on this hinge. All these sensors on the pendulum are shown in figure 3.9. All signals are acquired using a sampling frequency of 1000 Hz. After that, all signals are filtered with an analogue filter of 100 Hz.

In the next step, filtering occurs using a digital moving average filter using a window width of 25 data samples. A moving average filter is appropriate for reducing noise but keeping peaks (Smith, 1999).

All sensors are calibrated and checked differently. The WHMs are calibrated by measuring the output at every 20 mm of the range. A straight line is fitted through this data; and the measurement error causes deviations. The potentiometers and torque sensor are calibrated similarly, but then using steps of respectively 5 deg and 2 kg at a distance of 0.09 m. The accelerometers are calibrated by letting only gravity act on both sides of the sensor. The absolute maximum measurement errors of all these calibrations are given in table 3.5. The maximum occurring measurement errors of the accelerometers are not given, since the calibration factor is not based on small steps as for the other sensors.

Two other factors that are known beforehand influence the variations and errors in the results. The first factor is the error due to measuring lengths. The exact error can not be quantified easily, but due to small dimensions of the pendulum, it is assumed to be less than 1 mm. The spirit level that is also used to adjust the geometry has an accuracy of 1 mm/m. The second factor is the variability in the waves and the wavemaker. This factor is difficult to measure separate from the measurement error due to the wave gauges. Therefore, the variability in the waves will be presented in all the following figures. The variability will also be shown for the results that are influenced by this.

Table 3.5: A summary of the absolute maximum measurement errors of all sensors used in the experiment. The measurement errors of accelerations, length measurements and the waves are not included in this table due to the difficulty in quantifying these errors.

Name	Position	Measurement error	
WHM 1	In front of pendulum (x_1 = 25.27 m)	0.85	mm
WHM 2	At pendulum (x_2 = 29.88 m)	1.3	mm
WHM 3	Behind pendulum (x_3 = 34.69 m)	0.99	mm
Potmeter 1	Axis of top hinge	0.24	deg
Potmeter 2	Axis of top hinge	0.15	deg
Potmeter 3	Axis of bottom hinge	0.21	deg
Torque meter	Axis of bottom hinge	0.176 / 0.035 [1]	Nm

[1] The first value is the maximum error observed when an almost ideal moment is applied to the torque sensor. However, in the test setup, only one side of the torque sensor is loaded, which also causes a shear force. Fortunately, the error is smaller in that situation. The larger error in the first case is probably caused by hysteresis that is observed in the signal

4

Results and discussion

After presenting the research questions in chapter 1, designing the experimental setup in chapter 3 based on the reduced-order model introduced in chapter 2, the results of the experiments and the model are presented and discussed in this chapter. The model used for the results presented here is the model shown in section 2.4. Not all results are presented here; the visualisation of selected situations are shown. These situations contain notable behaviour of the pendulum or are the example situation, which is chosen to be the longest pendulum and the wave focused at x_{focus} = 28.880 m (the middle focus location). The values of the frictional torque applied to the bottom hinge vary between 0 and 11 Nm, in which the last value creates a pendulum that stays fixed, creating a single hinge pendulum.

First, the results in the time domain of the pendulum with L_1 = 1.25 m subjected to the wave focused at x_{focus} = 28.880 m are presented and discussed in section 4.1. The time signals are shown to create an understanding of how the pendulum behaves and how well the reduced-order model can predict this behaviour. The differences in magnitude are discussed in the section that follows, section 4.2. In that section, different energy components of the pendulum are analysed. Energy components that are related to elastic as well as plastic behaviour are shown. This section can give the final insight to answer the main question. A detailed overview of all the results is shown in appendix B.

4.1. Measured time signals to analyse pendulum behaviour

The first part of the results consists of the results over time for the longest pendulum in waves with x_{focus} = 28.880 m of five different sensors. These sensors are potentiometers 1 and 2 which measure the angle of the top part of the pendulum, potentiometer 3 which measures the relative angle of the top and bottom part, the torque meter which measures the torque that acts on the bottom hinge and WHM 2 which measures the wave height at the original position of the pendulum. The signals of these sensors are filtered once with a moving average filter with a width of 25 data points. The results of the last three sensors are directly shown in this section. The results of potentiometers 1 and 2 are averaged to show the behaviour of the top pendulum in a more compact way. A more detailed analysis of this simplification is shown in appendix C.

When looking closely at the signals for the angle of the top and bottom part of the pendulum, horizontal parts can be observed in the signal. These horizontal parts of the signal are created by the minimum resolution steps of the potentiometers. The potentiometers stay at a particular value before 'jumping' to the next. This behaviour is inevitable for these potentiometers with the specific range used here. The steps vary between 0.1 and 0.38 deg. This value should be added to the inaccuracy of all potentiometers. This behaviour leads to problems when calculating the derivatives of the angles, which results in difficulties when calculating some energy components of the pendulum. This problem is solved by selecting the horizontal or nearly horizontal parts of the signal. Then, the middle points of these intervals and the middle points of the other intervals are selected. A cubic spline is fitted through these points. A more detailed analysis of this fit function is shown in appendix C.

Each experimental condition, which is a combination of a pendulum arrangement and a wave focus location, is tested five or six times. From these five or six repetitions, the median, 25% and 75%

quartiles, and the minimum and maximum measured values can be determined. These are shown in every figure in this section. The reduced-order model is shown with a black line.

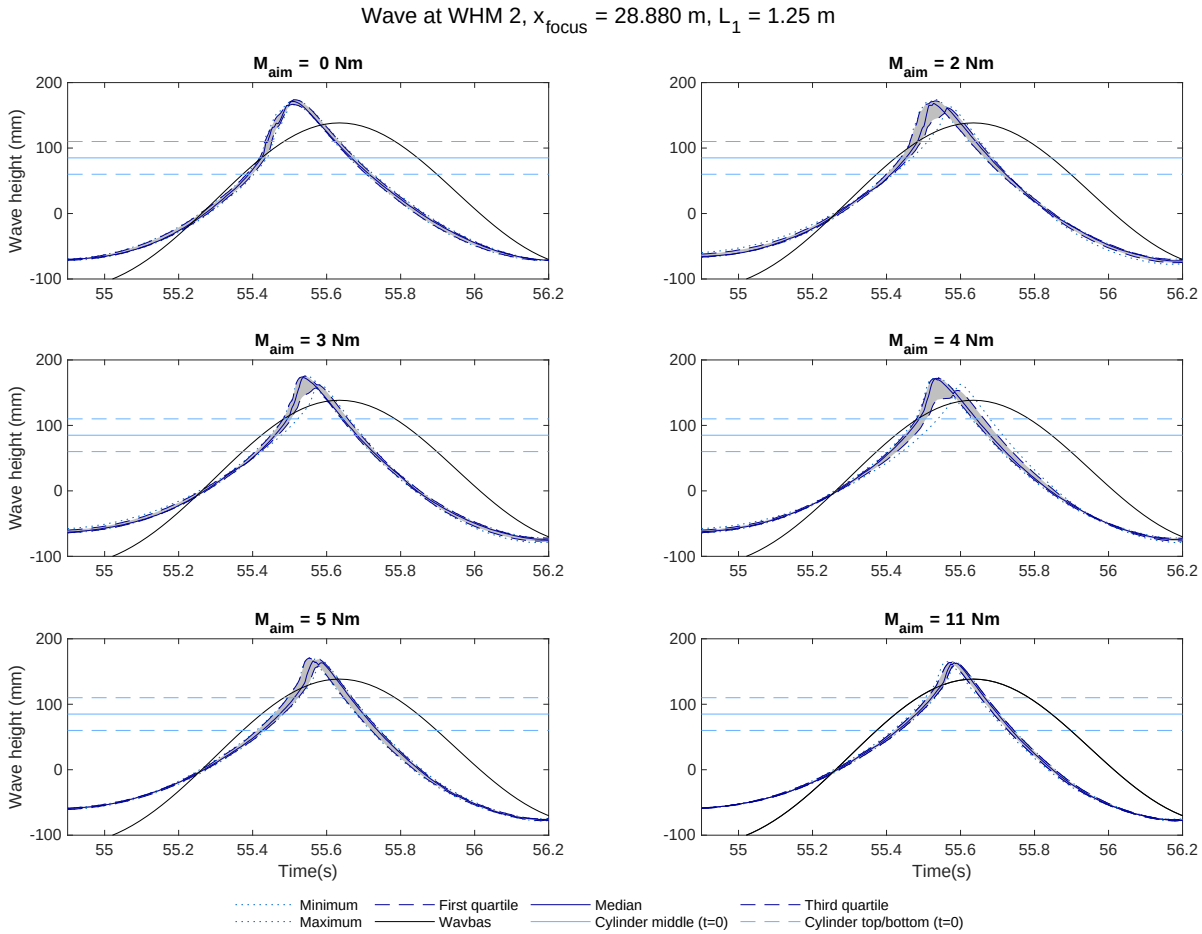

Figure 4.1: Waves with focus location x_{focus} = 28.880 m measured at WHM 2 which are imposed on the longest pendulum. Less spread can be observed than when all the waves are grouped in figure 3.2. More variability in the wave measurements can be observed for situations in which more spread in the relative angle is present. The results from *Wavbas* deviate significantly from the experimental values, which is caused by the assumption of linearity. The level of the cylinder at the start position (t = 0) is shown as well.

First, the waves in which the pendulum is placed are shown in figure 4.1. These measurements are taken at the original position of the pendulum, which is indicated with 'cylinder (t = 0)' as well in this figure. When comparing these signals to all the waves measured, which are presented earlier in the top six diagrams of figure 3.2, the variability is less. This phenomenon can be an indication that fluid-structure interaction (FSI) is an essential factor, and the spread is less due to the same behaviour of the pendulum. This statement is supported by the fact that the variability in the waves is larger when the spread in the relative angle is larger (see figure 4.4). All the median lines of the wave measurements in the different situations of the long pendulum are shown together in figure 4.2. In this figure it is visible that some results differ significantly from the rest, indicating FSI again. The experimental and calculated values are synchronised using the signal of the waveboard. When comparing the results of *Wavbas* to the experimental results, it can be seen that the model is not perfect. The modelled wave is less steep and wider than the measured wave. These differences are caused by the assumption of linearity. Small deformations of the free surface are assumed, which is apparently not sufficient to represent the waves in the experiment.

The top angle of the pendulum, shown in figure 4.3, increases with increasing frictional torque, while the relative angle between the top and bottom part decreases, which is shown in figure 4.4. The top angle is a measure for the elastic deformation of a structure, while the relative angle is a measure for plastic deformation. From this analysis, it can be concluded that more plastic deformation causes less

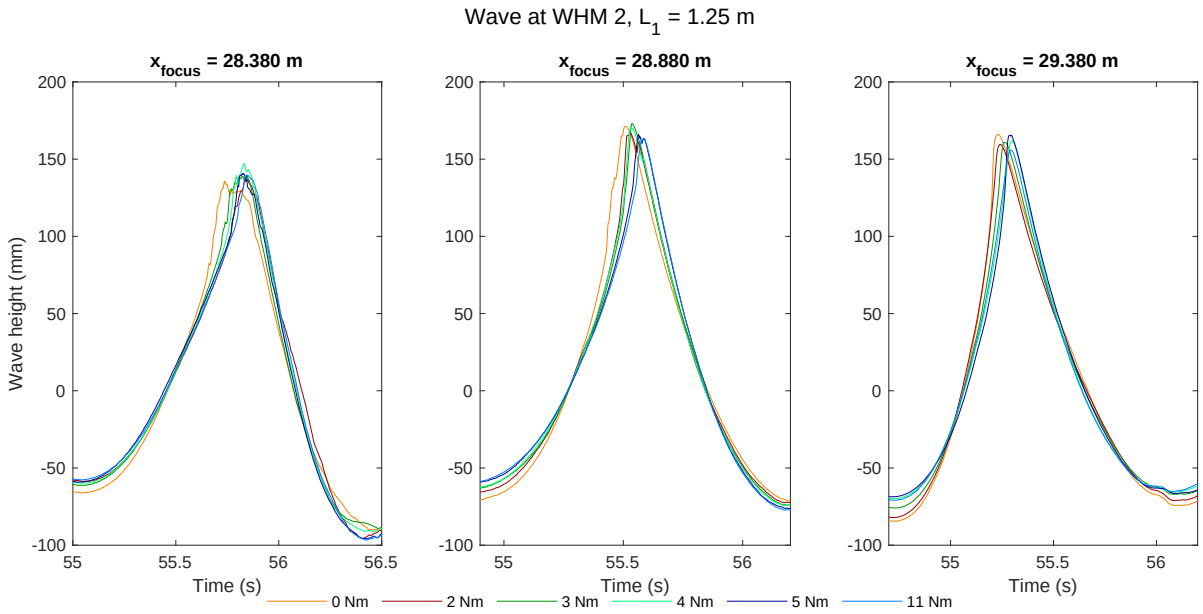

Figure 4.2: The median lines of the wave measurements when the long pendulum is subjected to waves focused at 28.380 m (left), 28.880 m (middle) and 29.380 m (right). The results for some values of the frictional torque (for example 0 Nm) differ significantly from the rest, indicating FSI.

elastic deformation. This conclusion can be translated to a real system as follows: A material more resistant to movement of material dislocations will be less damaged, but will have a larger deflection. Which material will have a higher or lower total energy transfer will be analysed in section 4.2. The oscillation period, which can be seen as a measure for the elastic behaviour, does not change significantly with varying frictional torque. The oscillation period varies between 2.035 and 2.050 s based on the experiment and is 2.050 s based on the results of the model. Before the experiments in the tank were executed, the oscillation period was observed to be 2.050 s using a stopwatch. This unchanged oscillation period after deformation is a logical consequence of the significant weight difference between the top and bottom pendulum. This weight difference causes the influence of the top pendulum on the oscillation period to be dominant over the influence of the bottom pendulum. For the medium and short pendulum, the same behaviour can be observed. For the medium pendulum, the experimental results show values between 1.780 and 1.790 s, the model between 1.810 and 1.815 s and the test with the stopwatch 1.813 s. For the short pendulum, the experimental results show values between 1.497 and 1.517 s, the model between 1.507 and 1.517 s and the test with the stopwatch 1.514 s. The small difference between the stopwatch test and the experimental values can be assigned to reading errors of the graph.

The results of the angles of the reduced-order model and the experiment are synchronised using the synchronisation of the waves. It can be seen that for the situation in which the frictional torque is zero, the modelled value for the top angle rises slower than the experiments. In the other situations, the result of the model increases at the same rate as the experimental result but keeps increasing for a longer time. Therefore, the model overestimates the behaviour of the top angle for all cases in which frictional torque is applied. Next to this, it introduces a phase shift between the results of the model and the experiment. Possible reasons for these phenomena will be discussed in the next paragraphs, together with analysing the results for the relative angle and torque.

The relative angle between the top and bottom pendulum and the measured torque are closely related and are, therefore, shown together in figure 4.4. The results of the reduced-order model and the experiment are synchronised using the synchronisation of the waves. The relative angle decreases with increasing frictional torque. It can be seen that the rate at which the relative angle increases is smaller for the model than for the experiment. This can be due to the shape of the wave. The modelled wave is less steep, and causes, therefore, a more gradually increasing force on the pendulum. The wave force is less ‘impact’-like in the model due to the shape of the wave and creates a lower response

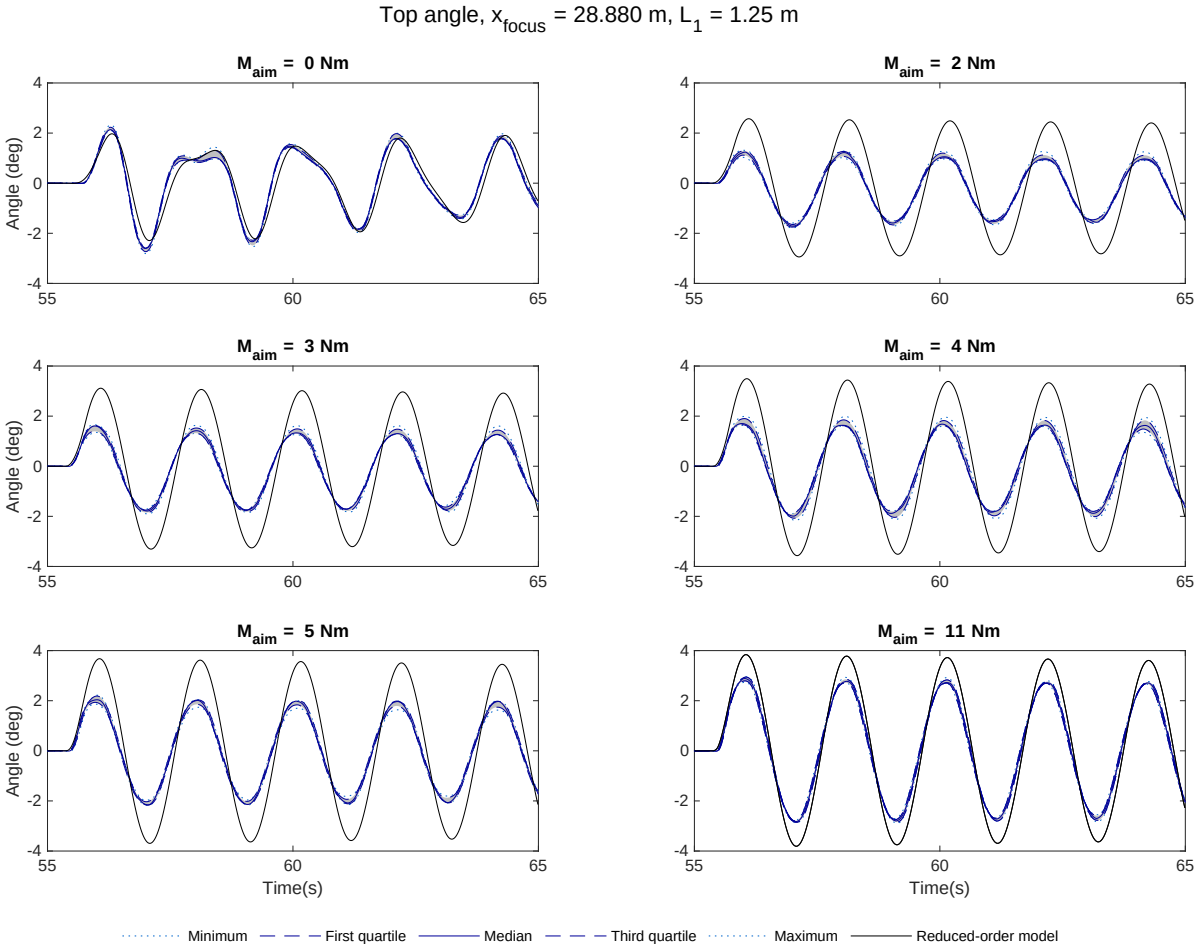

Figure 4.3: Angle of the top part of the longest pendulum subjected to waves focused at x_{focus} = 28.880 m. The time signal is given for six different aim values of frictional torque varying from 0 Nm to 11 Nm. The motion of the top angle shown here simulates the elastic deformation of a structure. This elastic deformation becomes bigger when less plastic deformation occurs, which is the case for increasing frictional torque that the friction mechanism can withstand. The reduced-order model overestimates the experimental values in the situations in which frictional torque is present. The oscillation period of the pendulum is constant with increasing frictional torque.

of the relative angle and a larger response of the top angle of the pendulum, which is shown in figure 4.3. This phenomenon causes a phase shift between the values of the model and the experiment for the situation without frictional torque. Due to this more spread-out wave force, the modelled torque increases more gradually before a relative motion occurs and, therefore, can be seen to develop before the measured torque does.

Furthermore, the modelled torque does not show the large negative dip which can be observed in the experimental results. This dip can even exceed the maximum frictional torque of the friction mechanism creating an asymmetric signal of the frictional torque. This means no motion occurs during this time interval. What does occur could be explained by looking at the relative angle when M_{aim} = 11 Nm. The measured change in relative angle is likely caused by elastic deformation of the rubber of the brake-blocks. This phenomenon can also be observed in other situations, in which a decrease of the relative angle can be seen after reaching its maximum. This decrease is never seen in the model. Therefore, this decrease in the angle could be due to the elastic deformation of the brake-blocks and this could be a cause for the dip in the measured torque, which can not be seen in the modelled torque. However, the wave conditions can also cause this effect in a similar way as described by Davies and Martin (1990). In this research, high added mass coefficients cause a backward horizontal force in diagonal impacts.

Moreover, by looking at the signals of the measured and modelled torque, it should be questioned if the friction is modelled adequately. In the current model, Coulomb friction is used following the equation

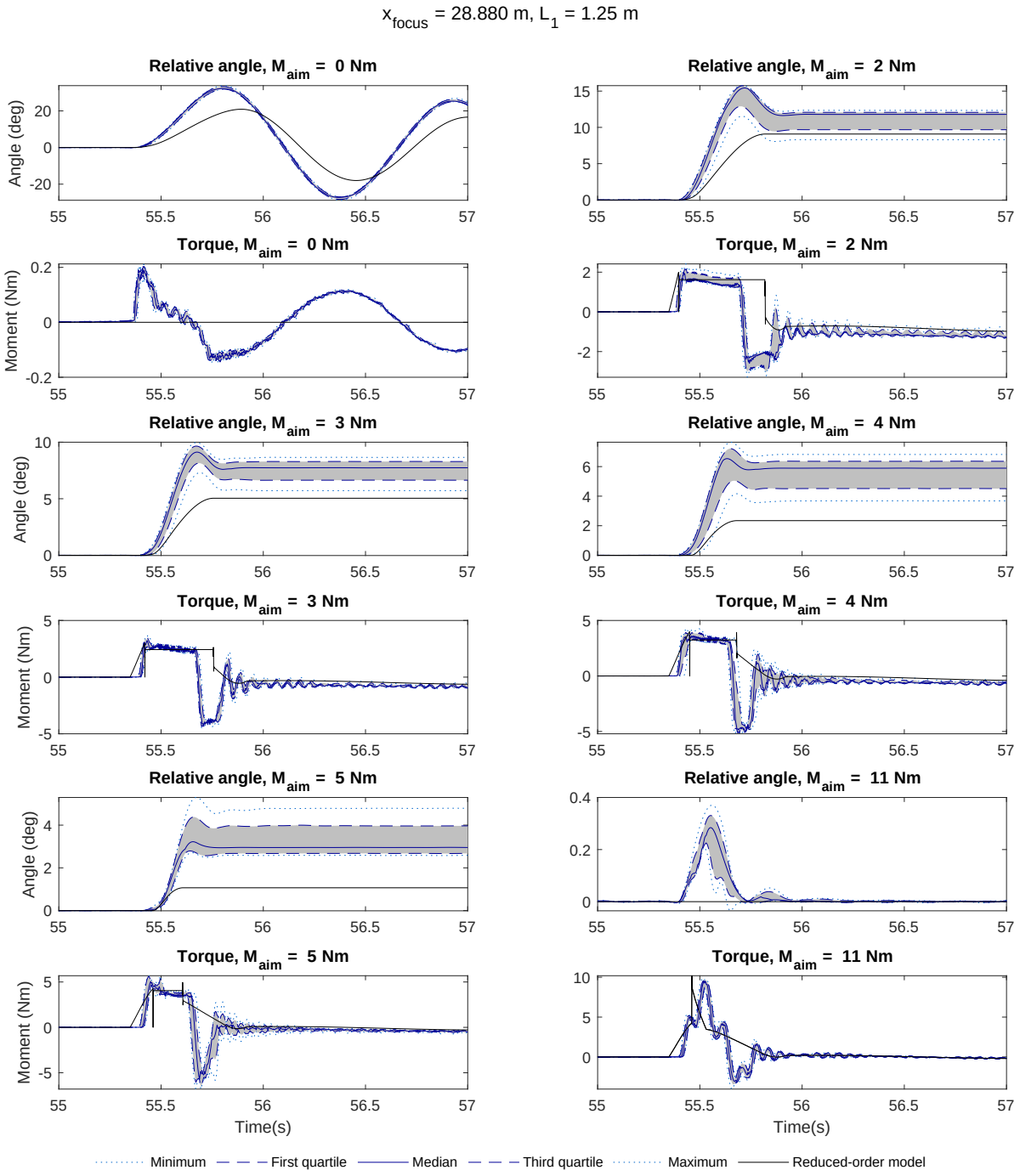

Figure 4.4: The relative angle between the top and bottom part and the measured and modelled frictional torque of the longest pendulum subjected to waves focused at x_{focus} = 28.880 m are shown. The time signals are given for six different aim values for the maximum frictional torque varying from 0 Nm to 11 Nm. The relative angle shown here simulates the plastic response of a structure. This plastic response becomes smaller with increasing frictional torque. The model has a slower increase of the relative angle and the torque than the measured values. Two large differences are observed between the modelled and measured torque. When 0 Nm is applied, the model shows a value of 0 Nm, while the experimental data shows a measured torque due to the motion of the pendulum. In all the other situations a dip in the measured torque is shown, which is not shown in the modelled torque. The time intervals that show more variability in the measured torque also show similar behaviour of the relative angle.

$F_f = \mu F_n$. The model assumes that only two different values of the friction coefficient μ occur, namely the static and dynamic friction coefficient. This assumption leads to a constant frictional torque while a relative motion between the top and bottom pendulum occurs. However, the measured torque slowly

decreases in this same time interval. Therefore, the friction coefficient could depend on for example speed or even temperature. These changes in the friction coefficient are currently not implemented in the model, and they could be an impediment to model the experimental behaviour completely correct.

One other difference occurs between the measured and modelled torque. When 0 Nm is applied, the model shows a value of 0 Nm while the experimental data shows a measured torque. This measured torque is created by the inertia of the disc of the friction mechanism, which exerts a torque on the torque sensor due to its angular acceleration.

The fact that the relative angle and the torque are closely related can be seen in the variability of both signals. The variability in the relative angle could be a result of inaccuracies of the potentiometers. However, the variability in both signals can be related to each other as well. The time intervals that show more variability in the measured torque also show similar behaviour of the relative angle. However, the cause of the variability in the measured torque can at present not be explained. It can partly be a result of variability in the waves or in the friction mechanism itself.

4.2. Energy components to distinguish between elastic and plastic contributions

The second part of the results consists of different energy components that are present in the setup. By presenting these components, the information about the behaviour of the pendulum is lost, but the different lengths and wave conditions can be compared more easily. First, the elastic energy that is absorbed by the double pendulum, which is related to elastic deformation and consists of potential and kinetic energy, is shown in section 4.2.1. In the next section, the most important energy components of this research are shown. The energy components related to plastic deformation, which are the stored and dissipated energy, are shown in comparison with the elastic and total absorbed energy of the pendulum in section 4.2.2.

4.2.1. Elastic energy of the double pendulum

Two different energy components are linked to the elastic energy of the double pendulum, namely the kinetic and potential energy. The formulations used for the calculation of the kinetic energy for the top, bottom and entire pendulum are given in equation 4.1. In these formulations, all values indicated with subscript 1 correspond to the top part of the pendulum and values with a 2 to the bottom part. The angle of the bottom part is relative to the vertical plane, as shown in figure 2.5. This definition means that the measured values in the experiment of potentiometers 1 or 2 and 3 should be added to obtain these values.

$$\begin{aligned} E_{kin,top} &= 0.5 m_1 \dot{\theta}_1^2 h_1^2 + 0.5 I_1 \dot{\theta}_1^2 \\ E_{kin,bottom} &= 0.5 m_2 \left(\dot{\theta}_1^2 L_1^2 + 2\dot{\theta}_1 \dot{\theta}_2 L_1 h_2 \cos(\theta_2 - \theta_1) + \dot{\theta}_2^2 + h_2^2\right) + 0.5 I_2 \dot{\theta}_2 \\ E_{kin,total} &= E_{kin,top} + E_{kin,bottom} \end{aligned} \tag{4.1}$$

The formulations used for the calculation of the potential energy for the top, bottom and entire pendulum are given in equation 4.2.

$$\begin{aligned} E_{pot,top} &= m_1 g h_1 \left(1 - \cos(\theta_1)\right) \\ E_{pot,bottom} &= m_2 g \left(L_1 \left(1 - \cos(\theta_1)\right) + h_2 \left(1 - \cos(\theta_2)\right)\right) \\ E_{pot,total} &= E_{pot,top} + E_{pot,bottom} \end{aligned} \tag{4.2}$$

By combining the kinetic and potential energy, a formulation is established for the elastic energy of the double pendulum, indicated with E_{el} and shown in equation 4.3.

$$\begin{aligned} E_{el,top} &= E_{kin,top} + E_{pot,top} \\ E_{el,bottom} &= E_{kin,bottom} + E_{pot,bottom} \\ E_{el,total} &= E_{kin,total} + E_{pot,total} \end{aligned} \tag{4.3}$$

The elastic energy of the top, bottom and entire pendulum is shown in figure 4.5 for four different frictional moments for the long pendulum in the wave focused at 28.880 m. With increasing frictional moment, the influence of the top pendulum on the total elastic energy increases until the energy of

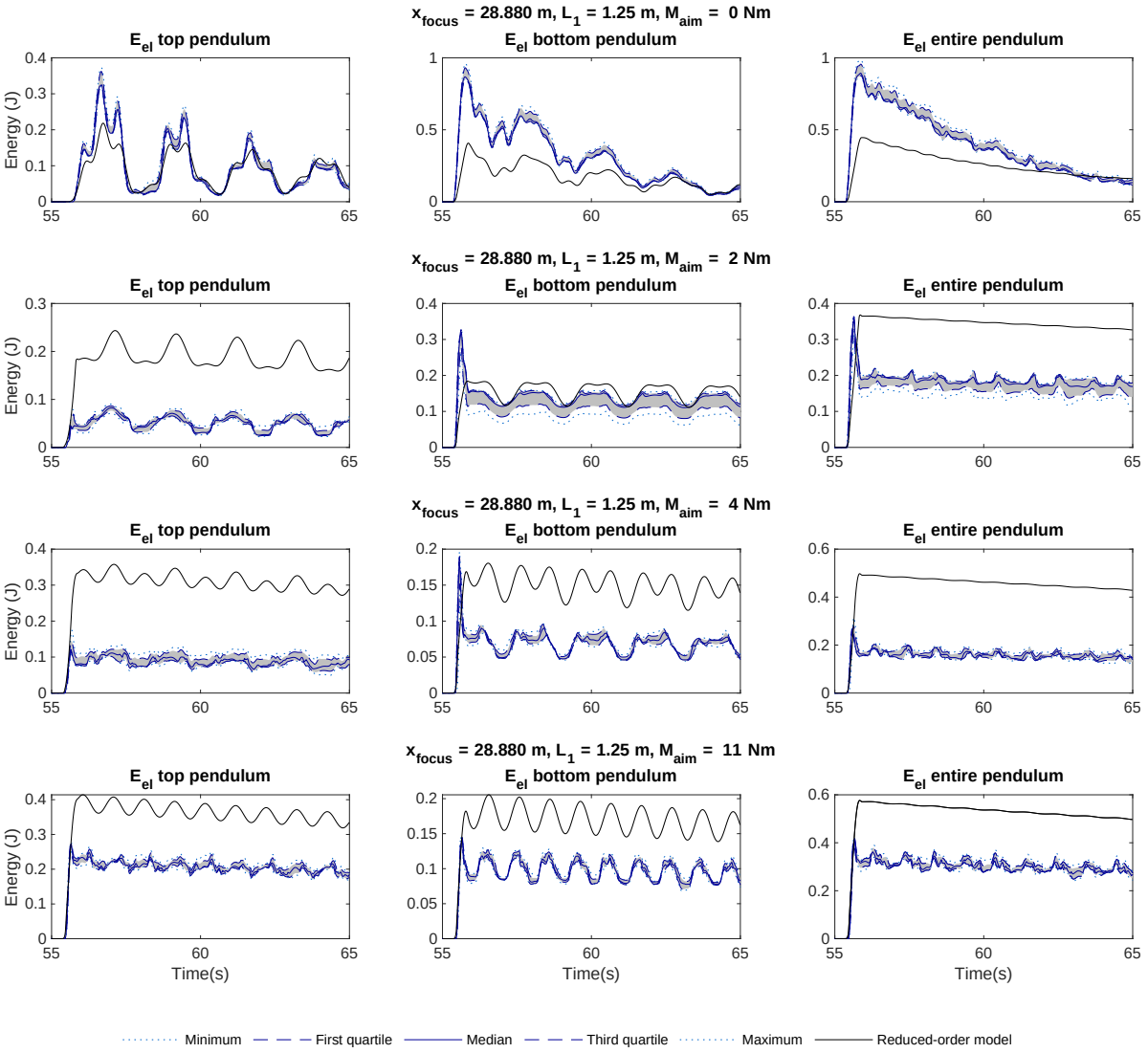

Figure 4.5: The elastic energy of the top, bottom and entire pendulum for four different frictional moments for the long pendulum in the wave focused at 28.880 m. With increasing frictional moment, the influence of the top pendulum on the total elastic energy increases until the energy of the top and bottom pendulum is approximately equal. The model estimates an amount of elastic energy influenced mostly by the top pendulum. For low values of the frictional torque the signal is asymmetric, caused by the relative angle between the two parts of the pendulum. This asymmetry decreases with increasing frictional torque until it complete vanishes for the situation of 11 Nm. This behaviour is correctly modelled, but the values are overestimated for all cases in which frictional torque is present. In all situations, the top and bottom pendulum exchange energy, which results in the oscillating behaviour of the elastic energy of both pendulums separately, but no oscillation in their summed signal.

the top and bottom pendulum is approximately equal. The model does not capture this behaviour and estimates an amount of elastic energy influenced mostly by the top part of the pendulum. The energy is overestimated by the model for all cases in which frictional torque is present. For low values of the frictional torque, it can be seen that for both parts of the pendulum the signal is asymmetric, caused by the relative angle between them. This asymmetry decreases with increasing frictional torque until it complete vanishes for the situation in which 11 Nm is applied and only a single hinge pendulum remains. The behaviour of the signal is modelled correctly. In all situations, the top and bottom pendulum exchange energy, which results in the oscillating behaviour of both pendulums separately, but no oscillation in their summed signal. In the outer position of the pendulum, the potential energy of both pendulums is maximal. During the downward motion, the top pendulum influences the bottom pendulum, resulting in an energy transfer from top to bottom. Therefore, the kinetic energy of the top pendulum is lower than its potential energy, while the kinetic energy of the bottom pendulum is higher than its potential energy. This phenomenon explains the oscillating behaviour in the separate signals.

4.2.2. Energy related to plastic deformation

After the double pendulum is hit by the wave, there will be an angle between the top and bottom part due to the friction mechanism, called the relative angle. The potential energy, which can be calculated by inserting the final top and relative angle in equation 4.2, will be called the stored energy (E_{stor}). This value is the amount of energy stored in the plastic deformation. A short description of this component together with the other components is given in table 4.1.

The second energy component related to the plastic deformation is the dissipated energy in the friction mechanism. The formulation used for the calculation of the dissipated energy is:

$$E_{diss} = \int |M_f| d\theta \tag{4.4}$$

For most cases, these two energy components support the same conclusion. When this is not the case, the largest component will have more influence. Both components are shown in the top two diagrams of figure 4.6 for the long pendulum in all wave conditions and figure 4.8 for all pendulums in the wave focused at 28.880 m. As can be seen in these figures, the dissipated energy is significantly larger than the stored energy. Therefore, it is decided that only the dissipated energy is analysed when talking about plastic deformation in the rest of this report.

It is important to see the magnitude of the dissipated and elastic energy relative to the total absorbed energy, which is, therefore, introduced here:

$$E_{abs} = E_{kin} + E_{pot} + E_{diss} \tag{4.5}$$

This component is the summation of the total kinetic energy, the total potential energy and the dissipated energy. The maximum of the total absorbed energy of the system is not necessarily the moment of either the maximum kinetic, potential or dissipated energy.

Table 4.1: A summary of the four most important energy components in the system: elastic, dissipated, stored and total absorbed energy.

Symbol	Full name	Description of component
E_{el}	Elastic energy	The sum of the kinetic and potential energy is defined to be the elastic energy, which is a measure for the elastic deformation of a structure. The strain energy due to deformation of the pendulum is neglected, and, therefore, this energy could also be called the energy of the rigid body. This energy component is the energy that would stay conserved in the system when no losses would occur during oscillation.
E_{diss}	Dissipated energy	Energy is dissipated in the friction hinge in the form of heat when a relative motion between the top and bottom pendulum occurs. The energy that is lost due to this mechanism is a measure for the amount of plasticity in the system.
E_{stor}	Stored energy	After the double pendulum is hit by the wave, there will be an angle between the top and bottom part of the pendulum. The potential energy at this final angle is called the stored energy and is a measure for the final plastic deformation. This energy component is 2 - 4 times smaller than the dissipated energy and is, therefore, not used for the conclusions.
E_{abs}	Total absorbed energy	This component is the total energy transferred from the wave to the pendulum. This is a summation of the kinetic and potential energy and the energy dissipated in the friction hinge. This is equal to the sum of the elastic and dissipated energy discussed above.

Figures 4.6 to 4.9 present the stored, dissipated, elastic and absorbed energy of L_1 = 1.25 m (figures 4.6 and 4.7) and x_{focus} = 28.880 m (figures 4.8 and 4.9). The stored energy will not be discussed in detail due to the fact that is 2 - 4 times smaller than the energy dissipated in the friction hinge. In all figures, the results of the experiments are shown as individual data points. On the y axis the energy is

shown and on the x axis the maximum measured torque in the experiment or the static torque of the model is shown. To show the behaviour of the energy as function of the frictional moment more clearly, a coloured area around these data points is added. The outer bounds of this colour area are cubic splines which are fitted through outer data points selected by hand. Some outlying data points, which are selected visually, are not taken into account for this cubic spline. The average of these outer lines is shown as well. The variability of the energy is loosely defined as the bandwidth between these outer lines.

In general, more elastic energy is transferred to the pendulum when the frictional torque is below 3 Nm or above 4 or 5 Nm. The elastic energy reaches a minimum around frictional values of 3 - 4 Nm. The reduced-order model underestimates the values for the situation with 0 Nm torque, which is due to the fact that the energy of the bottom pendulum is underestimated and out of phase with the experimental values, leading to a lower maximum amount of energy of the top and bottom pendulum combined. The model overestimates the situations with a frictional torque above 2 or 3 Nm. This can be explained by the fact that for values of the frictional torque above 3 Nm, the model follows the behaviour of the top pendulum, while the experimental values follow an average behaviour between both parts of the pendulum. This phenomenon is caused by an overestimation of the model of the top angle and an underestimation of the relative angle between the top and bottom pendulum.

The dissipated energy decreases with increasing frictional torque. Values of the frictional torque above 2 Nm allow for decreasing angles between top and bottom pendulum with increasing frictional torque, which results in a decreasing amount of dissipated energy, which is modelling plastic energy. The dissipated energy should be equal to zero for 0 and 11 Nm, but as discussed before in section 4.1, the measured torque is influenced by the motion of the pendulum, which influences the dissipated energy as shown in equation 4.4.

The total absorbed energy decreases with increasing frictional torque. This means that when a structure allows for more plastic deformation, the total absorbed energy will be larger. The model shows a different behaviour than the experiment. According to the model, the absorbed energy increases with increasing torque until a frictional torque of 3 Nm. After that point the maximum absorbed energy decreases again. This large difference is mainly caused by an underestimation of the elastic energy for values of the frictional torque below 1.5 Nm, which is a consequence of the wave modelling.

Figures 4.7 and 4.9 show which part of the total absorbed energy goes to the motion of the double pendulum (representing the elastic deformation) and which part is dissipated in the friction hinge (representing plastic deformation) of the pendulum. Ratio $E_{el,max}/E_{abs,max}$ is approximately equal to 1 for 0 and 11 Nm and ratio $E_{diss,max}/E_{abs,max}$ is equal to 0 in these cases. This is due to the fact that no plasticity occurs in these situations. At 0 Nm, no frictional torque is present, while at 11 Nm no relative angle between the top and bottom pendulum occurs. Ratio $E_{el,max}/E_{abs,max}$ shows a minimum around values for the frictional torque of 3 - 4 Nm, while ratio $E_{diss,max}/E_{abs,max}$ is maximal in that situation.

The stored, dissipated, elastic and total absorbed energy of the long pendulum are shown in figure 4.6. When only elastic behaviour occurs, so for 0 Nm or values of the frictional torque above 8 Nm, the experiment shows that the wave focused at 28.380 m transfers the most elastic energy to the pendulum. In the situations with values of the frictional torque below 4 Nm, the wave focused at 29.380 m causes the most elastic energy transfer. Above this value, the wave focused at 28.380 m causes the most elastic energy transfer.

Next to this, it can be seen that the dissipated energy is the highest for the wave focused at 29.380 m, then 28.880 m and the lowest for 28.380 m. The model does not capture this, which is explained by the waves not being modelled correctly. It also shows the importance of the wave elevation, velocity and acceleration in the model. The variability in dissipated energy is the largest due to the wave focused at 28.380 m.

Approximately the same behaviour as for the dissipated energy can be seen in the experimental values of the maximum absorbed energy. The wave focused at 29.380 m causes the most absorbed energy of the pendulum. The wave focused at 28.380 m causes again the most variability. For the situations with 0 or 11 Nm torque, the absorbed energy in the wave focused at 28.380 m is the largest since it is almost only influenced by the elastic energy of the double pendulum.

The elastic and dissipated energy shown in figure 4.6 are shown again in figure 4.7, but now they are divided by the maximum absorbed energy for the pendulum with L_1 = 1.25 m. It seems that the wave

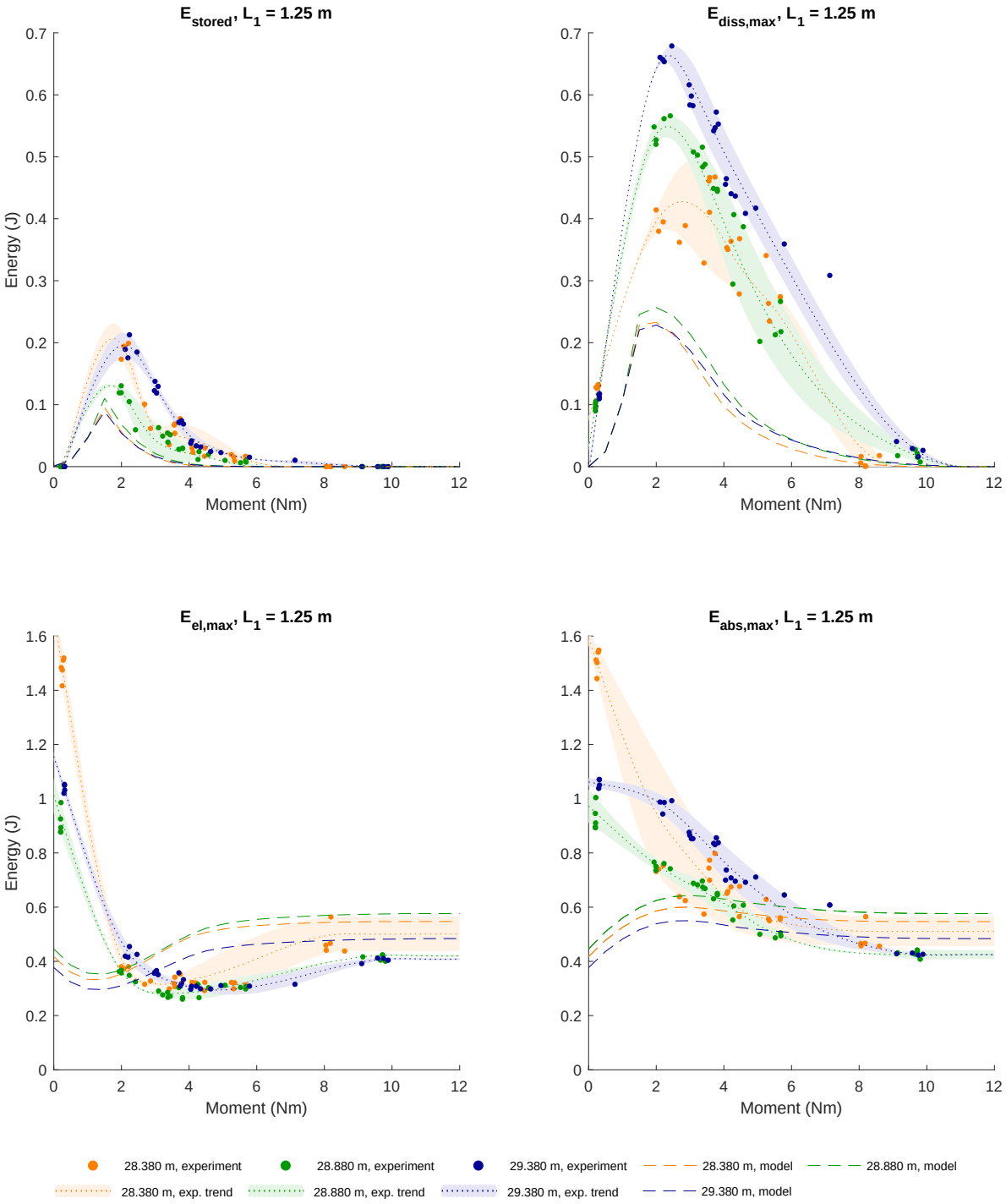

Figure 4.6: The stored (top left), dissipated (top right), elastic (bottom left) and total absorbed energy (bottom right) of the long pendulum are shown. In the situations with values of the frictional torque between 1 and 4 Nm, the wave focused at 29.380 m causes the most elastic energy transfer. In the other situations, the wave focused at 28.380 m causes the most elastic energy transfer. The dissipated energy is the highest for the wave focused at 29.380 m, then 28.880 m and the lowest for 28.380 m. The wave focused at 29.380 m causes the most absorbed energy by the pendulum. The absorbed energy decreases with increasing frictional torque. The model shows a different behaviour than the experiment for the absorbed energy. According to the model, the absorbed energy increases with increasing torque until a frictional torque of 3 Nm. After that point the maximum absorbed energy decreases again. The wave focused at 28.380 m causes the most variability for all energy components.

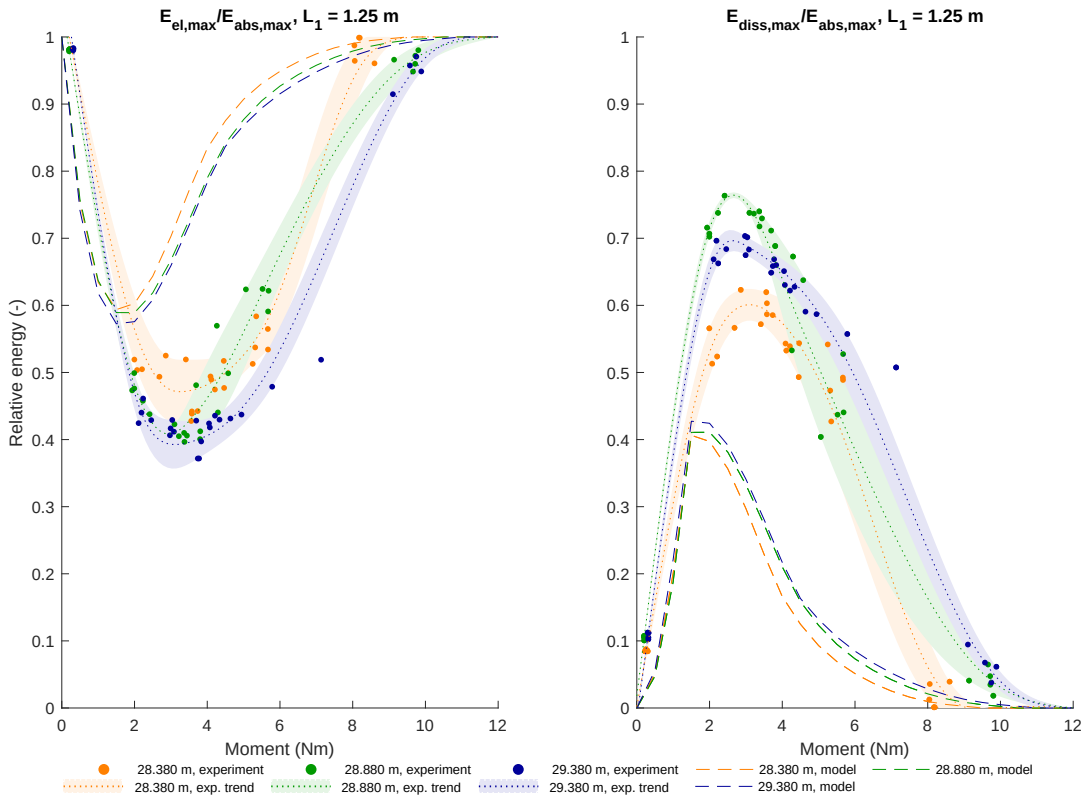

Figure 4.7: The relative transferred elastic energy to the long pendulum is shown in the left figure. The relative dissipated energy is shown in the right figure. These figures show which part of the total absorbed energy goes to the motion of the double pendulum and which part is dissipated in the plastic deformation of the pendulum. Ratio $E_{el,max}/E_{abs,max}$ is equal to 1 for 0 and 11 Nm and $E_{diss,max}/E_{abs,max}$ is equal to 0. The wave focused at 28.380 m transfers more elastic energy to the pendulum than the other two conditions. The model predicts this correctly. For values of the frictional torque below 5 Nm, the value of the dissipated energy over the absorbed energy is higher for the wave focused at 28.880 m, while at higher values the wave focused at 29.380 m creates the most energy dissipation. The model does predict the latter correctly.

focused at 28.380 m transfers more relative elastic energy to the pendulum than the other two wave focus locations for values of the frictional torque below 4 Nm and above 7 Nm. However, the variability of the data of the wave focused at 28.880 m makes a clear interpretation difficult for values of the frictional torque above 4 Nm. The model predicts that the wave focused at 28.380 m causes the most relative elastic energy transfer to the pendulum. For values of the frictional torque below 5 Nm, which means more plastic deformation and energy, the value of the dissipated energy over the absorbed energy is higher for the wave focused at 28.880 m. At values of the frictional torque above 5 Nm, the wave focused at 29.380 m creates the most energy dissipation. The model predicts the latter correctly.

The different lengths of the pendulum are compared in figure 4.8. The stored, dissipated, elastic and total absorbed energy of the double pendulum are shown, but now for focus location x_{focus} = 28.880 m. The pendulum with L_1 = 0.65 m has the most elastic energy transfer in situations with an applied frictional torque, which is correctly predicted by the model. This is due to the fact that this pendulum is lighter overall and will move more easily. The elastic energy is approximately the same for the other two lengths of the pendulum. For the situation in which 0 Nm is applied, the values for the elastic energy are approximately the same for all pendulum lengths, but slightly smaller for the pendulum with L_1 = 0.65 m.

It can be seen that the dissipated energy of the two longest pendulums is higher than the one of the short pendulum. However, due to the variability in the signals of the two longest pendulums, it is difficult to see which one dissipates more energy. The model correctly predicts that the values of these two pendulums are close together and that the dissipated energy of the short pendulum is the lowest.

The absorbed energy is the largest for L_1 = 0.95 m and smallest for L_1 = 0.65 m. At values of

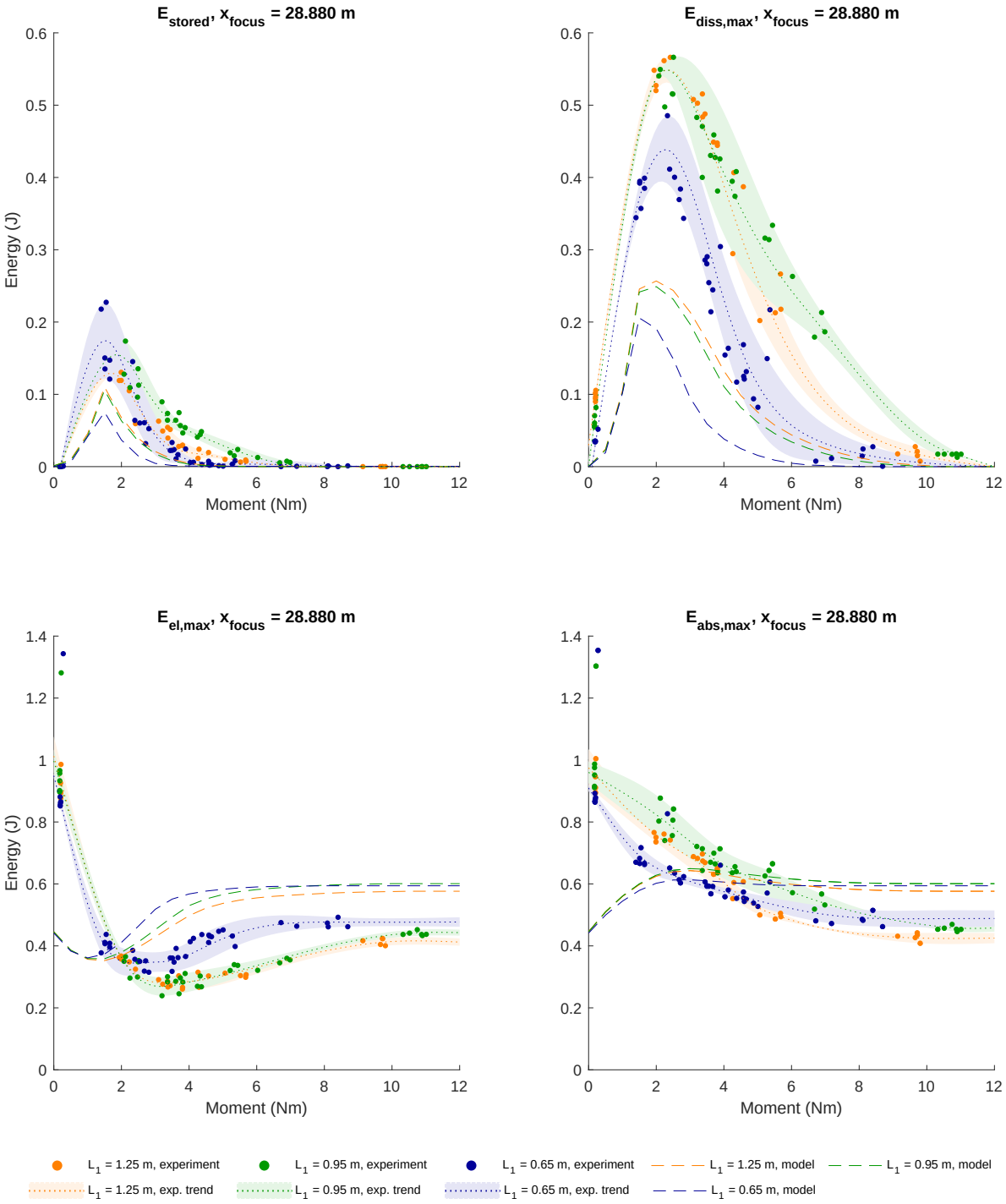

Figure 4.8: The stored (top left), dissipated (top right), elastic (bottom left) and total absorbed energy (bottom right) of the pendulums subjected to the wave focused at x_{focus} = 28.880 m are shown. The pendulum with L_1 = 0.65 m has the most elastic energy transfer. It can be seen that the dissipated energy of the two longest pendulums is higher than the one of the short pendulum. The absorbed energy is the largest for L_1 = 0.95 m and smallest for L_1 = 0.65 m. The absorbed energy decreases with increasing frictional torque. The model shows a different behaviour than the experiment for the absorbed energy. According to the model, the absorbed energy increases with increasing torque until a frictional torque of 3 Nm. After that point the maximum absorbed energy decreases again.

the frictional torque above 3 Nm, more spread can be observed, which makes is difficult to determine which pendulum absorbs the most energy.

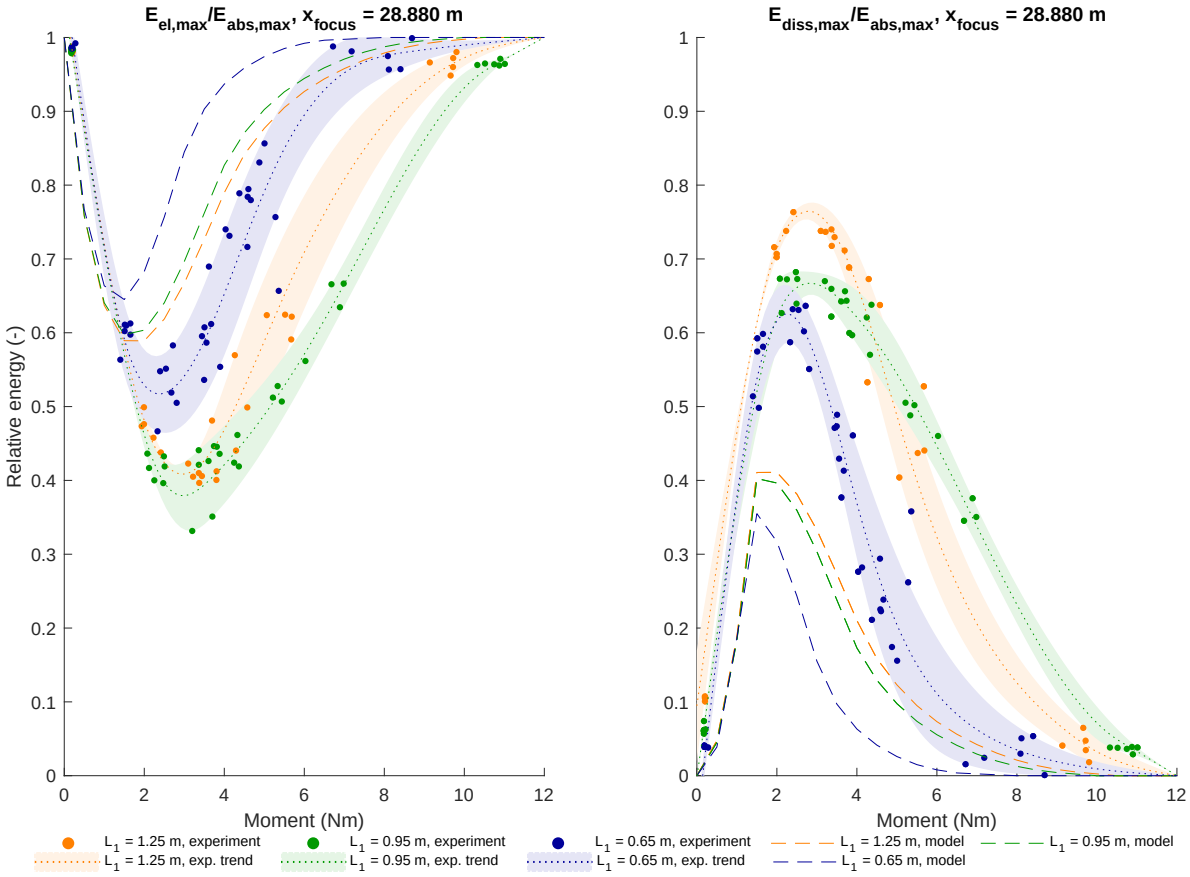

Figure 4.9: The relative transferred elastic energy to the pendulums subjected to the wave focused at x_{focus} = 28.880 m is shown in the left figure. The relative dissipated energy is shown in the right figure. These figures show which part of the total absorbed energy goes to the motion of the double pendulum and which part is dissipated in the plastic deformation of the pendulum. Ratio $E_{el,max}/E_{abs,max}$ is equal to 1 for 0 and 11 Nm and $E_{diss,max}/E_{abs,max}$ is equal to 0. The pendulum with L_1 = 0.65 m has the most energy transfer to the pendulum, but the least dissipated energy. The relative elastic energy transfer to the other two pendulums is approximately equal for values of the frictional torque below 4 Nm. At values of the frictional torque below 5 Nm, the pendulum with L_1 = 1.25 m dissipates more energy relatively than the pendulum with L_1 = 0.95 m, but at values of the torque above 5 Nm, the pendulum with L_1 = 0.95 m dissipates the most energy relatively. The model predicts the behaviour at values of the frictional torque below 5 Nm correctly.

The elastic and dissipated energy shown in figure 4.8 are shown again in figure 4.9, but now they are divided by the maximum absorbed energy for the wave focused at x_{focus} = 28.880 m. The most relative elastic energy is transferred to the pendulum with L_1 = 0.65 m, and this pendulum dissipates the least amount of energy. This is correctly predicted by the model. At values of the frictional torque below 4 Nm, the other two pendulums have an approximately equal amount of relative elastic energy, which is also due to the variability in both results. At higher values of the frictional torque, the pendulum with L_1 = 0.95 m has the least amount of relative elastic energy. For values of the frictional torque below 5 Nm, which means more plastic deformation and energy, the value of the dissipated energy over the absorbed energy is higher for the pendulum with L_1 = 1.25 m. The model predicts this correctly. At higher values of the frictional torque, the pendulum with L_1 = 0.95 m dissipates the most energy relatively.

The overall behaviour of the elastic energy shows a minimum at 3 or 4 Nm, which means that the elastic energy of the pendulum is larger for either lower or higher values of the frictional torque. The dissipated energy decreases with increasing frictional torque when the torque is larger than 2 Nm. Values of

the frictional torque above 2 Nm allow for decreasing angles between top and bottom pendulum with increasing frictional torque, which results in a decreasing amount of dissipated or plastic energy. The experimental values of the total absorbed energy decrease with increasing frictional torque. This means that when a structure allows for more plastic deformation, the energy that will be absorbed in total is larger.

The wave focused at 29.380 m causes the most total energy absorption. When comparing the different pendulums, the pendulum with L_1 = 0.95 m absorbs the most energy. A part of this total absorbed energy per situation originates from the elastic energy and a part from the plastic energy. The shortest pendulum contains the most elastic energy and the least plastic energy, while the longest pendulum, in which the stiffness ($k = mgh$) of the bottom and top pendulum differ most, contains the most plastic energy for values of the frictional torque below 5 Nm. For higher values of the frictional torque, the pendulum with medium length has the most relative energy dissipation. When looking at the different focus locations, it seems that the wave focused at 28.380 m transfers more relative elastic energy to the pendulum than the other two wave focus locations for values of the frictional torque below 4 Nm and above 7 Nm. However, the variability of the data of the wave focused at 28.880 m makes a clear interpretation difficult for values of the frictional torque above 4 Nm. For values of the frictional torque below 5 Nm, the value of the relative dissipated energy is higher for the wave focused at 28.880 m. At higher values of the frictional torque, the wave focused at 29.380 m creates the most energy dissipation. All energy components show more variability for the wave focused furthest away from the pendulum. This observation could mean that more air that is trapped in the water leads to more variability. The amount of variability in the energy differs as well over the situations with different amounts of frictional torque, which models the amount of plasticity. However, these variations in variability do not show a pattern, which makes it not possible to draw a conclusion for the relation between variability and plasticity.

The reduced-order model can predict the behaviour of the elastic and plastic energy transfer. It can, however, not predict the behaviour of the total absorbed energy accurately. According to the model, the absorbed energy increases with increasing torque until a frictional torque of 3 Nm. After that point the maximum absorbed energy decreases again. This large difference between the experiment and the model is mainly due to the fact that the elastic energy is underestimated at values of the frictional torque lower than 1.5 Nm. The model can predict the differences that occur between the different lengths of the pendulum. For the different waves it can not always correctly predict the differences in transferred energy. Only small deformations of the free surface are assumed in the current model, which is not sufficient to represent the waves in the experiment.

5

Conclusions & Recommendations

After introducing the problem in chapter 1, giving the steps taken towards the solution in chapters 2 and 3, and presenting the results in chapter 4, this chapter gives the conclusions and recommendations. First, the conclusions on the research question and the sub-questions presented in chapter 1 are shown in section 5.1. After that, the recommendations for further research are given in section 5.2.

5.1. Conclusions

Ship and offshore structures can deform plastically due to a hydrodynamic impact, which can lead to structural failure if the load is too high. In existing literature a clear gap is identified, which shows that a focused approach to investigate the influence of plasticity on fluid-structure interaction (FSI) does not exist. To investigate this influence, we proposed to use a pendulum with few degrees of freedom and known properties, so that the emphasis of the experiment can be on FSI. We answer the following question with an experiment and reduced-order model:

What is the influence of plasticity on the behaviour of a pendulum in breaking waves?

Two hypotheses to this main question were formed in chapter 1.

1. The influence of the plastic deformation of the pendulum causes energy absorption. It is expected that situations with a higher resistance to plastic deformation absorb less plastic energy when loaded with the same wave. Next to this, pendulums with a higher stiffness are expected to absorb more energy while plastic deformation occurs.
2. Variability in the transferred energy could indicate the importance and influence of the plasticity on the behaviour. However, the variability could also be a result of the different amounts of trapped air in the breaking wave.

In order to answer the main question and to test the two hypotheses, an experimental setup is designed. Three different arrangements of a double pendulum with different properties are subjected to three focused waves with their focus location at three different locations. These focus locations are 0.5, 1.0 and 1.5 m in front of the pendulum. The pendulum has two hinges of which the bottom hinge incorporates frictional torque, which simulates the plasticity in the structure. A reduced-order model is constructed to be able to predict the pendulum behaviour. The steps described here are used to answer the sub-questions which form a support to the research goal. The conclusion to each sub-question formulated in chapter 1 is presented.

1. **What are the typical conditions when breaking waves are formed? How can these waves be modelled?**
   Breaking waves are formed when the ratio of height over length, also known as the steepness of the wave, becomes too large. The criterium for this is dependent on the water depth. Different forms of breaking waves can be observed, namely the slosh impact, flip-through impact, air pocket impact and aerated impact.

In an experiment, a focused wave can lead to a breaking wave. A focused wave is built up of different regular wave components that are in phase at the focus location. Using the information that the envelope travels with the group velocity and the wave inside the envelope follow the standard wave equation $\eta = Acos(kx - \omega t)$, the signal required at the wavemaker can be calculated. When this focused wave is sufficiently steep, it will generate a breaking wave.

In a reduced-order model, an analytical formulation for the wave exerted by a breaking wave should be found. No research on an analytical formulation for a breaking wave on a horizontal cylinder is found in literature. Therefore, a formulation for a plunging wave on a vertical pile, which is based on the frontal area of the wave, is used. The frontal area of this wave can be based on a simulation that solves the potential equation. The fact that small deformations of the free surface are assumed, makes it impossible to directly simulate a breaking wave. When using these wave characteristics, the elastic response of the pendulum is overestimated and the plastic response underestimated.

2. **How can a simple pendulum be adjusted to allow plastic deformation? How can this be implemented in a reduced-order or experimental approach?**
To understand how a simple pendulum can be adjusted to allow plastic deformation, a method of mimicking or simulating plastic deformation should be found. In this way, no structure is damaged, which makes the experiment more repeatable. The *Yield Point Theory* is a plasticity theory that assumes a certain shear stress is needed to initiate the motion of the dislocations in the material. After that point, a lower stress is required for dislocation movement. The mechanical approach of approximating this plasticity model is by using a friction model. When this friction is modelled as the Coulomb friction, the friction force is constant. The formulation for this is equal to $F_f = \mu F_n$. This formulation means that the friction force is equal to a coefficient of friction times a force normal to the two frictional surfaces. When a static and dynamic friction coefficient are taken into account, the friction represents the *Yield Point Theory*.

   A simple pendulum with only one hinge can simulate either elastic or plastic behaviour, but not both. Therefore, a second hinge is required in the pendulum setup. The top hinge is a normal hinge without additional friction, while the bottom hinge is a hinge in which friction can be applied to model plasticity. The amount of frictional torque can be modified by adjusting the normal force that is applied to the friction mechanism. The most extensive range of values for the frictional torque that leads to plastic deformation can be found when the top part of the pendulum is heavier and longer than the bottom part. Next to this, the centre of gravity of the top part should be low, while the centre of gravity of the bottom part should be high.

   The double pendulum with one regular and one friction hinge can be modelled using Lagrange's equation. In the reduced-order model, the frictional torque is assumed to be smaller than the static friction when no motion is induced, but equal to the dynamic friction when relative motion between the top and bottom pendulum occurs.

3. **When measuring the energy transfer from the waves to the pendulum, which energy components can indicate the influence of plasticity in the result?**
The different energy components that are used for analysing the energy transfer from the wave to the pendulum are the kinetic, potential, stored, dissipated and total absorbed energy. The stored energy is the potential energy of the pendulum calculated with the final top and bottom angle. The dissipated energy during the plastic deformation is equal to the integration of the torque over the relative angle between the top and bottom pendulum. A summation of the potential, kinetic and dissipated energy is assumed to be a suitable measure for the total energy transferred from the wave to the pendulum and is called the total absorbed energy. The kinetic and potential energy are related to the elastic deformation of the pendulum. The stored and dissipated energy are related to plastic deformation. Since the dissipated energy is larger than the stored energy, analysing the dissipated energy and comparing it to the total absorbed energy in the pendulum can give a measure of how much the influence of plasticity is in every examined situation.

The conclusion to the report will be mainly based on the experimental results. The capacity of the model to estimate these conclusions will be evaluated as well. In order to answer the main question, the hypotheses stated above are addressed again, taking the answers to the sub-questions into account.

The first hypothesis focuses on plastic deformation with respect to resistance to plasticity and stiffness of the pendulum. The results show that situations with a higher value of the frictional torque show less plastic deformation. The stiffness of the pendulum increases with increasing length. Therefore, the results will be analysed concerning the values of the frictional torque and length of the pendulums.

The first aspect of the behaviour that is analysed is the motion of the pendulum, which, in our approach, models the deformation of a structure. Compared to the situation in which sufficient friction is applied to create a single hinge pendulum, situations with less friction have a smaller response of the angle of the top part of the pendulum. The lower the value of the applied friction, the larger the relative angle between the top and bottom pendulum is. These results can be translated into the analysis of different energy components that make it possible to distinguish between elastic and plastic behaviour. Compared to the single hinge pendulum, the elastic energy of the pendulum decreases with decreasing values of the frictional torque. However, at values of the frictional torque below 3 Nm, the inertia of the pendulum influences the motion of the pendulum and the values for the elastic energy increase again. The dissipated energy in the friction hinge, modelling plastic energy, decreases with increasing frictional torque when the torque is larger than 2 Nm. The most surprising influence of FSI on the behaviour of the pendulum can be seen in the energy transferred from the wave to the structure, called 'total absorbed' energy. The total absorbed energy decreases with increasing frictional torque. This means that when a structure allows for more plastic deformation, the energy that will absorbed in total is larger.

The wave focused at 29.380 m causes the most total energy absorption. When comparing the different pendulums, the pendulum with L_1 = 0.95 m absorbs the most energy. A part of this total absorbed energy per situation originates from the elastic energy and a part from the plastic energy. The shortest pendulum contains the most elastic energy and the least plastic energy, while the longest pendulum, in which the stiffness ($k = mgh$) of the bottom and top pendulum differ most, contains the most plastic energy for values of the frictional torque below 5 Nm. For higher values of the frictional torque, the pendulum with medium length has the most relative energy dissipation. When looking at the different focus locations, it seems that the wave focused at 28.380 m transfers more relative elastic energy to the pendulum than the other two wave focus locations for values of the frictional torque below 4 Nm and above 7 Nm. However, the variability of the data of the wave focused at 28.880 m makes a clear interpretation difficult for values of the frictional torque above 4 Nm. For values of the frictional torque below 5 Nm, the value of the relative dissipated energy is higher for the wave focused at 28.880 m. At higher values of the frictional torque, the wave focused at 29.380 m creates the most energy dissipation.

A reduced-order model is constructed to help explain the results. It can predict the behaviour of the elastic and plastic energy transfer. It can, however, not predict the behaviour of the total absorbed energy accurately. According to the model, the absorbed energy increases with increasing torque until a frictional torque of 3 Nm. After that point the maximum absorbed energy decreases again. This large difference between the experiment and the model is mainly due to the fact that the elastic energy is underestimated at values of the frictional torque lower than 1.5 Nm. The model can predict the differences that occur between the different lengths of the pendulum. For the different waves it can not always correctly predict the differences in transferred energy. Only small deformations of the free surface are assumed in the current model, which is not sufficient to represent the waves in the experiment.

The second hypothesis focuses on variability in the results. All energy components of the double pendulum show more variability for the wave focused furthest away from the pendulum. This observation could mean that more air that is trapped in the water leads to more variability. The amount of variability in the energy differs as well over the situations with different amounts of frictional torque, which models the amount of plasticity. However, these variations in variability do not show a pattern, which makes it not possible to draw a conclusion for the relation between variability and plasticity. The model can not show variability and does, therefore, not contribute when addressing the second hypothesis.

5.2. Recommendations

This section presents the recommendations for further research.

1. The most important recommendation is based on the way the wave impact is incorporated into the reduced-order model. In the current wave model *Wavbas*, only linear effects are taken into account. This restrains the model to model breaking waves, which results in different impact conditions. The current impact conditions overestimate the elastic behaviour and underestimate the plastic behaviour and can not distinguish the different waves correctly. An example of a numerical code that can describe breaking waves accurately and could be used as a starting point for further calculations is given by Peregrine et al. (2005). In this research, they use a method that uses irrotational incompressible inviscid flow to compute a breaking wave. This would include convective acceleration terms in the equations used for the current calculations. The most severe case that can be modelled according to Peregrine et al. (2005) is between a sloshing and air pocket impact. When the pressures become large, compressibility and the interaction with air should be incorporated as well. Using irrotational incompressible inviscid flow, wave breaking can be simulated, likely resulting in a better prediction of the differences in pendulum behaviour between the three focus locations. This is expected to result in a better agreement between the model and experiment.

2. For this research, the choice is made to use a wave with a single impact on the pendulum. Large or extreme wave impacts are directly related to the Ultimate Limit State, which is the basis for this choice. However, now that the feasibility of this pendulum with a friction hinge is tested on this single wave impact, different waves could be applied. Monochromatic waves causing repeated impacts on the current pendulum could be a perfect addition to this research. The current setup and model would then be a model for strain hardening as well. The vertical distance between the cylinder and the friction hinge is reduced after plastic deformation due to the first wave impact. Assuming that a wave only exerts a horizontal force, the moment on the plastic hinge of a second wave impact becomes smaller after this initial plastic deformation. When strain hardening occurs, it is more difficult to deform the material plastically when loaded a second time. The reduction in the applied moment simulates the behaviour of strain hardening appropriately.

3. This recommendation is a summary of adjustments to the experimental setup. The first one is based on the results of the angles of the pendulum. When the behaviour is analysed, horizontal parts in the graph were observed. The potentiometers introduce these horizontal parts due to their minimal resolution. This phenomenon requires the use of a fit function to obtain the derivatives of the signals, which introduces more inaccuracies. Since the angles of the top part of the pendulum are approximately 100 times smaller than the range of the sensor, the problem strikes most at these angles. Therefore, it is recommended to choose potentiometers that have a range of ten degrees if these experiments would be repeated.

   Another recommendation is based on the details of the friction mechanism. In this research standard rubber brakes of a bike are used as brake-blocks on the disc of the friction mechanism. These rubber blocks are slightly deformable, and after a while, a trace is left on the disc. In order to prevent or change this, other materials for the disc or the brake-blocks could be chosen. This change would cause the friction mechanism to be repeatable in the long term as well. The rubber brake-blocks fall into the organic category. In order to obtain different behaviour, another material from that category could be chosen, such as glass or Kevlar. When a more thorough change is desired, metal or ceramic materials could be used (Bridgestone, 2020).

4. An addition to the energy analysis done in this research would be a complete energy balance of the environment around the pendulum. This is not done in this research due to difficult to model phenomena related to breaking waves. However, this energy balance could give insight in other energy components that are not shown in this research. A starting point could be the research of Perlin et al. (2013) in which the implementation of an eddy viscosity model shows good results regarding energy dissipation in waves.

Bibliography

Agarana, M. C., Ajayi, O. O., and Emetere, M. E. (2017). Lagrangian-analytical modelling of damped quintuple pendulum system. In *Proceedings of the World Congress on Engineering and Computer Science*, volume 2, pages 771–776.

Bos, R. W. and Wellens, P. R. (2020). Fluid Structure Interaction Between a Pendulum and Monochromatic Waves. pages 1–8.

Bridgestone (2020). Ceramic vs. Metallic Brake Pads.

Bullock, G. N., Obhrai, C., Peregrine, D. H., and Bredmose, H. (2007). Violent breaking wave impacts. Part 1: Results from large-scale regular wave tests on vertical and sloping walls. *Coastal Engineering*, 54(8):602–617.

Campbell, J. C. and Vignjevic, R. (2012). Simulating structural response to water impact. *International Journal of Impact Engineering*, 49:1–10.

Chan, E. S. and Melville, W. K. (1988). Deep-Water Plunging Wave Pressures on a Vertical Plane. In *Proceedings of the Royal Society of London. Series A, Mathematical and Physical Sciences*, volume 417, pages 95–131.

Chang, K.-A., Chen, H.-C., Yu, K., Ruy, Y., Ariyarathne, K., and Mercier, R. (2017). TAP-571-Loads due to Extreme Wave Crests.

Curnier, A. (1984). A theory of friction. *International Journal of Solids and Structures*, 20(7):637–647.

Dalton, C. and Nash, J. M. (1976). Wave slam on horizontal members of an offshore platform. In *Eighth Annual Offshore Technology Conference*, pages 769–780.

Davidson, J. (2019). Oil Companies Were Not Held Accountable for 10.8 Million Gallons of Oil Spilled in Gulf of Mexico.

Davies, R. L. and Martin, J. G. (1990). Wave-Impact Loads on Large-Diameter Horizontal Cylinder Placed Above Still Water Level. In *Proceedings of the 22nd Annual Offshore Technology Conference*.

den Besten, H. (2019). Fluid-Structure Interaction in Marine Structures: Transient wave loading - fluid dynamics.

Goda, Y., Haranaka, S., and Kitahata, M. (1966). Study of impulsive breaking wave forces on piles. *Port and Harbour Technical Research Institute*.

Ha, Y. J., Kim, K. H., Nam, B. W., and Hong, S. Y. (2020). Experimental study of wave impact loads on circular cylinder by breaking waves. *Ocean Engineering*, 209.

Haley, J. F., Gibson, R., and Swan, C. (2014). An Experimental Investigation of Wave Impact Loads on a Slender Horizontal Cylinder. In *Proceedings of the ASME 2014 33rd International Conference on Ocean, Offshore and Arctic Engineering*, pages 1–11.

Hattori, M., Arami, A., and Yui, T. (1994). Wave impact pressure on vertical walls under breaking waves of various types. *Coastal Engineering*, 22:79–114.

Hofland, B., Kaminski, M. L., and Wolters, G. (2010). Large scale wave impacts on a vertical wall. *Coastal Engineering*.

Holthuijsen, L. H. (2007). *Waves in Oceanic and Coastal Waters*. Cambridge University Press, Cambridge.

Kamath, A., Alagan Chella, M., Bihs, H., and Arntsen, Ø. A. (2016). Breaking wave interaction with a vertical cylinder and the effect of breaker location. *Ocean Engineering*, 128:105–115.

Kotsur, O., Scheglov, G., and Leyland, P. (2014). Verification of modelling of fluid structure interaction (FSI) problems based on experimental research of bluff body oscillations in fluids. *29th Congress of the International Council of the Aeronautical Sciences, ICAS 2014*, (January).

Langtangen, H. P. and Linge, S. (2016). *Finite Difference Computing with PDEs - A Modern Software Approach*. Oslo.

Lubliner, J. (2008). Chapter 2: The Physics of Plasticity. In *Plasticity Theory*, pages 75–110. Dover Publications, Inc., New York.

Manjula, R., Sannasiraj, S. A., and Palanichamy, K. (2012). Deflection of slender cylindrical member under breaking wave impact. In *Proceedings of the Twenty-second (2012) International Offshore and Polar Engineering Conference*, volume 4, pages 859–863.

MechaniCalc (2020). Mechanical Properties of Materials.

Méhauté, B. (1976). *An Introduction to Hydrodynamics and Water Waves*. Springer Berlin Heidelberg, Berlin, Heidelberg.

Montanari, A. (2017). Mechanics of sea waves.

Morison, J., Johnson, J., and Schaaf, S. (1950). The Force Exerted by Surface Waves on Piles. *Petroleum Transactions*, 189:149–154.

Paik, J. K. (2018). *Ultimate Limit State Analysis and Design of Plated Structures*. John Wiley & Sons Ltd.

Peregrine, D. H. (2003). Water-Wave Impact on Walls. *Annual Review of Fluid Mechanics*, 35:23–43.

Peregrine, H., Bredmose, H., Bullock, G., Obhrai, C., Müller, G., and Wolters, G. (2005). Violent water wave impact on a wall. pages 155–159.

Perlin, M., Choi, W., and Tian, Z. (2013). Breaking Waves in Deep and Intermediate Waters. *Annual Review of Fluid Mechanics*, 45(1):115–145.

Prasad, S., Chan, E.-S., and Isaacson, M. (1994). Breaking Wave Impact on a Slender Horizontal Cylinder. In *Proceedings of the Fourth (1994) Offshore and Polar Engineering Conference*, volume III. The International Society of Offshore and Polar Engineers.

Sarpkaya, T. (1979). Wave impact loads on cylinders. *Society of Petroleum Engineers Journal*, pages 169–174.

Sarpkaya, T. (1986). Force on a circular cylinder in viscous oscillatory flow at low Keulegan-Carpenter numbers. *Journal of Fluid Mechanics*, 165:61–71.

Smith, S. W. (1999). Moving Average Filters. In *The Scientist and Engineer's Guide to Digital Signal Processing*, chapter 15, pages 277–284.

Top Fives (2018). Top 5 Massive Waves vs Oil Rigs - heavy seas!

Tsaousis, T. D. and Chatjigeorgiou, I. K. (2020). An Analytical Approach for the Two-Dimensional Plunging Breaking Wave Impact on a Vertical Wall with Air Entrapment. *Fluids*, 5(58).

Tsaousis, T. D., Papadopoulos, P. K., and Chatjigeorgiou, I. K. (2020). A semi-analytical solution for the three-dimensional Wagner steep wave impact on a vertical circular cylinder. *Applied Mathematical Modelling*, 77:902–921.

Vallery, H. and Schwab, A. L. (2018). *Advanced Dynamics*. Delft University of Technology, Delft.

van Loon, R. and van de Vosse, F. N. (2010). Special issue: Fluid-structure interaction in biomedical applications. *International Journal for Numerical Methods in Biomedical Engineering*, 26(3-4):273–275.

Vyzikas, T., Stagonas, D., Buldakov, E., and Greaves, D. (2018). The evolution of free and bound waves during dispersive focusing in a numerical and physical flume. *Coastal Engineering*, 132:95–109.

Wiegel, R. L. (1982). Forces Induced by Breakers on Piles. *Coastal Engineering*, pages 1699–1715.

Wienke, J. and Oumeraci, H. (2005). Breaking wave impact force on a vertical and inclined slender pile - Theoretical and large-scale model investigations. *Coastal Engineering*, 52(5):435–462.

Wienke, J., Sparboom, U., and Oumeraci, H. (2005). Theoretical formulae for wave slamming loads on slender circular cylinders and application for support structures of wind turbines. In *Proceedings of the Coastal Engineering Conference*, number 1, pages 4018–4026.

Wikipedia (2020). Stress-strain curve.

Wriggers, P. (2006). *Computational contact mechanics*. Springer, second edition.

Wu, C. H. and Yao, A. (2004). Laboratory measurements of limiting freak waves on currents. *Journal of Geophysical Research*, 109.

Yu, Z., Amdahl, J., Greco, M., and Xu, H. (2019a). Hydro-plastic response of beams and stiffened panels subjected to extreme water slamming at small impact angles, Part I: An analytical solution. *Marine Structures*, 65:53–74.

Yu, Z., Amdahl, J., Greco, M., and Xu, H. (2019b). Hydro-plastic response of beams and stiffened panels subjected to extreme water slamming at small impact angles, part II: Numerical verification and analysis. *Marine Structures*, 65:114–133.

Zhang, S., Yue, D. K. P., and Tanizawa, K. (1996). Simulation of plunging wave impact on a vertical wall. *Journal of Fluid Mechanics*, 327:221–254.

A

Drawings and pictures of experimental setup

In this appendix, the drawings and pictures of the three pendulum arrangements are shown in section A.1. Then, in section A.2, pictures of details of the pendulum and process are shown.

A.1. Overview of three arrangements

The overview of the three arrangements is given from long to short, so, therefore, the pendulum with L_1 = 1.25 m is shown in section A.1.1, the pendulum with L_1 = 0.95 m in section A.1.2 and the pendulum with L_1 = 0.65 m in section A.1.3.

A.1.1. Drawing and picture of the long pendulum

The schematic overview of the long pendulum is shown in figure A.1. Then, a picture of the pendulum connected to the towing carriage is shown in figure A.2.

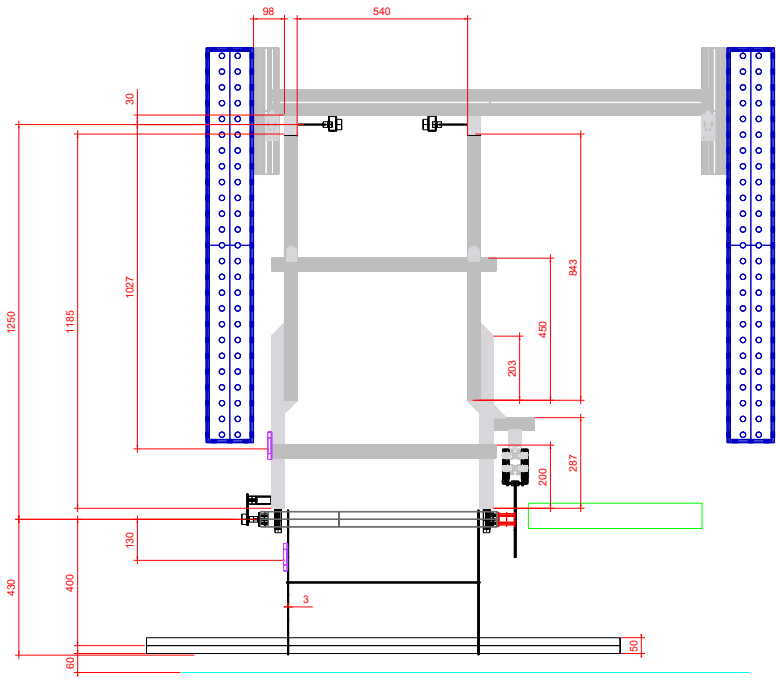

Figure A.1: Schematic overview of the long pendulum. In this arrangement, the length of the top part of the pendulum is 1.25 m, and the length of the bottom part is 0.4 m. *Drawing by Jasper den Ouden.*

Figure A.2: Picture of the long pendulum. In this arrangement, the length of the top part of the pendulum is 1.25 m, and the length of the bottom part is 0.4 m.

Figure A.3: Picture of the medium pendulum. In this arrangement, the length of the top part of the pendulum is 0.95 m, and the length of the bottom part is 0.4 m.

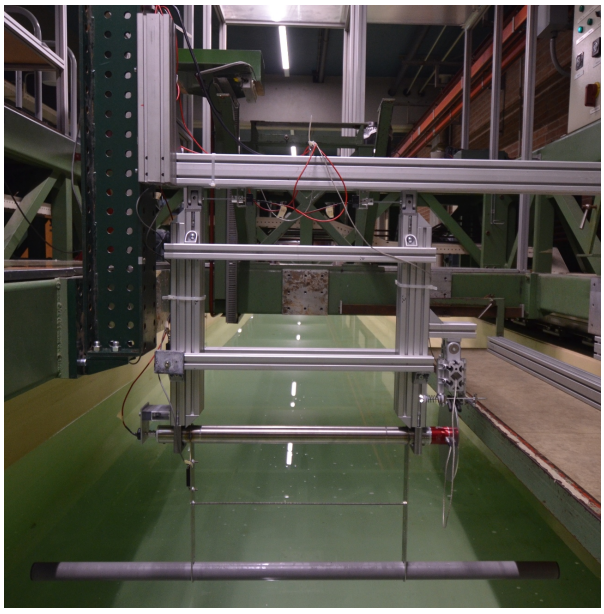

Figure A.4: Picture of the short pendulum. In this arrangement, the length of the top part of the pendulum is 0.65 m, and the length of the bottom part is 0.4 m.

A.1.2. Drawing and picture of the medium pendulum

The schematic overview of the medium pendulum is shown in figure A.5. A picture of the pendulum connected to the towing carriage is shown in figure A.3.

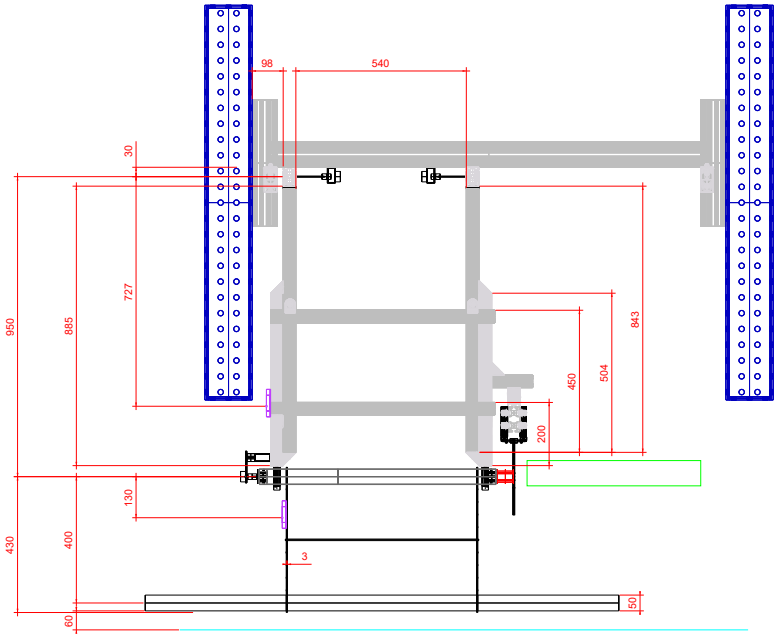

Figure A.5: Schematic overview of the medium pendulum. In this arrangement, the length of the top part of the pendulum is 0.95 m, and the length of the bottom part is 0.4 m. *Drawing by Jasper den Ouden.*

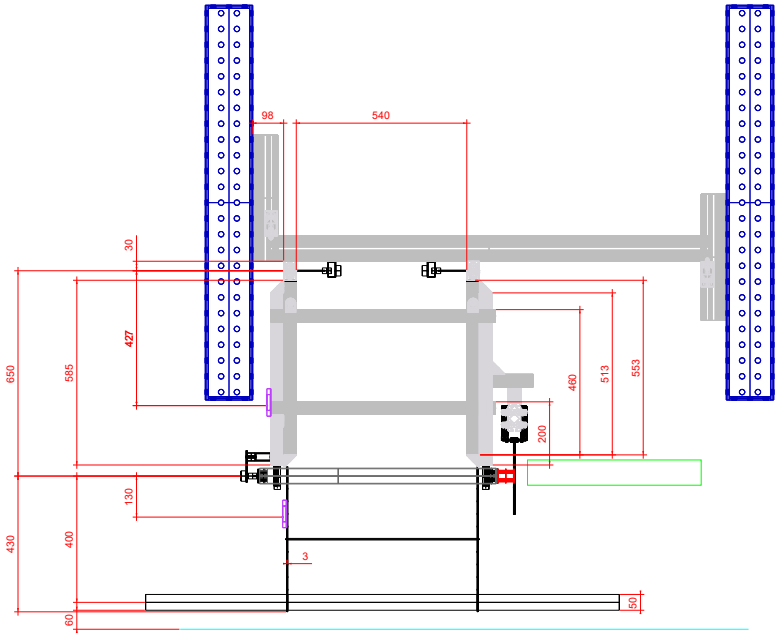

Figure A.6: Schematic overview of the short pendulum. In this arrangement, the length of the top part of the pendulum is 0.65 m, and the length of the bottom part is 0.4 m. *Drawing by Jasper den Ouden.*

A.1.3. Drawing and picture of the short pendulum

The schematic overview of the short pendulum is shown in figure A.6. A picture of the pendulum connected to the towing carriage is shown in figure A.4.

A.2. Details of pendulum and process

The connection of the three potentiometers is shown in figures A.7 (potentiometers 1 and 2) and A.8 (potentiometer 3). Next to this, a close up of the friction mechanism is shown in figure A.9. The red sensor is the torque sensor which is connected between the disc and the axis of the bottom hinge. In the friction mechanism, a hinge is incorporated to adjust for possible small horizontal deviations of the disc.

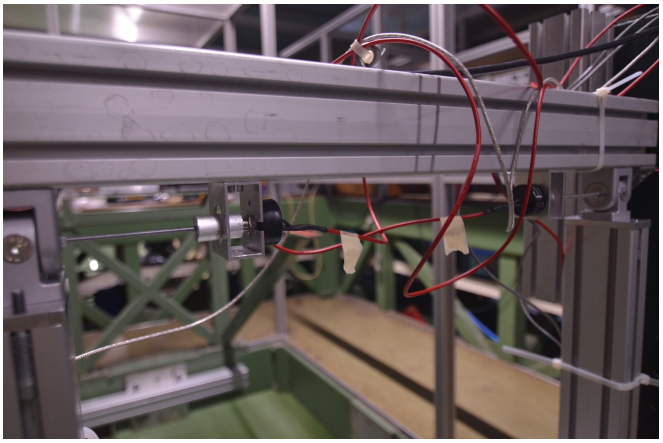

Figure A.7: Potentiometers 1 and 2 are connected to the top hinges in order to measure the angle of the top part of the pendulum.

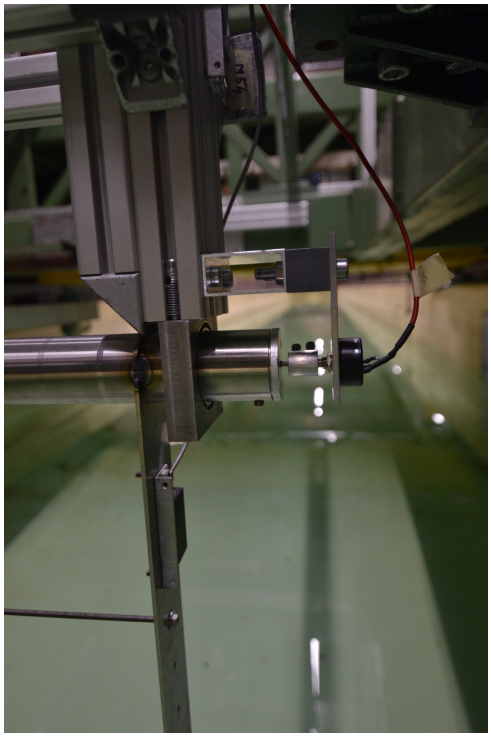

Figure A.8: Potentiometer 3 is connected to the axis between the top and bottom pendulum to measure the relative angle between the top and bottom pendulum.

Figure A.9: Close up of the friction mechanism. In the friction mechanism, a hinge is incorporated to adjust for possible small horizontal deviations of the disc.

Before starting the experiments, it is made sure that the pendulum is orientated vertical when it is unloaded. This orientation is checked using a laser with a spirit level included. This check is shown on the left of figure A.10. Next to this, the pendulum should be perpendicular to the towing tank. This orientation is examined using a large L-square, made of aluminium profiles, which is aligned with the rails of the towing tank. This L-square is shown on the right of figure A.10.

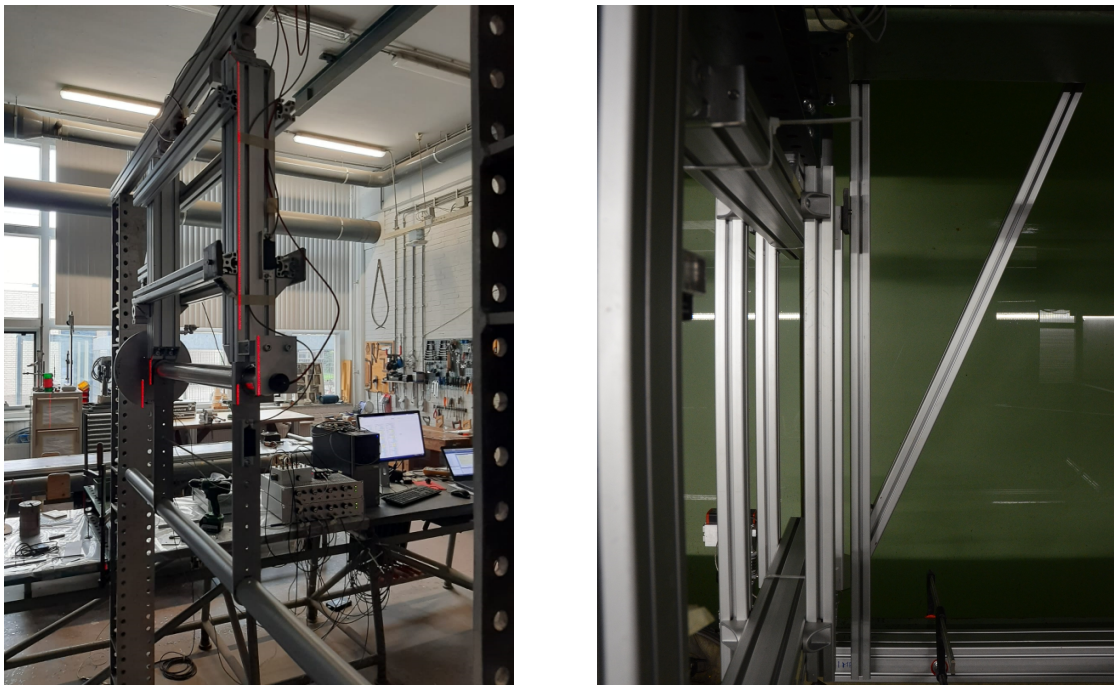

Figure A.10: The pendulum is orientated vertical when it is unloaded (left). This check is done using a laser with an included spirit level. The pendulum is perpendicular to the towing tank (right). This orientation is examined using a large L-square, made of aluminium profiles, which is aligned with the rails of the towing tank.

B

Detailed overview of results

In this appendix, all the results are summarised for each pendulum in each wave. The maximum values of the wave height, top angle of the pendulum and elastic, dissipated and total absorbed energy are given. For the relative angle between the top and bottom pendulum, the value after the pendulum has stopped oscillating is given. For each variable, the median, 25% and 75% quartiles and the minimum and maximum measured values are given, and in the last column, the value calculated by the model is given. First, the results of the long pendulum are shown in section B.1, then of the medium pendulum in section B.2 and of the short pendulum in section B.3.

B.1. Long pendulum L_1 = 1.25 m

The detailed results of the long pendulum in all three waves are shown in this section. In table B.1 the results of the wave focused at 28.380 m are shown, in table B.2 the results of the wave focused at 28.880 m and in table B.3 the results of the wave focused at 29.380 m.

Table B.1: The detailed results for the long pendulum in the wave focused at x_{focus} = 28.380 m. The median, 25% (Q1) and 75% (Q3) quartiles, and the minimum and maximum measured values are shown. The last column shows value calculated by the model. All these values are given for the maximum values of the wave height, top angle of the pendulum and elastic, dissipated and total absorbed energy and the final value of the relative angle.

	M_{aim} (Nm)	Minimum	Q1	Median	Q3	Maximum	Model	
η_{max}	0	127.679	129.651	135.733	137.550	137.620	136.382	mm
$\theta_{top,max}$	0	3.001	3.017	3.033	3.074	3.082	1.910	deg
$\theta_{rel,end}$	0	40.054	40.444	40.849	41.368	41.394	20.214	deg
$E_{el,max}$	0	1.416	1.446	1.484	1.515	1.519	0.417	J
$E_{diss,max}$	0	0.126	0.126	0.128	0.132	0.132	0.000	J
$E_{abs,max}$	0	1.443	1.473	1.512	1.544	1.548	0.417	J
η_{max}	2	134.449	134.730	139.257	130.554	142.462	136.382	mm
$\theta_{top,max}$	2	1.379	1.490	1.602	1.640	1.675	2.585	deg
$\theta_{rel,end}$	2	8.483	9.676	14.371	15.185	15.276	8.233	deg
$E_{el,max}$	2	0.315	0.322	0.373	0.380	0.381	0.353	J
$E_{diss,max}$	2	0.362	0.371	0.389	0.405	0.414	0.233	J
$E_{abs,max}$	2	0.624	0.632	0.732	0.747	0.754	0.586	J
η_{max}	3	131.805	132.951	139.478	128.519	140.537	136.382	mm
$\theta_{top,max}$	3	1.949	1.951	2.062	2.177	2.229	3.138	deg
$\theta_{rel,end}$	3	6.445	7.181	8.900	9.309	9.588	4.207	deg
$E_{el,max}$	3	0.298	0.303	0.318	0.348	0.353	0.422	J
$E_{diss,max}$	3	0.329	0.370	0.461	0.467	0.467	0.178	J
$E_{abs,max}$	3	0.574	0.637	0.744	0.786	0.798	0.600	J
η_{max}	4	132.739	132.910	147.158	135.111	154.528	136.382	mm
$\theta_{top,max}$	4	2.204	2.224	2.320	2.336	2.352	3.494	deg
$\theta_{rel,end}$	4	4.422	4.801	5.892	6.080	6.259	1.721	deg
$E_{el,max}$	4	0.292	0.306	0.322	0.322	0.323	0.489	J
$E_{diss,max}$	4	0.279	0.315	0.354	0.366	0.368	0.097	J
$E_{abs,max}$	4	0.565	0.608	0.658	0.676	0.677	0.586	J
η_{max}	5	130.379	135.028	140.696	135.638	147.193	136.382	mm
$\theta_{top,max}$	5	2.208	2.260	2.328	2.387	2.430	3.630	deg
$\theta_{rel,end}$	5	3.293	3.398	4.234	4.604	4.784	0.752	deg
$E_{el,max}$	5	0.299	0.299	0.314	0.322	0.322	0.519	J
$E_{diss,max}$	5	0.235	0.249	0.273	0.307	0.341	0.053	J
$E_{abs,max}$	5	0.550	0.552	0.557	0.595	0.629	0.572	J
η_{max}	11	129.261	132.198	139.773	129.765	139.930	136.382	mm
$\theta_{top,max}$	11	3.071	3.100	3.214	3.416	3.596	3.747	deg
$\theta_{rel,end}$	11	-0.002	0.000	0.004	0.089	0.174	0.000	deg
$E_{el,max}$	11	0.438	0.440	0.460	0.515	0.564	0.547	J
$E_{diss,max}$	11	0.000	0.001	0.006	0.017	0.018	0.000	J
$E_{abs,max}$	11	0.456	0.457	0.466	0.516	0.565	0.547	J

Table B.2: The detailed results for the long pendulum in the wave focused at x_{focus} = 28.880 m. The median, 25% (Q1) and 75% (Q3) quartiles, and the minimum and maximum measured values are shown. The last column shows value calculated by the model. All these values are given for the maximum values of the wave height, top angle of the pendulum and elastic, dissipated and total absorbed energy and the final value of the relative angle.

	M_{aim} (Nm)	Minimum	Q1	Median	Q3	Maximum	Model	
η_{max}	0	166.382	166.688	171.155	173.032	173.354	138.415	mm
$\theta_{top,max}$	0	2.076	2.083	2.119	2.214	2.309	1.971	deg
$\theta_{rel,end}$	0	31.772	31.775	32.027	33.167	33.657	20.909	deg
$E_{el,max}$	0	0.877	0.878	0.894	0.956	0.986	0.446	J
$E_{diss,max}$	0	0.090	0.092	0.097	0.104	0.105	0.000	J
$E_{abs,max}$	0	0.893	0.895	0.911	0.975	1.004	0.446	J
η_{max}	2	121.628	143.308	168.100	172.163	173.985	138.415	mm
$\theta_{top,max}$	2	1.051	1.146	1.244	1.273	1.296	2.572	deg
$\theta_{rel,end}$	2	8.291	9.674	11.788	12.067	12.342	9.083	deg
$E_{el,max}$	2	0.325	0.337	0.357	0.365	0.367	0.368	J
$E_{diss,max}$	2	0.520	0.524	0.548	0.564	0.566	0.257	J
$E_{abs,max}$	2	0.736	0.739	0.751	0.763	0.766	0.625	J
η_{max}	3	119.444	144.060	173.080	169.124	175.076	138.415	mm
$\theta_{top,max}$	3	1.332	1.370	1.594	1.603	1.610	3.114	deg
$\theta_{rel,end}$	3	5.717	6.642	7.736	8.233	8.542	5.044	deg
$E_{el,max}$	3	0.271	0.274	0.286	0.297	0.304	0.429	J
$E_{diss,max}$	3	0.449	0.468	0.503	0.512	0.516	0.214	J
$E_{abs,max}$	3	0.631	0.650	0.682	0.692	0.697	0.643	J
η_{max}	4	105.269	135.472	170.978	171.078	171.600	138.415	mm
$\theta_{top,max}$	4	1.604	1.615	1.688	1.848	1.932	3.494	deg
$\theta_{rel,end}$	4	3.681	4.512	5.894	6.360	6.819	2.343	deg
$E_{el,max}$	4	0.261	0.263	0.266	0.291	0.315	0.498	J
$E_{diss,max}$	4	0.295	0.351	0.444	0.466	0.484	0.132	J
$E_{abs,max}$	4	0.553	0.579	0.645	0.662	0.674	0.630	J
η_{max}	5	140.034	149.482	166.068	155.115	168.305	138.415	mm
$\theta_{top,max}$	5	1.868	1.909	2.002	2.161	2.204	3.676	deg
$\theta_{rel,end}$	5	2.578	2.655	2.952	4.041	4.787	1.067	deg
$E_{el,max}$	5	0.299	0.301	0.304	0.310	0.312	0.537	J
$E_{diss,max}$	5	0.202	0.207	0.218	0.327	0.387	0.075	J
$E_{abs,max}$	5	0.487	0.491	0.500	0.556	0.607	0.613	J
η_{max}	11	156.646	158.671	163.387	142.873	164.509	138.415	mm
$\theta_{top,max}$	11	2.687	2.762	2.918	2.921	2.922	3.839	deg
$\theta_{rel,end}$	11	-0.002	-0.001	-0.000	0.001	0.002	0.000	deg
$E_{el,max}$	11	0.401	0.403	0.417	0.424	0.424	0.576	J
$E_{diss,max}$	11	0.007	0.011	0.018	0.024	0.028	0.000	J
$E_{abs,max}$	11	0.409	0.418	0.431	0.438	0.442	0.576	J

Table B.3: The detailed results for the long pendulum in the wave focused at x_{focus} = 29.380 m. The median, 25% (Q1) and 75% (Q3) quartiles, and the minimum and maximum measured values are shown. The last column shows value calculated by the model. All these values are given for the maximum values of the wave height, top angle of the pendulum and elastic, dissipated and total absorbed energy and the final value of the relative angle.

	M_{aim} (Nm)	Minimum	Q1	Median	Q3	Maximum	Model	
η_{max}	0	158.602	162.119	165.952	168.093	169.918	132.039	mm
$\theta_{top,max}$	0	2.300	2.303	2.308	2.312	2.314	1.802	deg
$\theta_{rel,end}$	0	34.359	34.438	34.668	34.846	34.871	19.297	deg
$E_{el,max}$	0	1.020	1.026	1.041	1.051	1.053	0.377	J
$E_{diss,max}$	0	0.110	0.111	0.115	0.117	0.118	0.000	J
$E_{abs,max}$	0	1.039	1.045	1.060	1.071	1.071	0.377	J
η_{max}	2	158.396	158.559	159.514	160.953	161.599	132.039	mm
$\theta_{top,max}$	2	1.248	1.249	1.251	1.279	1.308	2.376	deg
$\theta_{rel,end}$	2	14.355	14.545	14.825	15.370	15.825	8.084	deg
$E_{el,max}$	2	0.415	0.417	0.423	0.440	0.455	0.310	J
$E_{diss,max}$	2	0.653	0.655	0.659	0.670	0.679	0.229	J
$E_{abs,max}$	2	0.944	0.965	0.987	0.990	0.993	0.539	J
η_{max}	3	158.270	160.137	163.242	164.506	164.534	132.039	mm
$\theta_{top,max}$	3	1.409	1.409	1.439	1.468	1.468	2.866	deg
$\theta_{rel,end}$	3	11.794	11.885	12.148	12.515	12.708	4.423	deg
$E_{el,max}$	3	0.351	0.354	0.358	0.363	0.366	0.362	J
$E_{diss,max}$	3	0.582	0.583	0.591	0.607	0.616	0.188	J
$E_{abs,max}$	3	0.853	0.853	0.859	0.870	0.876	0.550	J
η_{max}	4	158.414	159.035	160.895	162.214	162.294	132.039	mm
$\theta_{top,max}$	4	1.768	1.787	1.827	1.865	1.883	3.200	deg
$\theta_{rel,end}$	4	9.026	9.119	9.214	9.305	9.394	2.051	deg
$E_{el,max}$	4	0.309	0.313	0.325	0.345	0.358	0.418	J
$E_{diss,max}$	4	0.542	0.544	0.550	0.562	0.572	0.116	J
$E_{abs,max}$	4	0.830	0.833	0.836	0.847	0.856	0.534	J
η_{max}	5	157.349	159.308	161.871	162.901	163.326	132.039	mm
$\theta_{top,max}$	5	1.783	1.840	1.923	1.950	1.950	3.356	deg
$\theta_{rel,end}$	5	6.079	6.169	6.449	6.803	6.968	0.966	deg
$E_{el,max}$	5	0.297	0.298	0.304	0.308	0.308	0.450	J
$E_{diss,max}$	5	0.437	0.439	0.448	0.460	0.465	0.068	J
$E_{abs,max}$	5	0.696	0.698	0.704	0.723	0.737	0.518	J
η_{max}	6	162.931	163.954	165.519	166.162	166.263	132.039	mm
$\theta_{top,max}$	6	1.961	1.975	2.022	2.121	2.186	3.421	deg
$\theta_{rel,end}$	6	3.507	3.870	4.699	5.252	5.339	0.506	deg
$E_{el,max}$	6	0.298	0.304	0.310	0.313	0.316	0.464	J
$E_{diss,max}$	6	0.309	0.334	0.384	0.413	0.417	0.043	J
$E_{abs,max}$	6	0.608	0.626	0.668	0.701	0.711	0.506	J
η_{max}	11	154.025	154.566	155.765	157.455	158.487	132.039	mm
$\theta_{top,max}$	11	2.562	2.562	2.563	2.573	2.584	3.510	deg
$\theta_{rel,end}$	11	-0.002	0.000	0.004	0.096	0.186	0.000	deg
$E_{el,max}$	11	0.392	0.398	0.407	0.412	0.412	0.484	J
$E_{diss,max}$	11	0.016	0.021	0.028	0.035	0.040	0.000	J
$E_{abs,max}$	11	0.423	0.425	0.427	0.430	0.431	0.484	J

B.2. Medium pendulum L_1 = 0.95 m

The detailed results of the medium pendulum in all three waves are shown in this section. In table B.4 the results of the wave focused at 28.380 m are shown, in table B.5 the results of the wave focused at 28.880 m and in table B.6 the results of the wave focused at 29.380 m.

Table B.4: The detailed results for the medium pendulum in the wave focused at x_{focus} = 28.380 m. The median, 25% (Q1) and 75% (Q3) quartiles, and the minimum and maximum measured values are shown. The last column shows value calculated by the model. All these values are given for the maximum values of the wave height, top angle of the pendulum and elastic, dissipated and total absorbed energy and the final value of the relative angle.

	M_{aim} (Nm)	Minimum	Q1	Median	Q3	Maximum	Model	
η_{max}	0	131.816	144.960	150.241	150.505	162.215	136.382	mm
$\theta_{top,max}$	0	3.728	3.732	3.867	4.000	4.001	2.445	deg
$\theta_{rel,end}$	0	40.107	40.109	41.209	41.691	42.637	20.197	deg
$E_{el,max}$	0	1.413	1.428	1.499	1.550	1.607	0.417	J
$E_{diss,max}$	0	0.089	0.091	0.094	0.101	0.118	0.000	J
$E_{abs,max}$	0	1.434	1.449	1.521	1.576	1.630	0.417	J
η_{max}	2	129.543	140.733	144.110	152.100	148.718	136.382	mm
$\theta_{top,max}$	2	1.774	1.865	1.868	1.869	1.977	2.761	deg
$\theta_{rel,end}$	2	11.781	11.787	14.179	15.276	15.460	7.971	deg
$E_{el,max}$	2	0.320	0.327	0.378	0.403	0.433	0.365	J
$E_{diss,max}$	2	0.385	0.428	0.483	0.488	0.490	0.225	J
$E_{abs,max}$	2	0.683	0.741	0.863	0.880	0.910	0.590	J
η_{max}	3	109.463	116.637	143.222	140.388	145.318	136.382	mm
$\theta_{top,max}$	3	2.213	2.216	2.224	2.301	2.317	3.365	deg
$\theta_{rel,end}$	3	7.788	8.103	8.108	8.285	8.287	3.818	deg
$E_{el,max}$	3	0.313	0.317	0.326	0.329	0.333	0.446	J
$E_{diss,max}$	3	0.381	0.395	0.396	0.396	0.406	0.162	J
$E_{abs,max}$	3	0.678	0.685	0.702	0.711	0.721	0.608	J
η_{max}	4	124.168	136.837	141.656	148.264	153.212	136.382	mm
$\theta_{top,max}$	4	2.260	2.378	2.439	2.463	2.577	3.763	deg
$\theta_{rel,end}$	4	3.707	4.767	5.529	6.633	7.006	1.452	deg
$E_{el,max}$	4	0.302	0.305	0.312	0.338	0.341	0.517	J
$E_{diss,max}$	4	0.240	0.274	0.306	0.375	0.400	0.082	J
$E_{abs,max}$	4	0.553	0.566	0.601	0.697	0.718	0.599	J
η_{max}	5	122.812	131.285	140.104	157.371	151.728	136.382	mm
$\theta_{top,max}$	5	2.478	2.486	2.578	2.585	2.737	3.915	deg
$\theta_{rel,end}$	5	2.953	3.690	4.049	4.056	4.416	0.599	deg
$E_{el,max}$	5	0.327	0.336	0.341	0.345	0.352	0.545	J
$E_{diss,max}$	5	0.209	0.243	0.257	0.267	0.282	0.042	J
$E_{abs,max}$	5	0.554	0.578	0.591	0.602	0.614	0.588	J
η_{max}	11	108.965	116.737	135.908	133.120	140.572	136.382	mm
$\theta_{top,max}$	11	3.103	3.204	3.249	3.292	3.397	4.069	deg
$\theta_{rel,end}$	11	-0.003	-0.003	0.000	0.001	0.003	0.000	deg
$E_{el,max}$	11	0.406	0.431	0.437	0.442	0.448	0.570	J
$E_{diss,max}$	11	0.009	0.010	0.021	0.030	0.030	0.000	J
$E_{abs,max}$	11	0.439	0.447	0.455	0.460	0.471	0.570	J

Table B.5: The detailed results for the medium pendulum in the wave focused at x_{focus} = 28.880 m. The median, 25% (Q1) and 75% (Q3) quartiles, and the minimum and maximum measured values are shown. The last column shows value calculated by the model. All these values are given for the maximum values of the wave height, top angle of the pendulum and elastic, dissipated and total absorbed energy and the final value of the relative angle.

	M_{aim} (Nm)	Minimum	Q1	Median	Q3	Maximum	Model	
η_{max}	0	157.774	170.373	174.516	175.263	178.038	138.415	mm
$\theta_{top,max}$	0	2.578	2.580	2.707	2.800	3.330	2.675	deg
$\theta_{rel,end}$	0	32.361	32.387	33.037	33.353	37.559	20.891	deg
$E_{el,max}$	0	0.897	0.901	0.945	0.966	1.281	0.446	J
$E_{diss,max}$	0	0.055	0.056	0.058	0.070	0.082	0.000	J
$E_{abs,max}$	0	0.911	0.915	0.963	0.987	1.303	0.446	J
η_{max}	2	155.168	159.229	163.094	171.365	167.813	138.415	mm
$\theta_{top,max}$	2	1.510	1.513	1.520	1.522	1.667	2.977	deg
$\theta_{rel,end}$	2	10.490	11.215	11.783	12.534	14.161	8.807	deg
$E_{el,max}$	2	0.296	0.300	0.349	0.353	0.365	0.379	J
$E_{diss,max}$	2	0.498	0.515	0.528	0.549	0.566	0.249	J
$E_{abs,max}$	2	0.740	0.756	0.804	0.842	0.877	0.628	J
η_{max}	3	157.801	158.082	167.583	171.975	172.273	138.415	mm
$\theta_{top,max}$	3	1.667	1.690	1.722	1.782	2.016	3.650	deg
$\theta_{rel,end}$	3	7.736	8.476	8.844	9.222	10.123	4.648	deg
$E_{el,max}$	3	0.239	0.245	0.285	0.301	0.311	0.452	J
$E_{diss,max}$	3	0.400	0.426	0.445	0.471	0.483	0.197	J
$E_{abs,max}$	3	0.643	0.670	0.706	0.714	0.721	0.649	J
η_{max}	4	161.584	171.221	173.073	174.192	175.464	138.415	mm
$\theta_{top,max}$	4	1.988	2.017	2.035	2.050	2.379	4.108	deg
$\theta_{rel,end}$	4	5.177	6.633	7.182	7.373	8.101	1.961	deg
$E_{el,max}$	4	0.268	0.270	0.290	0.303	0.337	0.530	J
$E_{diss,max}$	4	0.334	0.374	0.388	0.408	0.428	0.111	J
$E_{abs,max}$	4	0.636	0.636	0.648	0.665	0.665	0.641	J
η_{max}	5	145.094	154.816	169.944	173.816	175.489	138.415	mm
$\theta_{top,max}$	5	2.298	2.454	2.524	2.651	2.664	4.289	deg
$\theta_{rel,end}$	5	2.393	2.584	3.315	4.057	4.623	0.866	deg
$E_{el,max}$	5	0.321	0.321	0.342	0.355	0.360	0.566	J
$E_{diss,max}$	5	0.179	0.187	0.238	0.314	0.316	0.061	J
$E_{abs,max}$	5	0.519	0.532	0.569	0.626	0.643	0.627	J
η_{max}	11	140.999	158.405	169.526	173.816	173.233	138.415	mm
$\theta_{top,max}$	11	2.857	3.044	3.091	3.162	3.176	4.449	deg
$\theta_{rel,end}$	11	-0.001	0.001	0.002	0.004	0.009	0.000	deg
$E_{el,max}$	11	0.433	0.437	0.437	0.441	0.452	0.601	J
$E_{diss,max}$	11	0.013	0.017	0.017	0.017	0.018	0.000	J
$E_{abs,max}$	11	0.446	0.453	0.454	0.457	0.469	0.601	J

Table B.6: The detailed results for the medium pendulum in the wave focused at x_{focus} = 29.380 m. The median, 25% (Q1) and 75% (Q3) quartiles, and the minimum and maximum measured values are shown. The last column shows value calculated by the model. All these values are given for the maximum values of the wave height, top angle of the pendulum and elastic, dissipated and total absorbed energy and the final value of the relative angle.

	M_{aim} (Nm)	Minimum	Q1	Median	Q3	Maximum	Model	
η_{max}	0	159.599	165.085	166.663	167.644	171.926	132.039	mm
$\theta_{top,max}$	0	2.930	2.932	2.943	3.090	3.109	2.445	deg
$\theta_{rel,end}$	0	34.908	35.695	35.702	36.246	36.438	19.278	deg
$E_{el,max}$	0	1.040	1.082	1.093	1.153	1.158	0.377	J
$E_{diss,max}$	0	0.068	0.070	0.073	0.075	0.079	0.000	J
$E_{abs,max}$	0	1.059	1.102	1.114	1.172	1.182	0.377	J
η_{max}	2	157.693	158.565	161.773	163.064	166.212	132.039	mm
$\theta_{top,max}$	2	1.514	1.523	1.601	1.608	1.651	2.761	deg
$\theta_{rel,end}$	2	16.922	16.937	18.215	18.770	19.432	7.798	deg
$E_{el,max}$	2	0.485	0.488	0.507	0.524	0.570	0.320	J
$E_{diss,max}$	2	0.693	0.704	0.707	0.721	0.725	0.220	J
$E_{abs,max}$	2	1.128	1.130	1.166	1.190	1.194	0.541	J
η_{max}	3	159.413	161.093	164.998	166.096	166.132	132.039	mm
$\theta_{top,max}$	3	1.666	1.749	1.866	1.869	2.024	3.365	deg
$\theta_{rel,end}$	3	13.630	13.990	14.164	14.543	14.724	4.047	deg
$E_{el,max}$	3	0.410	0.413	0.432	0.440	0.444	0.382	J
$E_{diss,max}$	3	0.628	0.633	0.649	0.675	0.694	0.172	J
$E_{abs,max}$	3	0.981	0.981	1.015	1.066	1.104	0.554	J
η_{max}	4	156.765	159.185	165.037	166.750	167.853	132.039	mm
$\theta_{top,max}$	4	1.866	1.872	2.021	2.026	2.066	3.763	deg
$\theta_{rel,end}$	4	11.044	11.233	12.336	12.526	12.546	1.694	deg
$E_{el,max}$	4	0.364	0.367	0.398	0.410	0.433	0.444	J
$E_{diss,max}$	4	0.568	0.576	0.611	0.629	0.637	0.096	J
$E_{abs,max}$	4	0.887	0.903	0.955	0.995	1.039	0.540	J
η_{max}	5	160.655	161.841	165.084	165.805	167.039	132.039	mm
$\theta_{top,max}$	5	2.072	2.130	2.172	2.217	2.231	3.915	deg
$\theta_{rel,end}$	5	7.033	7.369	7.740	8.038	8.091	0.801	deg
$E_{el,max}$	5	0.344	0.345	0.353	0.357	0.362	0.472	J
$E_{diss,max}$	5	0.452	0.478	0.508	0.513	0.519	0.057	J
$E_{abs,max}$	5	0.777	0.802	0.844	0.846	0.859	0.529	J
η_{max}	6	160.638	162.866	166.792	168.845	171.474	132.039	mm
$\theta_{top,max}$	6	2.448	2.478	2.536	2.578	3.002	3.981	deg
$\theta_{rel,end}$	6	4.426	5.530	6.077	6.261	6.374	0.401	deg
$E_{el,max}$	6	0.364	0.366	0.381	0.398	0.463	0.485	J
$E_{diss,max}$	6	0.427	0.436	0.454	0.459	0.494	0.034	J
$E_{abs,max}$	6	0.793	0.811	0.837	0.861	0.881	0.519	J
η_{max}	11	156.327	164.238	165.287	165.565	165.727	132.039	mm
$\theta_{top,max}$	11	3.108	3.136	3.157	3.202	3.205	4.069	deg
$\theta_{rel,end}$	11	-0.002	-0.001	-0.000	0.002	0.003	0.000	deg
$E_{el,max}$	11	0.531	0.531	0.538	0.542	0.553	0.503	J
$E_{diss,max}$	11	0.008	0.008	0.009	0.009	0.009	0.000	J
$E_{abs,max}$	11	0.540	0.540	0.546	0.552	0.562	0.503	J

B.3. Short pendulum L_1 = 0.65 m

The detailed results of the short pendulum in all three waves are shown in this section. In table B.7 the results of the wave focused at 28.380 m are shown, in table B.8 the results of the wave focused at 28.880 m and in table B.9 the results of the wave focused at 29.380 m.

Table B.7: The detailed results for the short pendulum in the wave focused at x_{focus} = 28.380 m. The median, 25% (Q1) and 75% (Q3) quartiles, and the minimum and maximum measured values are shown. The last column shows value calculated by the model. All these values are given for the maximum values of the wave height, top angle of the pendulum and elastic, dissipated and total absorbed energy and the final value of the relative angle.

	M_{aim} (Nm)	Minimum	Q1	Median	Q3	Maximum	Model	
η_{max}	0	143.895	150.238	158.401	162.425	166.943	136.382	mm
$\theta_{top,max}$	0	5.606	5.625	5.892	6.693	6.798	4.396	deg
$\theta_{rel,end}$	0	36.289	36.327	36.832	40.356	41.387	19.446	deg
$E_{el,max}$	0	1.157	1.163	1.209	1.493	1.523	0.417	J
$E_{diss,max}$	0	0.044	0.045	0.046	0.057	0.058	0.000	J
$E_{abs,max}$	0	1.166	1.176	1.221	1.503	1.534	0.417	J
η_{max}	1	134.370	142.320	147.229	149.214	150.963	136.382	mm
$\theta_{top,max}$	1	2.064	2.259	2.304	2.314	2.845	3.142	deg
$\theta_{rel,end}$	1	13.071	14.181	16.110	18.403	19.141	6.320	deg
$E_{el,max}$	1	0.357	0.389	0.417	0.472	0.511	0.353	J
$E_{diss,max}$	1	0.293	0.335	0.344	0.351	0.351	0.089	J
$E_{abs,max}$	1	0.614	0.729	0.758	0.822	0.862	0.521	J
η_{max}	2	130.255	137.755	147.094	151.746	155.397	136.382	mm
$\theta_{top,max}$	2	2.744	2.945	3.141	3.498	3.820	4.564	deg
$\theta_{rel,end}$	2	6.625	7.373	9.947	11.497	14.009	5.443	deg
$E_{el,max}$	2	0.308	0.326	0.394	0.454	0.477	0.433	J
$E_{diss,max}$	2	0.259	0.263	0.328	0.404	0.477	0.154	J
$E_{abs,max}$	2	0.559	0.575	0.714	0.863	0.924	0.587	J
η_{max}	3	117.900	137.564	148.160	151.430	154.414	136.382	mm
$\theta_{top,max}$	3	3.722	3.751	3.798	3.972	4.197	5.499	deg
$\theta_{rel,end}$	3	4.420	4.426	4.881	6.540	8.838	1.399	deg
$E_{el,max}$	3	0.356	0.364	0.396	0.438	0.456	0.547	J
$E_{diss,max}$	3	0.201	0.210	0.220	0.305	0.400	0.059	J
$E_{abs,max}$	3	0.563	0.563	0.613	0.754	0.828	0.606	J
η_{max}	4	131.405	134.799	146.654	150.832	150.976	136.382	mm
$\theta_{top,max}$	4	4.126	4.208	4.212	4.351	4.363	5.722	deg
$\theta_{rel,end}$	4	1.828	2.398	2.862	3.321	4.810	0.396	deg
$E_{el,max}$	4	0.390	0.413	0.438	0.455	0.459	0.580	J
$E_{diss,max}$	4	0.103	0.140	0.175	0.194	0.266	0.022	J
$E_{abs,max}$	4	0.529	0.552	0.593	0.646	0.722	0.602	J
η_{max}	5	125.685	130.451	142.279	142.730	144.749	136.382	mm
$\theta_{top,max}$	5	4.462	4.565	4.608	4.671	4.697	5.794	deg
$\theta_{rel,end}$	5	0.737	0.738	1.651	3.099	4.241	0.099	deg
$E_{el,max}$	5	0.449	0.453	0.473	0.480	0.500	0.591	J
$E_{diss,max}$	5	0.055	0.063	0.125	0.201	0.270	0.007	J
$E_{abs,max}$	5	0.508	0.512	0.597	0.679	0.768	0.598	J
η_{max}	11	124.142	130.024	139.972	140.407	144.243	136.382	mm
$\theta_{top,max}$	11	4.361	4.741	4.873	5.039	5.358	5.827	deg
$\theta_{rel,end}$	11	-0.003	-0.002	0.006	0.171	0.174	0.000	deg
$E_{el,max}$	11	0.475	0.481	0.493	0.513	0.570	0.597	J
$E_{diss,max}$	11	-0.000	-0.000	0.006	0.014	0.017	0.000	J
$E_{abs,max}$	11	0.481	0.489	0.504	0.519	0.570	0.597	J

Table B.8: The detailed results for the short pendulum in the wave focused at x_{focus} = 28.880 m. The median, 25% (Q1) and 75% (Q3) quartiles, and the minimum and maximum measured values are shown. The last column shows value calculated by the model. All these values are given for the maximum values of the wave height, top angle of the pendulum and elastic, dissipated and total absorbed energy and the final value of the relative angle.

	M_{aim} (Nm)	Minimum	Q1	Median	Q3	Maximum	Model	
η_{max}	0	148.245	164.709	168.116	170.958	170.981	138.415	mm
$\theta_{top,max}$	0	4.662	4.709	4.728	4.734	6.494	4.540	deg
$\theta_{rel,end}$	0	30.876	31.254	31.671	31.675	36.728	20.114	deg
$E_{el,max}$	0	0.852	0.854	0.863	0.881	1.343	0.445	J
$E_{diss,max}$	0	0.034	0.035	0.035	0.035	0.052	0.000	J
$E_{abs,max}$	0	0.864	0.867	0.875	0.892	1.354	0.445	J
η_{max}	1	171.150	171.177	172.664	173.856	174.782	138.415	mm
$\theta_{top,max}$	1	1.523	1.776	1.818	1.854	1.977	3.171	deg
$\theta_{rel,end}$	1	11.603	12.528	13.083	15.473	16.181	6.526	deg
$E_{el,max}$	1	0.378	0.396	0.408	0.411	0.437	0.376	J
$E_{diss,max}$	1	0.344	0.357	0.389	0.395	0.399	0.092	J
$E_{abs,max}$	1	0.663	0.666	0.668	0.683	0.717	0.554	J
η_{max}	2	144.860	160.032	169.618	175.614	176.232	138.415	mm
$\theta_{top,max}$	2	2.486	2.492	2.541	2.592	2.835	4.554	deg
$\theta_{rel,end}$	2	5.924	7.746	8.154	8.475	13.075	6.260	deg
$E_{el,max}$	2	0.315	0.318	0.351	0.357	0.386	0.446	J
$E_{diss,max}$	2	0.343	0.369	0.392	0.411	0.485	0.177	J
$E_{abs,max}$	2	0.603	0.614	0.629	0.651	0.827	0.623	J
η_{max}	3	126.390	158.431	169.107	169.689	177.188	138.415	mm
$\theta_{top,max}$	3	2.900	3.056	3.147	3.189	3.221	5.548	deg
$\theta_{rel,end}$	3	3.495	4.432	5.145	5.166	6.264	1.925	deg
$E_{el,max}$	3	0.318	0.348	0.361	0.362	0.392	0.563	J
$E_{diss,max}$	3	0.214	0.245	0.267	0.286	0.290	0.082	J
$E_{abs,max}$	3	0.568	0.592	0.593	0.594	0.606	0.644	J
η_{max}	4	150.996	162.017	168.240	171.102	177.000	138.415	mm
$\theta_{top,max}$	4	3.350	3.501	3.579	3.680	3.815	5.843	deg
$\theta_{rel,end}$	4	1.844	1.850	2.489	2.938	5.160	0.600	deg
$E_{el,max}$	4	0.366	0.411	0.419	0.430	0.437	0.607	J
$E_{diss,max}$	4	0.117	0.131	0.159	0.169	0.304	0.034	J
$E_{abs,max}$	4	0.551	0.554	0.566	0.580	0.660	0.641	J
η_{max}	5	147.674	153.645	171.121	173.396	177.099	138.415	mm
$\theta_{top,max}$	5	3.642	3.649	3.762	3.843	3.864	5.935	deg
$\theta_{rel,end}$	5	0.741	1.110	1.660	2.036	3.138	0.193	deg
$E_{el,max}$	5	0.398	0.432	0.433	0.447	0.452	0.621	J
$E_{diss,max}$	5	0.082	0.094	0.123	0.149	0.217	0.014	J
$E_{abs,max}$	5	0.527	0.538	0.549	0.571	0.606	0.635	J
η_{max}	11	140.732	143.605	167.759	168.971	172.716	138.415	mm
$\theta_{top,max}$	11	3.848	3.943	3.993	4.120	4.122	5.996	deg
$\theta_{rel,end}$	11	-0.006	-0.002	-0.000	0.002	0.005	0.000	deg
$E_{el,max}$	11	0.461	0.462	0.469	0.475	0.492	0.632	J
$E_{diss,max}$	11	0.000	0.008	0.013	0.024	0.028	0.000	J
$E_{abs,max}$	11	0.462	0.472	0.482	0.486	0.514	0.632	J

Table B.9: The detailed results for the short pendulum in the wave focused at x_{focus} = 29.380 m. The median, 25% (Q1) and 75% (Q3) quartiles, and the minimum and maximum measured values are shown. The last column shows value calculated by the model. All these values are given for the maximum values of the wave height, top angle of the pendulum and elastic, dissipated and total absorbed energy and the final value of the relative angle.

	M_{aim} (Nm)	Minimum	Q1	Median	Q3	Maximum	Model	
η_{max}	0	165.413	167.327	168.232	170.362	170.438	132.039	mm
$\theta_{top,max}$	0	5.334	5.389	5.413	5.451	5.618	4.159	deg
$\theta_{rel,end}$	0	33.749	33.819	34.062	34.607	34.613	18.584	deg
$E_{el,max}$	0	0.978	0.980	1.003	1.036	1.041	0.377	J
$E_{diss,max}$	0	0.042	0.042	0.042	0.043	0.043	0.000	J
$E_{abs,max}$	0	0.991	0.993	1.017	1.050	1.051	0.377	J
η_{max}	1	159.381	160.970	162.404	163.929	169.196	132.039	mm
$\theta_{top,max}$	1	1.507	1.632	1.822	1.947	2.081	2.956	deg
$\theta_{rel,end}$	1	13.249	14.251	14.436	15.468	15.651	6.351	deg
$E_{el,max}$	1	0.416	0.422	0.442	0.452	0.457	0.317	J
$E_{diss,max}$	1	0.425	0.430	0.444	0.474	0.485	0.090	J
$E_{abs,max}$	1	0.742	0.764	0.770	0.778	0.802	0.476	J
η_{max}	2	148.413	151.598	165.060	167.317	167.688	132.039	mm
$\theta_{top,max}$	2	2.292	2.311	2.453	2.480	2.556	4.239	deg
$\theta_{rel,end}$	2	11.783	11.786	11.790	14.004	14.004	5.418	deg
$E_{el,max}$	2	0.386	0.392	0.404	0.434	0.455	0.379	J
$E_{diss,max}$	2	0.415	0.452	0.472	0.523	0.526	0.153	J
$E_{abs,max}$	2	0.746	0.762	0.778	0.880	0.883	0.533	J
η_{max}	3	142.891	151.492	162.094	163.624	169.320	132.039	mm
$\theta_{top,max}$	3	2.706	2.744	2.936	3.020	3.376	5.101	deg
$\theta_{rel,end}$	3	8.109	8.478	9.213	10.314	11.421	1.652	deg
$E_{el,max}$	3	0.365	0.378	0.393	0.402	0.462	0.474	J
$E_{diss,max}$	3	0.389	0.400	0.416	0.469	0.512	0.070	J
$E_{abs,max}$	3	0.707	0.755	0.773	0.832	0.962	0.544	J
η_{max}	4	140.767	149.964	161.266	162.216	163.741	132.039	mm
$\theta_{top,max}$	4	3.115	3.160	3.406	3.485	3.572	5.344	deg
$\theta_{rel,end}$	4	4.599	5.137	6.443	7.553	7.749	0.561	deg
$E_{el,max}$	4	0.371	0.388	0.424	0.433	0.433	0.508	J
$E_{diss,max}$	4	0.298	0.323	0.348	0.393	0.438	0.032	J
$E_{abs,max}$	4	0.681	0.722	0.748	0.807	0.849	0.539	J
η_{max}	5	151.285	159.000	164.376	166.046	171.124	132.039	mm
$\theta_{top,max}$	5	3.404	3.610	3.724	3.760	3.763	5.430	deg
$\theta_{rel,end}$	5	3.314	4.055	4.420	5.888	5.890	0.197	deg
$E_{el,max}$	5	0.407	0.426	0.441	0.448	0.461	0.520	J
$E_{diss,max}$	5	0.243	0.265	0.289	0.369	0.375	0.014	J
$E_{abs,max}$	5	0.662	0.684	0.713	0.818	0.826	0.534	J
η_{max}	6	143.514	156.069	163.676	164.232	167.239	132.039	mm
$\theta_{top,max}$	6	3.852	3.853	3.939	4.208	4.351	5.472	deg
$\theta_{rel,end}$	6	0.355	1.680	2.672	2.766	3.497	0.056	deg
$E_{el,max}$	6	0.426	0.450	0.471	0.489	0.506	0.527	J
$E_{diss,max}$	6	0.033	0.151	0.207	0.226	0.290	0.005	J
$E_{abs,max}$	6	0.537	0.569	0.657	0.713	0.771	0.532	J
η_{max}	11	153.593	158.445	160.946	163.025	164.137	132.039	mm
$\theta_{top,max}$	11	3.948	4.054	4.277	4.481	4.563	5.495	deg
$\theta_{rel,end}$	11	-0.006	-0.004	-0.003	-0.001	-0.000	0.000	deg
$E_{el,max}$	11	0.460	0.478	0.503	0.552	0.553	0.531	J
$E_{diss,max}$	11	0.002	0.003	0.007	0.016	0.020	0.000	J
$E_{abs,max}$	11	0.473	0.478	0.515	0.553	0.554	0.531	J

C

Extra information on data processing

In this appendix, two elements of the data processing are explained in more detail. In section C.1, the difference between the two potentiometers at the top of the pendulum is analysed. Then, in section C.2, the data processing used to reduce the influence of the bad resolution of the potentiometers is shown.

C.1. Comparison potentiometers 1 and 2

Potentiometers 1 and 2 are both measuring the angle of the top part of the pendulum. In section 4.1, these two signals are averaged into one signal, and this signal is also used for calculation of the energy components in section 4.2. However, it should be analysed if this is a correct approach. For an example run, the signals of both potentiometers and the average between them are shown in figure C.1. Due to the resolution of each potentiometer, the signals of both sensors differ. This difference is not larger than one step in the resolution of the sensors. Therefore, it is accepted to use the average of both sensors in further calculations. It can even be beneficial for a first smoothing of the signal of the angle of the top part of the pendulum.

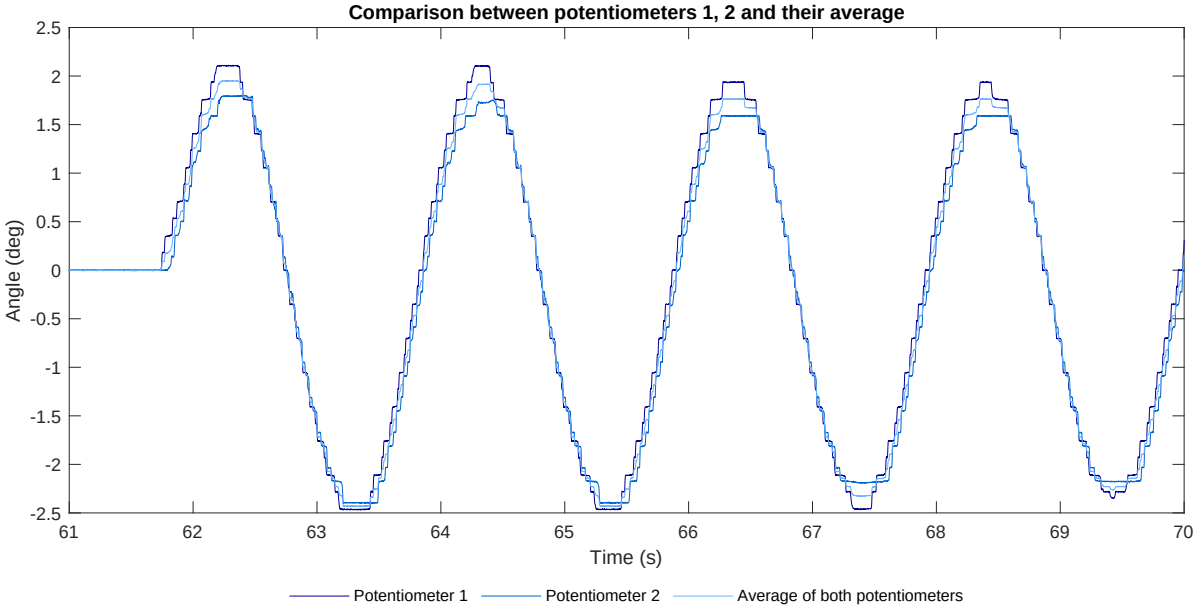

Figure C.1: Measurements of potentiometers 1 and 2 and their average. Due to the resolution difficulties of each potentiometer, the signals of both sensors differ from each other. This difference is not larger than one step in the resolution of the sensors. Therefore, it is accepted to use the average of both sensors in further calculations.

C.2. Fit function to overcome the bad resolution of potentiometers

As shown in section 4.1, some signals of the measured angles show horizontal parts. These horizontal parts become problematic when taking the derivative of the signal. Since these horizontal parts are not really part of the behaviour but only exist due to bad resolution of the potentiometers, a solution should be found to eliminate these horizontal parts. In order to show how this is performed, the same example run as in the previous section is used.

The first step in this process is selecting the parts of the graph that are horizontal or nearly horizontal. This selection is made by taking the data points that are in a range of 0.05 deg from each other. The intervals that satisfy this condition are selected as 'horizontal', and the other parts are selected as 'other'. Of each interval, the middle data point is selected. These are shown in figure C.2 as 'selected data points'. Through these selected data points, a cubic smoothing spline with a smoothness parameter P equal to $1\text{-}10^{-4}$ for the top angle and $1\text{-}10^{-5}$ for the bottom angle is fitted. These two fit functions are shown in figure C.2 with the top angle on the left and the bottom angle on the right. The values for P are based on tuning of the parameters.

The influence of the horizontal parts is examined by introducing horizontal parts in the signal obtained by the reduced-order model. The cubic smoothing spline is fitted through the middle points of these introduced horizontal parts. The results of the original signal and the fit function are approximately the same, which leads to the conclusion that the bad resolution of the potentiometers does not influence the conclusions of this research.

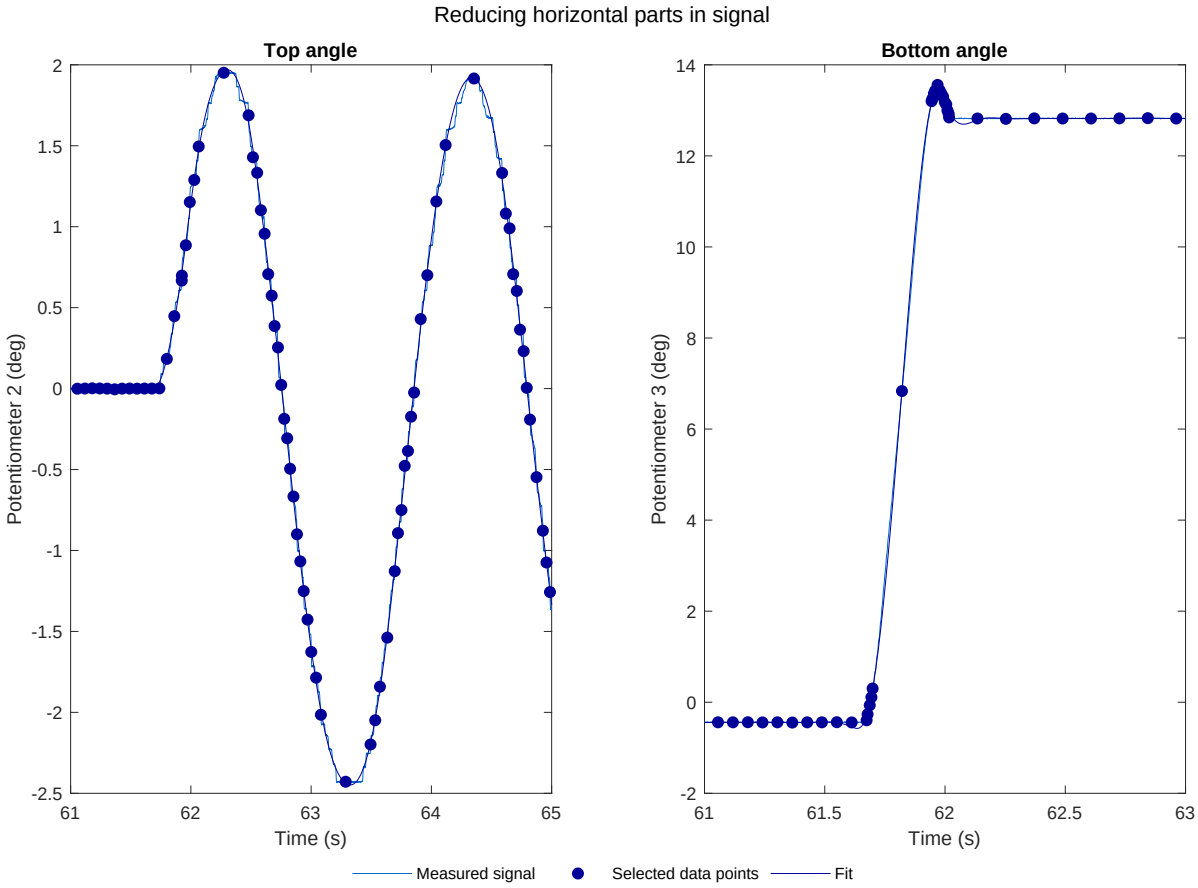

Figure C.2: The measured signal of the top (left) and bottom (right) angle of the pendulum. The selected data points are the middle points of the (approximately) horizontal intervals and the intervals in between. A cubic smoothing spline is fitted on these selected data points with smoothing parameters of $1\text{-}10^{-4}$ for the top angle and $1\text{-}10^{-5}$ for the bottom angle.